The primary crystallization nucleation kinetics in Al-based and Fe-based Metallic Glasses

By

Tianrui Duan

A dissertation submitted in partial fulfillment of

the requirements for the degree of

Doctor of Philosophy

(Materials Engineering)

at the

UNIVERSITY OF WISCONSIN-MADISON

2024

Date of the final oral examination: 04/24/2024

The dissertation is approved by the following members of the Final Oral Committee:
John Perepezko, Professor, MS&E

Dan Thoma, Professor, MS&E

Paul Voyles, Professor, MS&E

Izabela Szlufarska, Professor, MS&E

Mark Ediger, Professor, CHEM

Acknowledgments

I would like to express my deepest gratitude to the many individuals and institutions who have supported and guided me throughout my doctoral journey. Completing this thesis would not have been possible without their unwavering assistance and encouragement.

First and foremost, I am profoundly grateful to my advisor, Dr. Perepezko. His expertise and patience were invaluable throughout this research endeavor. His constructive feedback and insightful guidance have been instrumental in shaping the direction of this work. He has also enabled me to work on different research topics in addition to this thesis work, giving me a much broader experience pool from which I learnt many valuable lessons. I would also like to thank my committee members, Dr. Szlufarska, Dr. Voyles, Dr. Thoma and Dr. Ediger, for their valuable insights, critical evaluation, and time devoted to reviewing and providing feedback on my thesis. Their collective expertise greatly enriched the quality of my research.

I am indebted to the MS&E Department for providing the necessary resources, research facilities. All sorts of equipment like XRD, SEM and TEM helped my research. And the financial support of ONR (N00014-20-1-2704) is gratefully acknowledged, which allowed me to pursue this Ph.D. degree. The stimulating academic environment and access to the university's extensive library and research databases significantly contributed to the success of this project.

I am also grateful to my friends and group members who provided not only academic camaraderie but also moments of respite from the demands of research. Your friendship made this journey more enjoyable. I would like to thank for Seth Imhoff and

Ye Shen for their previous research which established the foundation of my project. I would also like to acknowledge the contributions of Wan Kim, Longfei Liu, and Chengrong Cao who provided valuable assistance during data collection and analysis, which significantly enhanced the quality of this thesis.

My heartfelt thanks go to my family for their unwavering support, understanding, and encouragement throughout my academic journey. I would also like to thank my wife, Yiqing, for all her encouragement and understanding during the challenging moments which helped me overcome frustrating time. Finally, I would like to thank our heavenly father that he gives me wisdom and a warm church community that help me finish this PhD journey.

Abstract

Amorphous alloys provide a valuable platform for dissecting the impact of local heterogeneities on nucleation and growth mechanisms, all without the interference of excess vacancies or dislocations that can complicate the kinetics in crystalline materials. Thus, amorphous alloys serve as an excellent model system for the systematic exploration of how spatial heterogeneities influence the crystallization process. In this thesis, we delved into nucleation behavior in two main systems: Al-Y-Fe and Fe-B alloys.

In amorphous Al alloys, particularly Al-Y-Fe alloys, the primary crystallization reaction results in ultrahigh densities of Al nanocrystals, ranging from 10^{21} to 10^{23} per cubic meter, typically measuring 10-20 nm in diameter. These nanocrystals are dispersed within an amorphous matrix, significantly enhancing the mechanical properties of the material. The presence of Al-like medium-range order (MRO) regions as a form of spatial heterogeneity in $Al_{88}Y_7Fe_5$ metallic glass (MG) acts as a catalyst, promoting primary crystallization. By measuring delay times using Flash Differential Scanning Calorimetry (DSC) and tracking Al nanocrystal density during isothermal annealing treatments via Transmission Electron Microscopy (TEM), we established an MRO-seeded nucleation kinetics model. This research demonstrates the profound impact of minor solute Cu on the crystallization behavior, affecting nanocrystal densities and transient behavior related to local spatial heterogeneities. The new nucleation model effectively accounts for the effects of heterogeneities induced by solute additions on primary crystallization.

In the case of Fe-based glasses such as Fe-B-Si and Fe-B-Nb, primary crystallization plays a pivotal role in optimizing magnetic properties. It has been observed that the precipitation of BCC-Fe nanocrystals smaller than the exchange length (30-40 nm) in Fe-based MGs can influence reduced coercivity and increased saturation magnetic flux density. In our study, we investigated the impact of varying heating rates, ranging from 0.17 K/s to 5000 K/s, on the crystallization behavior of BCC-Fe and explored the limitations on size reduction using Flash DSC and TEM. Our analysis revealed the compositional profile of B solute between adjacent nanocrystals, indicating that the limited size reduction and eutectic decomposition of BCC-Fe and Fe_3B at high temperatures result from diffusion field impingement. Importantly, our findings demonstrate that extremely fast heating exceeding 10^4 K/s is unnecessary for optimizing the binary Fe-B MGs composite with the best magnetic properties and, in fact, can lead to eutectic crystallization of BCC-Fe and Fe_3B, diminishing magnetic performance.

Table of Contents

Chapter **Page**

Acknoledgments i

Abstract.. iii

Table of Contents.. v

List of Tables vi

List of Figures... viii

Chapter I: Introduction... 1

Chapter II: Background and Literature Review 10

II .1 Crystallization Kinetics 10

II .1.1 JMAK equation and Kissinger Analysis 10

II .1.2 Nucleation Kinetics 14

II .1.3 Delay Time.. 21

II .2 Background of Al-based MGs 26

II .2.1 Crystallization Behavior 26

II .2.2 Medium Range Order 29

II .2.3 Minor Alloying Effects 34

II .3 Background of Fe-based MGs.. 44

II .3.1 Devitrification Behavior in Fe-B System... 44

II .3.2 Alloy Design to Improve Magnetic Properties 48

Chapter III: Experiment Procedures 53

III .1 Sample Preparation 53

III .1.1 Arc Melting... 53

III .1.2 Melt Spinning 53

III .2 Materials Characterization 55

III .2.1 X-ray Diffraction 55

III .2.2 Differential Scanning Calorimetry 55

III .2.3 Flash Differential Scanning Calorimetry 56

III .2.4 Microscopy Analysis 56

Chapter IV: Results and Discussion 60

IV.1 Nucleation Kinetics Studies for Primary Crystallization in Al-Y-Fe-Cu MGs ... 60

IV.1.1 Continuous Heating Treatment 60

IV.1.2 Isothermal Annealing Treatment 66

IV.1.3 Delay Time Measurement by Flash-DSC 72

IV.1.4 Particle Density Distribution 78

IV.1.5 MRO Seeded Nucleation Model 82

IV.1.6 Nucleation Kinetics Calculation 91

IV.1.7 Summary 99

IV.2 Nucleation Kinetics Analysis 101

IV.2.1 Thermal Analysis 101

IV.2.2 Microstructure Analysis 110

IV.2.3 Impingment in Fe-B MG 118

IV.2.4 Summary 122

Chapter V Concluding Remarks 123

Chapter VI Future Work 126

Appendix A 128

Appendix B 131

Appendix C 133

REFERENCES 135

List of Tables

Table **Page**

Table 1 A summary for the T_x for the primary crystallization in the Al-Y-Fe system with minor element doping 41

Table 2 The role of minor alloying elements in Fe-based amorphous/nanocrystalline alloys 52

Table 3 Summary of thermodynamic properties in different compositions by Cu-doping in $Al_{88}Y_7Fe_5$ system. The black up and down arrows give the increasing and decreasing trends compared to the values of $Al_{88}Y_7Fe_5$. 65

Table 4 Delay time τ for different temperature in compositions by minor-alloying in $Al_{88}Y_7Fe_5$ systems The delay time of $Al_{88}Y_7Fe_5$ is collected from Shen's work 77

Table 5 Summary of thermodynamic and structural parameters used in the nucleation model........ 88

Table 6 Summary of the delay times measured by Flash DSC, the delay time and the steady state nucleation rate measured by TEM for $Al_{88}Y_7Fe_5$........ 89

Table 7 Summary of the delay times measured by Flash DSC, the delay time and the steady state nucleation rate measured by TEM for $Al_{87}Y_7Fe_5Cu_1$........ 89

Table 8 Summary of the delay times measured by Flash DSC, the delay time and the steady state nucleation rate measured by TEM for $Al_{88}Y_6Fe_5Cu_1$........ 90

Table 9 Summary of the delay times measured by Flash DSC, the delay time and the steady state nucleation rate measured by TEM for $Al_{88}Y_7Fe_4Cu_1$ 90

Table B1 Summary of values and physical meaning of the parameters used in the Spaepen method calculation 132

Table C1 Thermodynamic parameters for Al-Y-Fe system.. 134

List of Figures

Figure **Page**

Fig. 1 (a) Schematic diagram of the change in volume and enthalpy with temperature as an undercooled liquid quenched bypass the glass transition temperature. (b) Schematic TTT-diagram and thermal pathway for the formation of crystalline phase (path 1,3) and glass (path 2) 7

Fig. 2 T_g versus log t_{anneal} plot for $Al_{88}Y_7Fe_5$ at T_{anneal}=240 °C, q=5000 K/s. A break point was identified at 525 s. TEM images were taken for samples annealed shorter (a,b,c) and longer (d) than the time corresponding to the break point 8

Fig. 3 The tensile strengths of aluminum alloys compared as a function of microstructural scale: (a) commercial purity aluminum; (b) the strongest conventional precipitation-hardened Al alloys; (c) amorphous, or part amorphous Al-TM-Ln alloys (TM: transition metals, Ln: lanthanides), consolidated and crystalized; (d) amorphous Al-TM-Ln alloys, partially devitrified to give nanometer scale crystallites. 9

Fig. 4 A schematic example of how the Avrami exponent during a reaction can change based upon the nucleation and growth mechanisms controlling the crystallization kinetics. Experimental observation of the transformation mode by (1) surface crystallization, (2) three-dimensional growth of crystals, and (3) segregation of solute to grain boundaries is necessary to understand the changes in the exponent, n. 13

Fig. 5 A Schematic plot of the free energy due to nuclei cluster size. S stands for surface. B stands for bulk. G* is the nucleation barrier 18

Fig. 6 The thermal energy, kT, defines a region of size space, Δ, within which clusters grow in a random walk manner 19

Fig. 7 Schematic of spherical cap nucleation of a liquid on a solid mold wall 20

Fig. 8 Schematic plot for crystal number density versus time relationship showing three stages of crystallization: transient nucleation, steady-state nucleation, growth, and coarsening 24

Fig. 9 Schematics showing kinetics of metallic glass formation: nucleation control vs. growth control. Quenching and reheating paths are shown on the TTT diagram and the thermogram (dQ/dt: heat evolution rate). 25

Fig. 10 Random close packing of quasi-equivalent, solute-centered atomic clusters to form Al-based MGs, as shown in ab initio MD simulations: (a) the ternary Al89La6Ni5 system; (b) the quaternary $Al_{85}Y_8Ni_5Co_2$ system. 32

Fig. 11 The simulated image of MROs embedded in the amorphous matrix in the as-spun Al-Y-Fe sample. The MRO is made of solely Al atoms. 33

Fig. 12 (a) Isothermal DSC scans for different transient metals induced Al-Y-Fe MGs. The doping elements are shown on each curve. (b) T_g for each composition 40

Fig. 13 An illustration of "Cluster Line Method" in the Al–Ni–Y ternary alloy phase diagram. Two solid lines corresponding to the ternary addition to the two respective binary clusters are shown for the whole system and the Al-rich corner (inset). The green star symbol at the intersection of the two lines is the favorable composition predicted, and the purple open star is the experimentally determined optimum glass formers. 42

Fig. 14 Frustration map of the polytetrahedral packing of identical hard spheres. If one tries to pack the 3-D space with the icosahedral clusters, packing frustration arises again due to the incompatibility of the fivefold rotational symmetry with long-range translational order. Green solid arrow points to the optimal choice at each stage 43

Fig. 15 Free energy vs. composition diagram for the Fe-rich Fe–B alloy system........... 46

Fig. 16 Various cores fabricated by Fe-based amorphous/nanocrystalline soft magnetic ribbons. 47

Fig. 17 The relationship between permeability (μe) at 1 kHz and saturation flux density (Bs) of soft magnetic materials. Reproduced with permission 51

Fig. 18 Schematic illustration of the melt spinning apparatus.. 54

Fig. 19 (a) Flash-DSC 2+ used in this research and (b) optical microscopy image of the chip sensor with the metallic glass sample. 58

Fig. 20 Calibration of the scattering mean free path (λ=191 nm) 59

Fig. 21 (a) Continuous heating DSC trace (20 K/min) of $Al_{88}Y_7Fe_5$ metallic glass. The onset temperature for the primary crystallization is at 267°C. (b) The XRD traces corresponding to different annealing products from heating to different labeled temperatures 63

Fig. 22 (a) Heat flow curves by normal DSC at 20K/min for 1at. % Cu-doping in $Al_{88}Y_7Fe_5$ systems. The down black arrows point to the onset temperature of primary crystallization. (a) Heat flow curves by normal DSC at 20K/min for 2 at. % and 4 at. % Cu-doping instead of Al in $Al_{88}Y_7Fe_5$ systems. 64

Fig. 23 (a)Schematic illustration for annealing treatments. (b)X-ray traces for $Al_{88}Y_7Fe_5$ annealed for various times at 245°C. 68

Fig. 24 Bright field TEM images for $Al_{88}Y_7Fe_5$ annealed for various times at 245°C. (a) as quenched, (b) 10 mins, (c) 20 mins and (d) 40 mins. 69

Fig. 25 Bright field TEM images of $Al_{87}Y_7Fe_5Cu_1$ which annealed under 245℃ for different time range: (a) 3000s, (b) 5000s, (c) 7000s and (d) 9000s. 70

Fig. 26 Bright field TEM images of $Al_{88}Y_7Fe_5$, $Al_{87}Y_7Fe_5Cu_1$, $Al_{88}Y_7Fe_4Cu_1$, and $Al_{88}Y_6Fe_5Cu_1$ after annealing 71

Fig. 27 A series of Flash DSC heat flow curves at 1000 K/s for $Al_{87}Y_7Fe_5Cu_1$ correspond to different annealing time t_a ranging from 10s to 7000s. 74

Fig. 28 Plot of glass transition temperature T_g and annealing time t_a (a) $Al_{87}Y_7Fe_5Cu_1$ annealing at 245℃, 247℃, 250℃ and 255℃; (b) $Al_{88}Y_7Fe_4Cu_1$ annealing at 170℃, 190℃, 200℃ and 203℃; (c) $Al_{88}Y_6Fe_5Cu_1$ annealing at 190℃, 195℃, 200℃ and 203℃ 75

Fig. 29 Bright field TEM images of $Al_{87}Y_7Fe_5Cu_1$ annealing under 247 °C: (a) before break point, (b) after break point 76

Fig. 30 The experimental (points) and calculated (solid curves) aluminum nanocrystal number density at various temperatures and times for $Al_{88}Y_7Fe_5$. θ is the intersection of the extrapolation of the nucleation curve and the time axis, which represents delay time 80

Fig. 31 The particle density vs. annealing time relationships for $Al_{87}Y_7Fe_5Cu_1$, $Al_{88}Y_7$Fe4Cu1, and $Al_{88}Y_6Fe_5Cu_1$. (a) $Al_{87}Y_7Fe_5Cu_1$ annealing at 245, 247, 250 and 255℃; (b) $Al_{88}Y_7Fe_4Cu_1$ annealing at 170, 190, 200 and 203℃; (c) $Al_{88}Y_6Fe_5Cu_1$ annealing at 190, 195, 200 and 203℃ 81

Fig. 32 (a) and (b) A schematic illustration of a nanocrystal nucleated on a disordered aluminum-like medium range order (MRO) region. The MRO/glass interface is replaced by the MRO/crystal interface. (c) The MRO rearranges and merges into the nanocrystal after nucleation.. 86

Fig. 33 J_{ss} vs T under homogeneous nucleation model. Red dash lines represent the temperature range in the experiment. 86

Fig. 34 Relationship between annealing temperature and delay time for four compositions (a) $Al_{88}Y_7Fe_5$, (b) $Al_{87}Y_7Fe_5Cu_1$, (c) $Al_{88}Y_6Fe_5Cu_1$ and (d) $Al_{88}Y_7Fe_4Cu_1$. The data points are the delay times measured directly from Flash DSC. The line is the delay time fitted by Arrhenius function. The activation energy Q are listed in the figure for each composition $Al_{88}Y_6Fe_5Cu_1$ and $Al_{88}Y_7Fe_4Cu_1$ have much lower Q compared to $Al_{88}Y_7Fe_5$ and $Al_{87}Y_7Fe_5Cu_1$ 87

Fig. 35 The calculated steady state nucleation rate (continuous curve) plotted together with the experimental Jss (data points) for $Al_{88}Y_7Fe_5$, $Al_{87}Y_7Fe_5Cu_1$, $Al_{88}Y_6Fe_5Cu_1$ and $Al_{88}Y_7Fe_4Cu_1$ 95

Fig. 36 (a) Al-Y-Fe ternary phase diagram. The red line represents the tangent line which shows the composition of liquidus at equilibrium which is Al-9.8Y-7Fe. The blue curve is the interface contour which shows the composition of liquidus at interface which is Al-12.2Y-5.1Fe. (b) Schematic showing the transformation affected region in the matrix .. 96

Fig. 37 (a) Transformed Volume Fraction for $Al_{88}Y_7Fe_5$ annealing at 245℃ (b) Simulation result for $Al_{88}Y_7Fe_5$ annealing at 245℃ where the solid curve is the calculation result and dashed curves represent the uncertainty of the calculation. 97

Fig. 38 The correlation between calculated ln($J_{ss}\tau$) vs ($\Delta G^*/kT$) for (a) $Al_{88}Y_7Fe_5$, (b) $Al_{87}Y_7Fe_5Cu_1$, (c) $Al_{88}Y_6Fe_5Cu_1$, and (d) $Al_{88}Y_7Fe_4Cu_1$. 98

Fig. 39 (a) DSC traces of $Fe_{85}B_{15}$ MG obtained at various heating rates. (b) XRD results of as-spun $Fe_{85}B_{15}$ MG and $Fe_{85}B_{15}$ MG composite annealed at 0.67 K/s up to 1st and 2nd peak temperature 105

Fig. 40 (a) Measured melting temperature of Al and Zn as a function of the heating rate. (b) Optical microscope image of Al and Zn on the UFH-1 sensor. 106

Fig. 41 (a) DSC and Flash DSC curves of $Fe_{85}B_{15}$ MG obtained at the heating rate of 5 K/s. (b) Optical microscope image of Al and Zn on the UFH-1 sensor. 107

Fig. 42 (a) Representative Flash-DSC results (b) Magnified curves showing glass transition signal (c) Kissinger plot of Crystallization onset temperature and peak temperature of BCC-Fe and Fe_3B crystalline phases.. 108

Fig. 43 Continuous Heating Transformation curve transposed from DSC and Flash DSC results 109

Fig. 44 TEM images and SAED patterns of annealed $Fe_{85}B_{15}$ alloys with the heating rate of 0.67 K/s, 50 K/s, 500 K/s, and 3000 K/s up to their T_p 113

Fig. 45 Size distribution of the precipitated nanocrystals in annealed $Fe_{85}B_{15}$ alloys heated at the heating rate of 0.67 K/s, 50 K/s, 500 K/s, and 3000 K/s up to their T_p. Red solid lines are the kernel density estimation. 114

Fig. 46 Average diameter and number density changes of BCC-Fe in annealed $Fe_{85}B_{15}$ as a function of heating rate (K/s). 115

Fig. 47 Bright-field TEM images of $Fe_{85}B_{15}$ MG annealed at 633 K for annealing time of 100s, 300s, 500s, and 1000s.. 116

Fig. 48 Number density (Black solid points) and average radius (Blue open points) of BCC-Fe changing as a function of annealing time. 117

Fig. 49 (a) Contour plot of V_f with the tangential lines representing t. Calculated diffusion field for B concentration (b) 108 nm, (c) 70nm, and (d) 40 nm separation with midpoint between nanocrystals. Detailed annealing conditions for calculations are described in the text. 120

Fig. 50 Calculated diffusion field of B concentration after the isothermal annealing for (a) 300s and (b) 600s. 121

Fig. A1 Quenched-in nuclei calculation under CNT in Al-Y-Fe MG 130

Chapter I: Introduction

The research on amorphous alloys began when Pol Duez, R. H. Willens, and W. Klement, at the California Institute of Technology in 1960, characterized rapidly cooled $Au_{75}Si_{25}$.[1] An overview of the different solidification pathways for both crystalline and amorphous alloys is shown in **Fig. 1**. When molten alloys are exposed to significant undercooling, the nucleation of stable crystalline phases is inhibited, which can extend the system's metastability by suppressing the formation of kinetically favored metastable phases.[2] This development of metastable phases has greatly expanded the range of microstructural options available for synthesizing new materials, particularly metallic glasses (MGs). MGs are metastable amorphous alloys that lack long-range order. [3] MGs exhibit higher strength compared to their crystalline counterparts and possess a polymer-like level of elastic limit, typically around 2%.[3,4]

The development of new glasses relies on a well-established set of alloying guidelines. These include negative heats of mixing between constituent elements, large atomic size ratios (greater than 10%), the use of multiple components, favorable valence electron ratios [5] , and compositions near deep eutectics.[6–8] While these guidelines are effective in predicting glass formation, identifying the necessary conditions to achieve a high density of dispersed nanocrystalline structures remains a challenging task. To synthesize amorphous alloys with improved glass-forming ability (GFA), it is crucial to delve into the crystallization process of MGs. MGs offer an advantage in this regard because they are free from excess vacancies or dislocations that can complicate kinetics in crystalline materials. This makes MGs an effective system for separately studying the influence of local heterogeneities on nucleation and growth mechanisms. Therefore, amorphous alloys serve as an ideal model system for the systematic exploration of how spatial heterogeneities influence the crystallization reaction. In this research, two main system types were selected for the study of the heterogeneous nucleation process and the understanding of glass stability: Al-RE (rare earth)-TM (transition metal) alloys and Fe-B alloys.

Al-based MGs (Al>80 at. %) with the rare-earth metals (RE) and transition metals (TM) additions were first discovered in the 1980s.[9,10] What sets these Al-based MGs apart is their relatively low density, which makes them attractive for a variety of engineering applications. Al-based MGs exhibit some unique characteristics. First, most Al-based MGs are considered marginal glass formers, unlike bulk MGS. Achieving their amorphous structure requires much higher critical cooling rates, typically in the range of 10^5 to 10^6 K/s. This has led to the predominant use of rapid solidification techniques like melt spinning for their production, although other methods such as cold-rolling [11] and ball-milling [12] have also been explored. Secondly, unlike some other MG systems such as Zr, Pd, and Ce-based MGs, which exhibit good glass-forming ability (GFA), most Al-based MGs do not display a clear glass transition (T_g) signal or a supercooled liquid region in differential scanning calorimetry (DSC) heating traces. This is because the onset of the primary crystallization peak (T_x) coincides with the glass transition.[13] In most cases, a typical continuous DSC trace for Al-based MGs shows a shallow primary crystallization peak for face-centered cubic (FCC) Al, followed by sharp crystallization peaks of intermetallic phases. The separation of over 50 °C between these primary and secondary crystallization peaks indicates a metastable equilibrium between Al and the glass. This is somewhat unexpected because, within the composition range favorable for glass formation, thermodynamics favor the formation of Al-rich intermetallic phases over FCC-Al.[14,15] The separation of nucleation reactions for different intermetallic phases is attributed to changes in the composition of the amorphous matrix. The formation of FCC-Al nanocrystals alters the matrix composition and leads to a different crystallization pathway.[16–18] According to Tsai et al., the dispersion of nanoscale FCC-Al in the amorphous matrix can be achieved in Al-Ni-Ce amorphous alloys only when the atomic size ratio falls in the range of 0.04-0.07 and the Al content ranges from 82-90 at.%.[19] Based on this unique crystallization behavior, Y. Shen [20] developed a method by using fast differential scanning calorimeter to determine the delay time of Al-based MGs at different annealing temperatures. From the Kissinger plot in this research, the glass transition requires a larger activation energy than the primary nucleation was found. With the increase of heating rates, both Tg and Tx move to higher temperatures. However, Tg requires more activation energy to shift, and Tg will trail behind Tx. Therefore, it is possible to discriminate the two signals in $Al_{88}Y_7Fe_5$ MG. As seen in **Fig. 2**, the T_g evolves differently before and after crystallization. Thus, the inflection point in the increase of T_g corresponds to the delay time of primary crystallization.

When primary crystallization occurs in Al-based MGs, it leads to the formation of a high number density of primary crystallized FCC-Al nanoparticles, typically ranging from 10^{21} to 10^{23} per cubic meter and measuring between 5 to 50 nanometers in diameter. This dispersion of nanoparticles within the amorphous matrix can be achieved by annealing the as-quenched amorphous Al alloys under specific experimental conditions.[13] Alternatively, directly solidifying the molten alloy at a cooling rate lower than the critical rate can also introduce FCC-Al particles into the matrix. [21,22] The strength of Al-based MGs in its as-quenched state can be further increased, surpassing that of many common steels, through partial devitrification during the primary crystallization process. As shown in **Fig. 3**, the tensile strength of Al-based MGs typically reaches around 1000 MPa. After primary crystallization, some alloys can achieve even higher strengths, up to 1500 MPa.[23] This strength improvement is attributed to the fine Al nanoparticles effectively acting as barriers to the movement of shear bands in the amorphous matrix. Additionally, the residual amorphous matrix undergoes hardening due to the enrichment of solutes associated with the primary crystallization reaction. The strength of partially crystallized alloys depends on the distribution of the nanocrystal particles, making it essential to understand and control the nucleation mechanism.

Fluctuation electron microscopy (FEM) experiments on Al-based glasses show that the structural heterogeneities exhibit diffraction from the {111} and {200} reflections of FCC-Al [24] but the higher angle / smaller d-spacing diffraction is strongly damped by disorder.[25] This disordered FCC structure has been variously described as “Al-like”, “defective Al”, or “disordered Al”. In between the strongly diffracting Al-like regions is a more disordered, less strongly diffracting structure which incorporates the rare earth and transition metal elements. In a recent work from Prof. Voyles’ group [26] , FEM data and electron scattering simulations were used to determine the mean size and volume fraction of the Al-like regions in $Al_{88}Y_7Fe_5$ and related alloy. It was suggested that the Al-rich regions can act to promote FCC-Al crystallization. Similar reports of quenched-in precursor structures were observed from Al-Y-Ni-Co amorphous alloys including the effects of minor solute additions of Cu, Pd and Nd in altering the crystallization behavior to yield an ultra-high Al nanocrystal density of about 10^{23} m^{-3}.[27,28] The discovery of MRO has laid the foundation for the development of a transient heterogeneous nucleation model. In this study, we have created a transient heterogeneous nucleation model that considers MRO density and delay time. Continuing research done by previous lab members Seth Imhoff and Ye Shen [20,29,30], this model has been designed to elucidate the primary nucleation mechanism for Al-Y-Fe MGs. Transmission Electron Microscopy (TEM) and Flash Differential Scanning Calorimetry (Flash DSC) were applied to investigate the delay time (τ) and the steady-state nucleation rate (J_{ss}), respectively, which support the validity of this model. Through this model, we gain the ability to manipulate the nucleation rate in Al-based MGs by altering the delay time. Furthermore, this model offers valuable insights for the development of Al-based MGs with enhanced GFA.

Much like Al-based MGs, Fe-B alloys exhibit similar primary crystallization behavior. Fe-based MG composites containing body-centered cubic (BCC) Fe nanocrystals are considered advanced soft magnetic materials, boasting a higher saturation magnetic flux density (B_s) compared to monolithic Fe-based MGs.[31,32] Furthermore, the coercivity (H_c) of these Fe-based MG composites, which is inversely proportional to permeability ($\mu_e=B_s/H_c$), can be reduced with decreasing BCC-Fe nanocrystal size when the crystal diameters fall below the natural exchange length (30-40 nm). [33]

Efforts to enhance magnetic performance have explored the impact of nonmagnetic additives as a means of controlling the crystallization process. Among the various elements studied, Cu has been found to act as a nucleation seed for BCC-Fe, while Nb can inhibit the growth of BCC-Fe.[31,34] The crystallization of primary BCC-Fe nanocrystals in Fe-based MGs containing these nonmagnetic additives has been carefully controlled to yield nanocrystals with diameters ranging from 10 to 20 nm.[35] However, it is worth noting that these nonmagnetic additives can have adverse effects on B_s, limiting the enhancement of B_s to around 1.9 T. [36]

In the pursuit of achieving a refined microstructure without relying on nonmagnetic additives, a new processing method has been proposed involving crystallization during rapid heating. By increasing the heating rate from 0.083 K/s up to 10^4 K/s, the diameter of primary BCC-Fe crystals that precipitate from the amorphous matrix in binary MGs like $Fe_{87}B_{13}$ [37] and $Fe_{86}B_{14}$ [38] has been reduced from 50-60 nm to 15-20 nm. These changes in microstructure effectively lower the H_c of binary Fe-B alloys and simultaneously elevate B_s beyond 1.9 T. However, it is important to note that above a heating rate of 100 K/s, there is no significant reduction in the diameters of BCC-Fe nanocrystals in binary Fe-B MGs. Furthermore, no processes or compositions have successfully decreased nanocrystal diameters below 10 nm, even with a heating rate of 10^4 K/s. In this study, microstructural changes in $Fe_{85}B_{15}$ MG were investigated using Flash DSC and TEM to determine the limitations of size reduction for BCC-Fe. The combined analysis of kinetics and local structure determination offers valuable insights into the influence of spatial heterogeneities on transformation behavior.

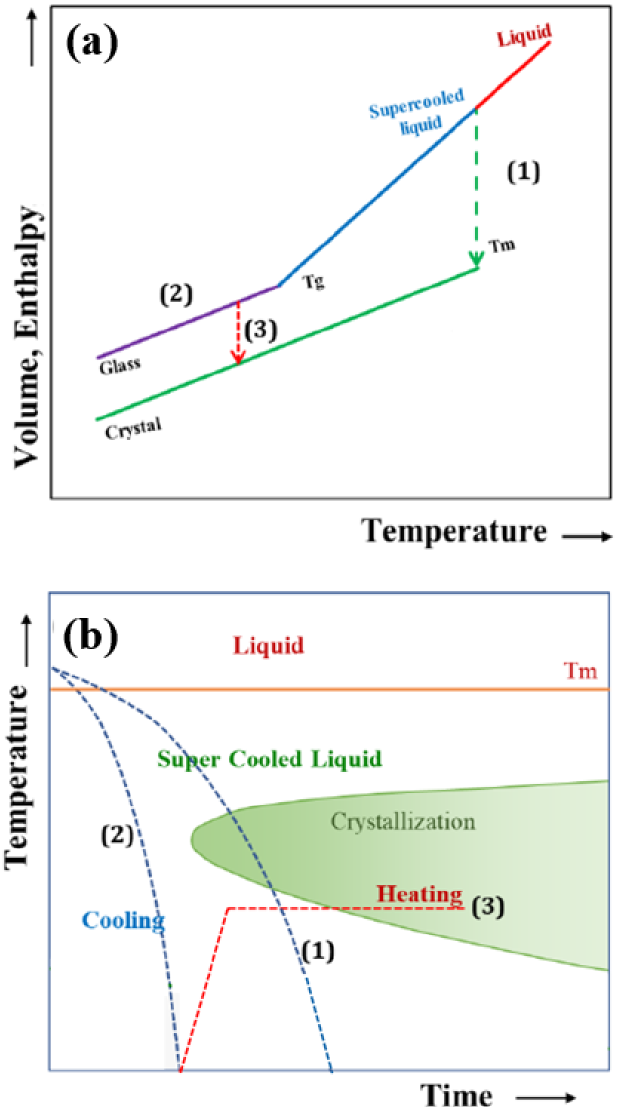

Fig. 1 (a) Schematic diagram of the change in volume and enthalpy with temperature as an undercooled liquid quenched bypass the glass transition temperature. (b) Schematic TTT-diagram and thermal pathway for the formation of crystalline phase (path 1,3) and glass (path 2).

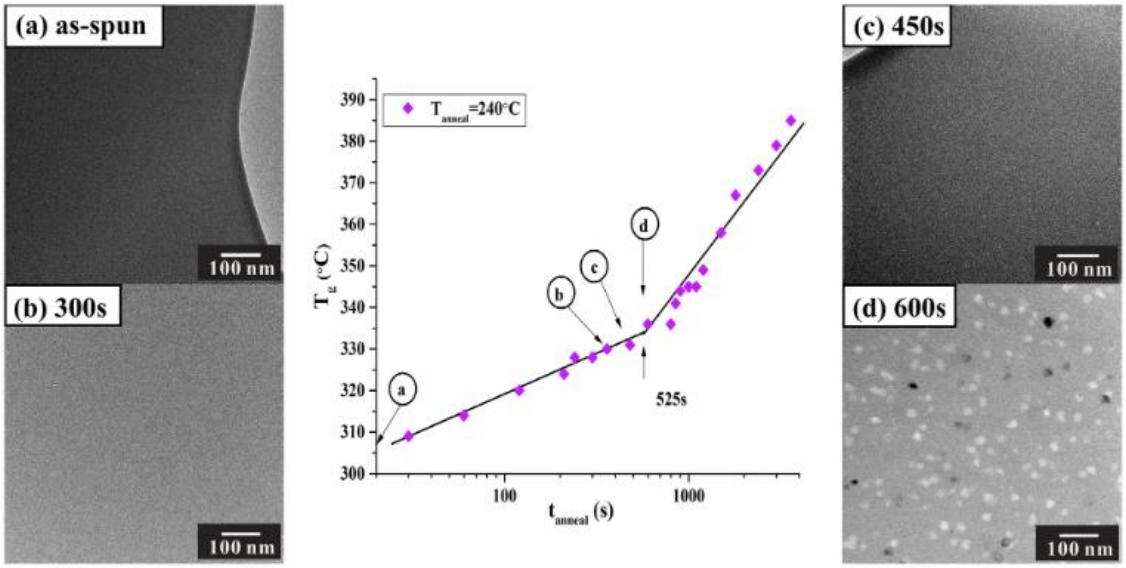

Fig. 2 T_g versus log t_{anneal} plot for $Al_{88}Y_7Fe_5$ at T_{anneal}=240 °C, q=5000 K/s. A break point was identified at 525 s. TEM images were taken for samples annealed shorter (a,b,c) and longer (d) than the time corresponding to the break point [20]

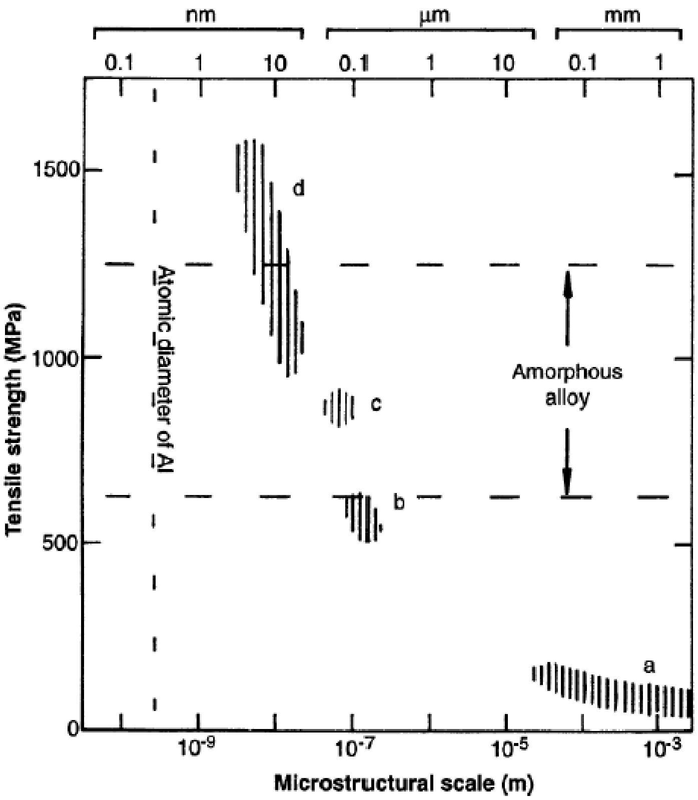

Fig. 3 The tensile strengths of aluminum alloys compared as a function of microstructural scale: (a) commercial purity aluminum; (b) the strongest conventional precipitation-hardened Al alloys; (c) amorphous, or part amorphous Al-TM-Ln alloys (TM: transition metals, Ln: lanthanides), consolidated and crystalized; (d) amorphous Al-TM-Ln alloys, partially devitrified to give nanometer scale crystallites.[23]

Chapter II: Background and Literature Review

II .1 Crystallization Kinetics

II .1.1 JMAK equation and Kissinger Analysis

In material science, the understanding of the kinetics of phase transformation processes under different external and internal conditions is important. And research into crystallization kinetics has largely centered around the analysis of DSC measurements.[39–41] The Johnson-Mehl-Avarmi-Kolmogorov (JMAK) equation [42–45] is a common model for understanding crystallization kinetics from DSC measurements.[46] In the JMAK analysis, it is assumed that transformed regions are randomly distributed within an untransformed matrix at a constant temperature. The volume fraction transformed is defined as:

$$x(t) = 1 - exp(-x_{ex}(t)) \qquad \text{Eq. 1}$$

where x_{ex}, the extended volume fraction, is the fraction which would be transformed if the dispersed volumes never impinged upon one another. After simplifying the extended volume fraction by assuming spherical particles, the volume of any given crystal can be described as $\frac{4\pi r^3}{3}$ or $\frac{4\pi v^3(t-\tau)^3}{3}$ where τ represents the delay time. This leads to a total unit volume defined as the integral of ensemble growth over time:

$$x_{ex}(t) = \frac{4\pi}{3}\int_0^t J(t-\tau)^3 v^3\, dt \qquad \text{Eq. 2}$$

where J is the nucleation rate and v represents the growth rate simultaneously. Grouping the temperature dependent terms into a new parameter, k, and substituting yields an expression for the transformed volume fraction, x, known as the JMA equation,

$$x(t) = 1 - exp(-kt^n) \qquad \text{Eq. 3}$$

where n is known as the Avrami exponent and contains information concerning the reaction mechanism. For instance, n was determined to be 2.5 for the primary crystallization of an $Al_{90}Tb_{10}$ amorphous alloy, which indicates a three-dimensional diffusional growth with constant nucleation rate.[47] Adaptations of this methodology are necessary during either isothermal or non-isothermal transformations because the fundamental assumptions for use of the JMA equation are not satisfied. These include a decreasing crystal growth rate with time, soft impingement of diffusion fields, and non-random nucleation protocols due to damped nucleation within the diffusion fields of growing crystals. With modification, this approach can produce a fit to primary crystallization DSC results, but the basic mechanistic understanding can be lost.

Interpretation of the local exponent is possible but requires that volume fraction estimates be coupled with observation of the microstructural evolution. An example of such an analysis is shown in **Fig. 4**, as adapted from Luck.[48] It has been shown that soft impingement as well as a continually changing diffusion coefficient during crystallization may be a more reasonable explanation for the growth mechanism during transformation.[49] Moreover, the application of the JMA analysis to continuous heating studies involves confounding effects of overlapping transitions that are often difficult to isolate for separate examination.

The Kissinger analysis is another widely used approach to describe crystallization kinetics based on continuous heating or cooling DSC measurement. The equation of Kissinger method can be expressed as

$$ln(\frac{T^2}{\Phi}) = (\frac{E}{RT}) + constant \qquad \text{Eq. 4}$$

where Φ is the heating rate, T is the reaction temperature, R is the gas constant and E is the activation energy for a specific reaction. However, the activation energies from the Kissinger analysis of the primary nucleation vary from 146 kJ/mol to 317 kJ/mol [50] and with the Avrami exponent ranging from 1.6 to 5.0.[39,50] Both E and n depend strongly on composition.[50] Though the JMA and Kissinger analyses are useful for a general characterization of thermal stability, a more detailed analysis with microstructural information is essential for a comprehensive understanding and prediction of crystallization behavior.

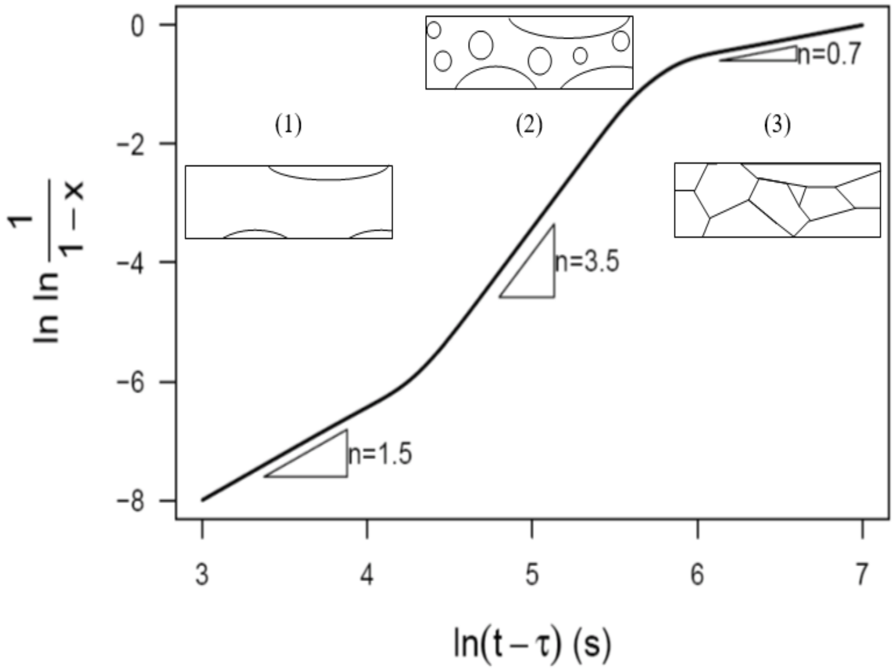

Fig.4 A schematic example of how the Avrami exponent during a reaction can change based upon the nucleation and growth mechanisms controlling the crystallization kinetics. Experimental observation of the transformation mode by (1) surface crystallization, (2) three-dimensional growth of crystals, and (3) segregation of solute to grain boundaries is necessary to understand the changes in the exponent, n.[48]

II .1.2 Nucleation Kinetics

A nucleation process, the first step for crystallization, is often required for a transformation from one phase into a more thermodynamically stable phase. In a liquid to solid transition, a liquid cooled below its equilibrium melting temperature, T_m, will not spontaneously transform until the driving force for nucleation overcomes the energy required to create a new liquid/solid interface. In a liquid undercooled below its melting temperature, the energy change from creating a bulk solid sphere containing n particles is given by:

$$\Delta G_B(n) = n v_a \Delta G_V \qquad \text{Eq. 5}$$

where ν_a is the atomic volume and ΔG_V is the volume energy difference between liquid and solid. The shape of a growing cluster is an important quality under the capillarity method of determining the energetic balance between the bulk and surface free energies. Like the section 1.1, after simplifying the nucleation crystals by assuming spherical particles, the number of atoms can always be transformed into a radius by an equivalent sphere method (volume can be calculated by using the number of atoms in a sphere), then the surface energy term can be expressed as:

$$\Delta G_S = 4\pi \left(\frac{3 n v_a}{4\pi}\right)^{2/3} \sigma \qquad \text{Eq. 6}$$

Where σ represents the distinct interfacial energy between the crystal and the liquid. Then, the overall free energy of the solid particle is obtained by adding the surface term to the bulk term:

$$\Delta G_n = \Delta G_S + \Delta G_B \qquad \text{Eq. 7}$$

Fig. 5 presents the free energy change of this process. The trends of ΔG_B and ΔG_S at temperatures below the melting point are such that there is a maximum in ΔG_n occurring at a cluster of finite size, n*, as shown in **Fig. 5**. The critical cluster size can also be represented by the radius of the cluster, where $r *= -2\sigma/\Delta G_V$. This maximum is the barrier to nucleation, however not all clusters that reach n* will survive as crystals. At a size of n*, a nucleus is in unstable equilibrium and the thermal energy, kT defines a region in size space in which the nucleus grows and shrinks by random fluctuation, demonstrated in **Fig. 6**. This region can be expressed as

$$\Delta = \frac{1}{Z\sqrt{\pi}} \qquad \text{Eq. 8}$$

where the Zeldovich factor, Z is defined by

$$Z \equiv \left[\frac{1}{2\pi kT}\frac{\partial^2 \Delta G_n}{\partial n^2}\bigg|_{n*}\right]^{1/2} \qquad \text{Eq. 9}$$

The Zeldovich factor is applied to correct among other things for the fact that some clusters that have reached the critical size still shrink to smaller sizes. It represents the curvature of the free energy ΔG_n curve near its maximum to compensate for the random walk process of cluster growth when they are in an unstable equilibrium. Furthermore, the proportion of nuclei which will grow beyond n*+Δ/2 and become truly stable is determined by the relative slopes on each side of n*. A simplistic estimate can be made that one half of all crystals which reach n* will be stable.

For the case of homogeneous nucleation, each monomer can act as a potential nucleation site. The With this statistical description of the rate of cluster growth discussed above, the homogenous steady state nucleation rate (J_{SS}) can be described as:

$$J_{SS} = \rho\beta Z\, exp\left(-\frac{\Delta G^*}{kT}\right) \qquad \text{Eq. 10}$$

This equation is known as classical nucleation theory (CNT) for homogenous nucleation, where ρ stands for monomer concentration. And β represents the attachment frequancy. The controlling atom attachment frequency can be thought of as either the movement of an atom across liquid/solid the interface or the replacement frequency, depending upon which is the slower rate limiting step.[51–53]

The homogeneous nucleation model could be extended to heterogeneous nucleation. Heterogeneous nucleation accounts for a population of initial particle inclusions inside the liquid. These particles lower the overall work necessary to create a supercritical cluster through their wetting behavior. A simple example is in droplet nucleation of a condensed phase from the vapor. Homogeneous nucleation requires impingement of individual monomers with the growing cluster until it reached n*, however if a solid surface is present, then a spherical cap shaped droplet is formed with a radius determined by the surface tension, as shown in **Fig.7**. This radius is now the effective radius of the droplet, and the agglomeration of monomers will become supercritical when it reaches r*. The balance of the interfacial tensions is reflected in the angle, θ, between the $\sigma_{S/L}$ and $\sigma_{L/V}$ vectors and lowers the nucleation barrier by a factor of f(θ). For a spherical geometry:

$$f(\theta) = \frac{1}{2} - \frac{3}{4}cos(\theta) + \frac{1}{4}cos^3(\theta) \qquad \text{Eq. 11}$$

Therefore, for a heterogeneous nucleation mechanism, the expression for the nucleation rate becomes:

$$J_{SS} = \rho\beta Z\, exp\left(-\frac{\Delta G^* f(\theta)}{kT}\right) \qquad \text{Eq. 12}$$

where ρ is now defined as the number density of nucleation sites rather than the monomer concentration. This model will be further developed in Al-based MGs by introducing the MRO as heterogeneous nucleation sites in this research.

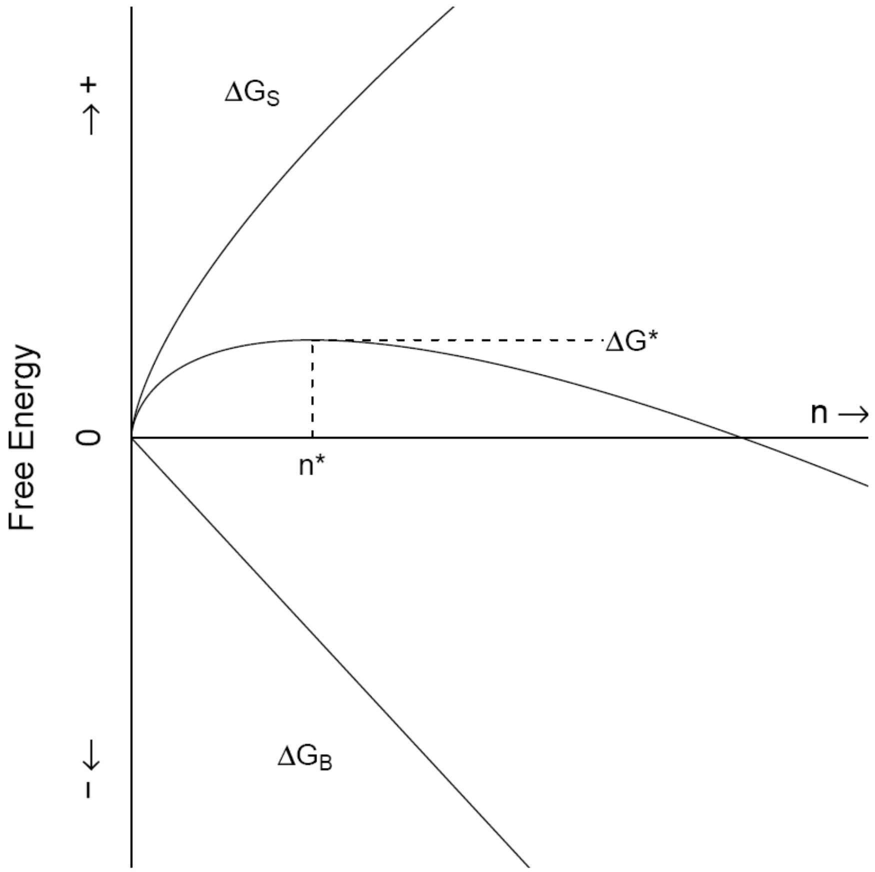

Fig. 5 A Schematic plot of the free energy due to nuclei cluster size. S stands for surface. B stands for bulk. G* is the nucleation barrier.

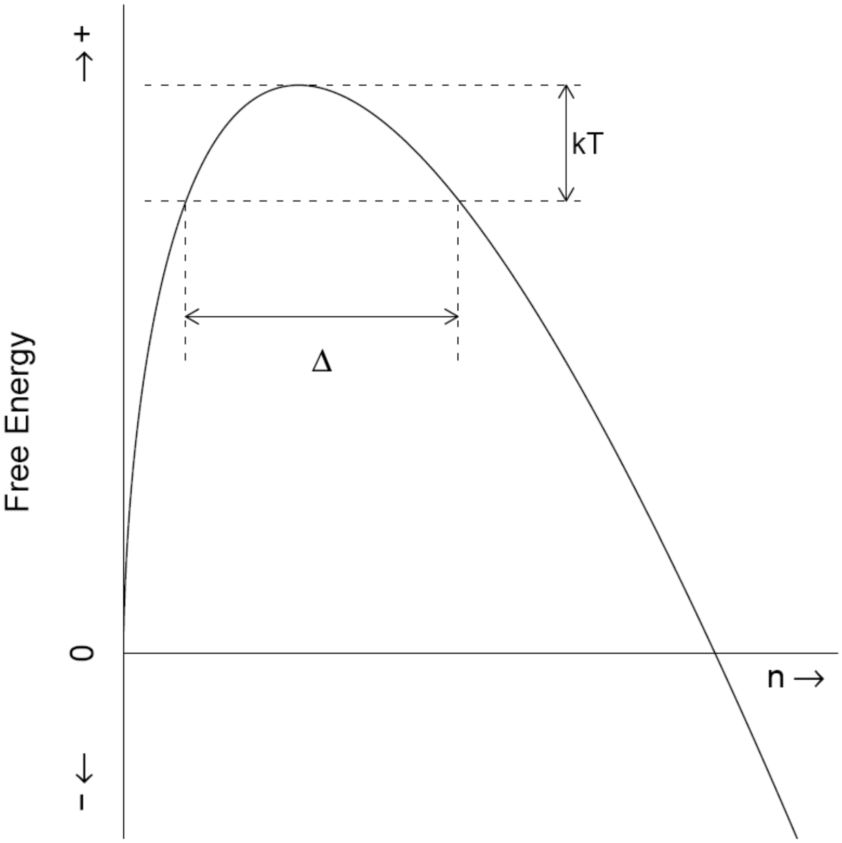

Fig. 6 The thermal energy, kT, defines a region of size space, Δ, within which clusters grow in a random walk manner.

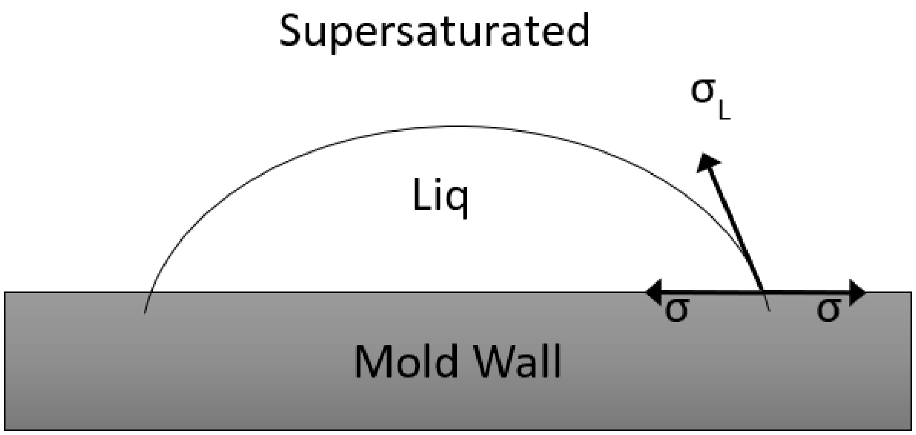

Fig. 7 Schematic of spherical cap nucleation of a liquid on a solid mold wall.

II .1.3 Delay Time

The delay time also known as incubation time or transient time represents the time lag for the new phase detection during nucleation or phase transition. The delay time has been researched widely in the context of crystallization behavior in oxide glasses and the precipitation behavior of inorganic electrolytes from aqueous solutions.[54,55] As the concept of "new phase detection" is subject to diverse interpretations, the delay time cannot be considered an inherent characteristic of a system. It can be explained through various processes, including: (1) the initial appearance of a crystal within the system which means that the first crystal reaches its critical size and forms a particle in the matrix. (2) the initiation of a transition in material properties, and so forth.

Fig. 8 illustrates a typical crystallization process for amorphous alloys during isothermal annealing treatment at a temperature below the T_x. Initially, the amorphous alloy undergoes a transient nucleation stage where the nucleation rate is near zero and meanly controlled by relaxation. After a certain time period, it enters a steady-state nucleation stage with a constant nucleation rate, during which existing nanocrystals grow simultaneously. Subsequently, the nucleation density reaches a plateau where the crystal number density stops increasing, but the crystals continue to grow, resulting in crystal coarsening. During heating, MGs maintain their amorphous state for a specific duration before transitioning into a crystalline phase.[56] This transitional period is what we refer to as the delay time. When nucleation reaches steady nucleation stage, the steady-state size distribution of nuclei spans all sizes up to the critical nucleus size, its achievement coincides with the achievement of the steady state nucleation rate. Therefore, the delay time in nucleation serves as a measure of the time required for the steady-state nucleation rate to be achieved for clusters of critical sizes.[57] To determine the delay time, one can extrapolate the linear segment of the particle number density versus annealing time curve until it intersects with the time axis, as outlined in some previous research.[56,58,59]

Expanding on the discussion of the nucleation process from the previous section, when we consider the growth of clusters towards nuclei with a critical size, the delay time can be defined as the duration during which atoms engage in a diffusion motion within a random walk zone around the critical cluster size.[57,60] In simpler terms, only clusters in the immediate vicinity of this critical size have the potential to evolve into nucleation particles. With this in mind, the delay time can be expressed as $\tau = \tau_c + \tau_\Delta$.[61] Here, τ_c represents the time associated with nucleation influenced by the thermodynamic free energy difference, and τ_Δ describes the time needed for a random walk to occur between a cluster size of 'n* - 0.5 Δ' and 'n* + 0.5 Δ.' The value of Δ signifies the cluster size distribution for which the rate-limiting step for growth is the random walk.

Now, the link between delay times and cluster growth has been established. The growth of clusters is intricately governed by the attachment frequency, which, in turn, is intertwined with the diffusion of atoms within the system. The connection between delay time and diffusion was initially introduced by Daynes [62], and it was further examined by Wu using both the monomer approximation and the more intricate multipath kinetics approach with detailed balancing.[63] So, the determination of τ offers a straightforward measurement to quantify the attachment frequency β, which can be expressed as:

$$\tau = \frac{1}{2Z^2\beta} \qquad \text{Eq. 13}$$

where Z is the Zeldovich factor. This method is favored over the conventional approach of approximating β by D/a^2, where D represents the diffusivity within the glass. It is worth noting that D can be challenging to define accurately for a multicomponent alloy, and a represents the jump distance. Furthermore, because D values are frequently not readily available, an additional approximation is often used to establish a connection between D and the viscosity (η) through the Stokes-Einstein relation ($D = \frac{k_B T}{6\pi\eta r}$, where r is the radius of the spherical particle). However, it is essential to mention that this relation has been demonstrated to be less valid near the T_g.[64]

Therefore, the delay time plays an essential role in comprehending transport and nucleation behaviors in MGs, which are fundamental for regulating nanoscale microstructures. As illustrated in **Fig. 9**, in the case of metallic glasses where nucleation predominates, the isothermal crystallization signal exhibits a distinct peak, enabling the direct measurement of the delay time.[65,66] However, for marginal MGs like Al-based and Fe based MGs where growth control prevails, the DSC signal shows a continuous decline, rendering the measurement of the delay time practically unfeasible.[67]

Consequently, determining the delay time for marginal MGs necessitates a laborious and time-consuming procedure, involving the quantification of particle number density in TEM images at different annealing times and specific annealing temperatures (as depicted in **Fig. 8**). The development of a more convenient method for measuring the delay time is not only meaningful but also essential.

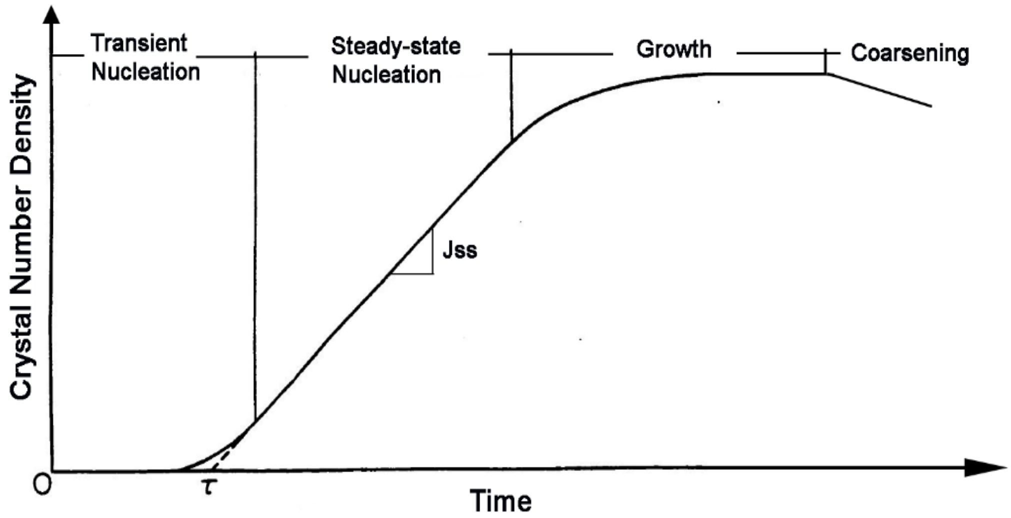

Fig. 8 Schematic plot for crystal number density versus time relationship showing three stages of crystallization: transient nucleation, steady-state nucleation, growth, and coarsening.

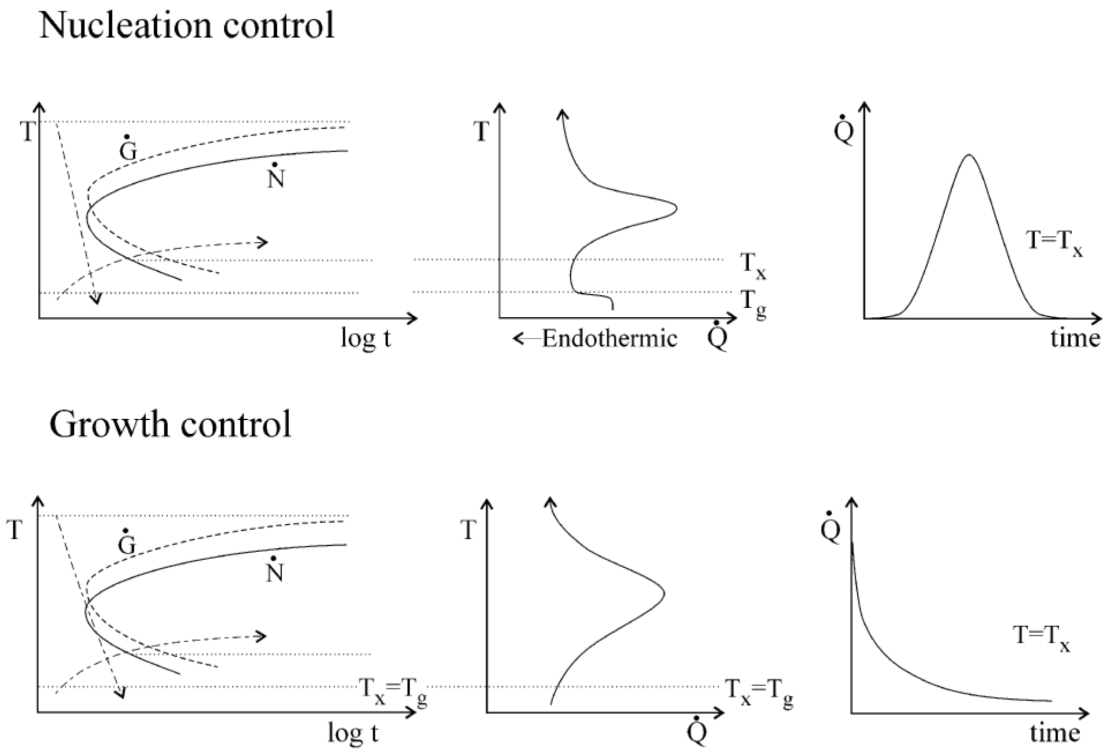

Fig. 9 Schematics showing kinetics of metallic glass formation: nucleation control vs. growth control. Quenching and reheating paths are shown on the TTT diagram and the thermogram (dQ/dt: heat evolution rate).[13]

II .2 Background of Al-based MGs

II .2.1 Crystallization Behavior

In the 1970s, reports emerged regarding partially vitrified microstructures in aluminum-metalloid and aluminum-transition metal binary systems.[68,69] Then, in 1981, researchers at Tohoku University achieved the successful preparation of fully vitrified Al-(Fe/Co)-B amorphous alloys through the melt spinning process.[70] However, these amorphous alloys within Al-TM-metalloid systems exhibited excessive brittleness, discouraging systematic studies of their fundamental properties. It was not until 1988, when Y. He and his colleagues published a report [71], that strong and ductile Al-TM-RE ternary glasses with an aluminum content of over 80% were introduced. Since then, various compositions have been explored in pursuit of ductile Al-TM-RE amorphous alloys.

Al-TM-RE glass formers can be categorized into two types of alloys: (1) Glassy alloys (clear T_g and eutectic crystallization) and (2) nanocrystalline alloys (unclear T_g and primary crystallization) which can be distinguished from each other and defined by the crystallization reactions.[72,73] Among them, the nanocrystalline type involved with the primary FCC-Al nanocrystals has been paid the most attention. The high number density of nanocrystals in Al-based amorphous alloys upon devitrification is unusual in comparison to other crystallization reactions. First, typical amorphous alloy compositions are hypereutectic and the thermodynamic driving free energy for crystallization favors intermetallic phase nucleation compared to a primary Al phase by a significant margin.[74] Thus, the selection of Al as the primary crystallization phase must be promoted by a nucleation catalyst to provide a significant kinetic advantage. Second, primary nucleation yields a high density of extremely small crystals, which further indicates a high nucleation rate and a relatively slow growth velocity. A comprehensive understanding of the primary crystallization mechanisms serves a dual purpose. It not only facilitates the development of novel Al-based MG composites incorporating nanocrystals but also plays a crucial role in unveiling the mysteries behind glass formation and advanced fabrication processes.[75,76] In pursuit of this knowledge, several models have been put forward, such as the "quenched-in nuclei model" [77] and the "phase separation model" [10].

In the “phase separation” model it is claimed that there is an underlying phase separation step prior to the crystallization, during which the Al-rich and the solute-rich amorphous phases form.[78–81] The experimental evidences supporting the “phase separation” model are given by the results from bright field TEM imaging [80], X-ray diffraction (XRD) [82,83], energy-dispersive X-ray spectroscopy/electron energy loss spectroscopy (EDS/EELS) [84], atom probe tomography (APT) [81,85,86], small-angle and wide angle X-ray scattering (SAXS/WAXS) [79,87,88] and high energy XRD (HEXRD) [85] investigations. For example, the XRD pattern of the amorphous $Al_{87}Ni_8La_5$ alloy annealed at 150 ˚C (78 degrees lower than T_x) for 25 h shows two diffuse halos from the Al enriched and Al depleted amorphous regions.[82] However, the large negative enthalpy of mixing in amorphous Al alloys does not favor phase separation.

On the other hand, the “quenched-in nuclei” model proposes that there are crystal embryos formed in the undercooled liquid during the rapid quenching. Supporting evidence are given by computer simulation [89], nuclear magnetic resonance (NMR) measurement [50] and JMA analysis [47]. Computer simulations show that there are FCC clusters of between 40 and 100 Al atoms in an Al-Y binary alloy. [89] The NMR results revealed the existence of quenched-in Al clusters which are indistinguishable from the atomic configuration of atoms in fcc α-Al in the as-spun $Al_{85}Ni_{11}Y_4$ amorphous alloy.[50] However, due to the rapid viscosity increase with the decreasing temperature, there is not enough time for them to grow into crystals.[11,90–92]

A common feature of both models is that the as-spun Al amorphous alloys are spatially heterogeneous, but the origin of the heterogeneities is different between the two models.[93] Some related work shows that heterogeneities were found in an as-quenched sample.[22,39,93,94] Direct evidence for the presence of Al-rich regions in an as-quenched $Al_{85}Ni_{11}Y_4$ amorphous alloy was provided in the analysis of the ^{27}Al signal in NMR (nuclear magnetic resonance) scans.[50] In addition, there have been a few computational studies that are related to the development of spatial heterogeneities in undercooled liquids and glasses and their effect on nucleation.[95–107]

II .2.2 Medium Range Order

Irrespective of the nucleation mechanisms discussed earlier, the origin of primary crystallization in amorphous aluminum alloys must, in some manner, be linked to the structure associated with spatial heterogeneity present in as-quenched Al amorphous materials. Researchers have employed X-ray absorption fine structure (XAFS) [108] and extended X-ray absorption fine structure (EXAFS) [10] techniques to probe the atomic structure within Al-based glasses. As depicted in **Fig. 10**, the bond distance and coordination information derived from XAFS [108] suggest strong interactions between Co or Fe atoms and Al atoms, indicating covalent bond-like properties. Furthermore, EXAFS analysis on Al-La-Ni alloys [10] indicates that Ni is surrounded by Al or La, not Ni atoms, which is explained by an electronic orbital match between Ni and La or Ni and Al atoms. Both studies support the notion of a significant interaction between solvent and solute atoms. This led Miracle and Senkov [109–112] to introduce the concept of solute-centered clusters, and their efficient cluster packing (ECP) model extends this concept to larger length scales. According to their model, various types of polyhedral clusters exist within the atomic structure to achieve ECP. While these findings shed light on the atomic structure of as-quenched Al-based glasses, none of them exhibit a direct connection with primary crystallization in these materials.

In the present study, FEM is applied to analyze the structure driving primary crystallization in the as-quenched state of MGs. FEM is sensitive to many-body atom correlations, enabling the detection of nanometer-scale structures called medium-range order (MRO) in amorphous materials.[113] MRO is an intermediate structural order that lies between short-range order and long-range order in amorphous materials. FEM scrutinizes spatial fluctuations in diffraction with nanometer-scale resolution, making it adept at detecting MRO.

Voyles et al. [114] and Nittala et al. [115] had previously reported changes in MRO in hydrogenated amorphous Si films, where MRO stability during heat treatment was found to depend on the initial size of MRO in the as-sputtered samples. Stratton et al. [24] pioneered the application of this technique to Al-based glasses and identified FCC Al-like MRO in $Al_{92}Sm_8$. The term "Al-like" implies that this structure diffracts under the same conditions as FCC-Al, suggesting that its internal atomic structure is akin to that of FCC-Al. However, this structure might also exhibit strain, distortion, or defects.[25] Atom probe tomography conducted on $Al_{90}Sm_{10}$ [21] supports the existence of nano-sized pure Al regions in as-quenched samples, even though there is no crystallographic information in the APT data. Notably, a similar MRO was not found in an $Al_{92}Sm_8$ sample that was amorphized by cold rolling. DSC revealed primary crystallization in melt-quenched samples but not in cold-rolled samples.[11] Furthermore, cold-rolled samples exhibited an apparent glass transition and an exothermic signal corresponding to eutectic phase formation. This indicates that the presence of Al-like MRO is associated with primary crystallization.

As shown in **Fig. 11**, $Al_{88}Y_7Fe_5$ alloy, when rapidly quenched from the liquid phase, also exhibits the formation of nanoscale aluminum-like MRO. Sheng et al. [116] have reported that the development of MRO in Al-based MG is not only dependent on larger distances but also requires the cooperation of clusters rather than individual atoms. Hence, the degree and extent of MRO may vary with cooling rates. However, only MD simulation indicates this phenomenon, which haven’t been proved by experiments. In the case of Al-Y-Fe amorphous alloys, the size and density of MRO structures are tested approximately 1.8 nm in diameter, with a number density of around 10^{25} per m^3.[26] These findings align with Atom Probe Tomography measurements for pure Al regions.[81,85]

The information regarding MRO can be applied to the study of crystallization and stability within a system, as it forms an integral part of both nucleation and precipitate phase growth. Preexisting structural arrangements, especially if they dominate the structure, can influence nucleation in various ways: (1) Altering the transport behavior to/from the nucleus by changing diffusivity or promoting cluster growth through multi-atom additions. (2) Modifying the activation barrier for nucleation. (3) Changing the relevant site density. (4) Creating a non-random nucleation protocol by excluding specific volumes.

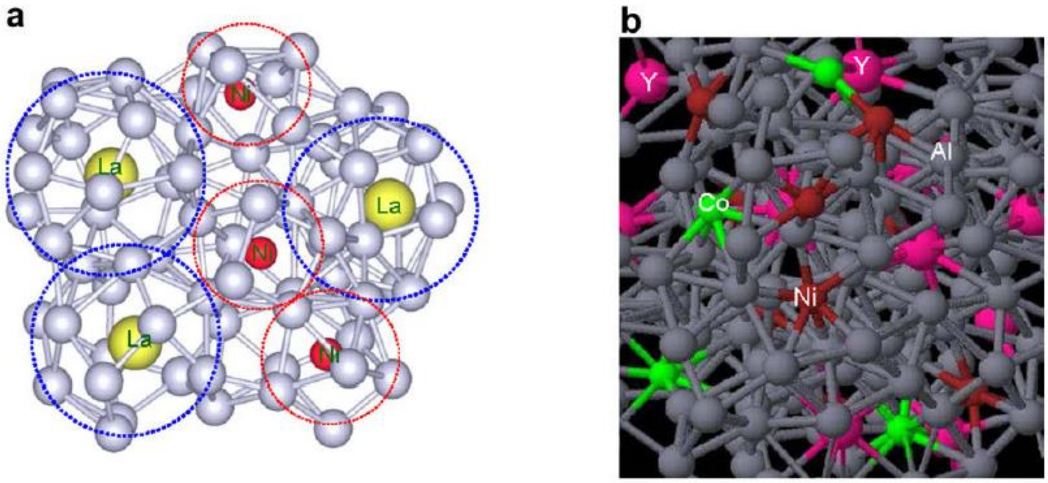

Fig. 10 Random close packing of quasi-equivalent, solute-centered atomic clusters to form Al-based MGs, as shown in ab initio MD simulations: (a) the ternary $Al_{89}La_6Ni_5$ system; (b) the quaternary $Al_{85}Y_8Ni_5Co_2$ system. [117]

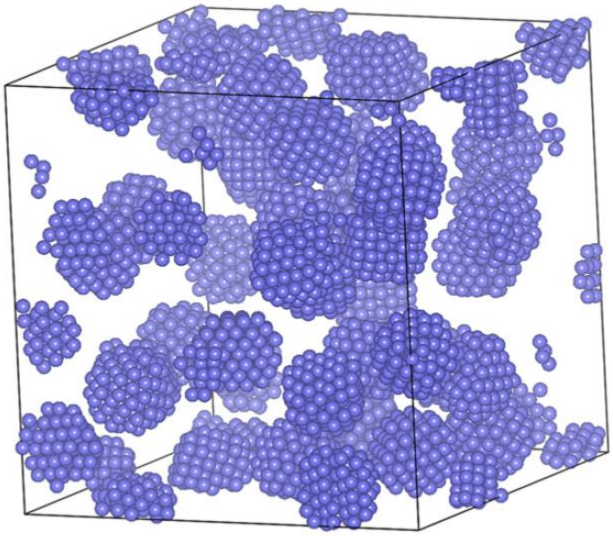

Fig. 11 The simulated image of MROs embedded in the amorphous matrix in the as-spun Al-Y-Fe sample. The MRO is made of solely Al atoms. [25]

II .2.3 Minor Alloying Effects

Since the 1980s, researchers have delved into the effects of minor alloying in MGs. Zhang et al. [118] observed that the GFA of Zr–Al–Ni–Cu alloys with oxygen impurities could be enhanced by adding 2–4% of Y. Similarly, Liu et al. [119] found that a mere 2% increase in Al content can substantially reduce crystalline phase formation in a well-established Zr-based bulk MG containing high oxygen levels. Similar minor alloying effects were also studied in Fe-based BMG [120] and Cu-based BMG [121]. It was found out that a 2% minor addition could significantly enhance the thermal stability of BMGs.

In the Al-based metallic glasses, the substitution of minor elements usually induces a significant change in the kinetic behavior.[30,67,122–125] For instance, in the Al-Y-Fe MG system, the addition of minor amounts of Pb has been observed to greatly accelerate primary crystallization. Insoluble Pd clusters act as a catalyst and result in a higher number of smaller FCC-Al nanocrystals.[124] Besides, substitutions of Al, Y, and Fe with Cu in the same system play distinct roles: the substitution of Y or Fe by Cu accelerates the primary crystallization by decreasing the crystallization temperature and increasing nanocrystal number density; the substitution of Al by Cu suppresses the primary crystallization by increasing the crystallization temperature and decreasing the nanocrystal number density.[30] In addition, a series of tests involving the addition of elements like Ti, V, Ni, Co, Cr, and Mn to the Al-Y-Fe system has been conducted. [122,125] The results from DSC and T_g measurements for different alloy additions are illustrated in **Fig.12**. It is evident that the primary crystallization behavior is highly sensitive to minor alloy additions. For instance, the inclusion of Ti [67] and V [125] in

Al-Y-Fe alloys enhances the difference between the onset of T_x and T_g, leading to improved GFA. These transition metal elements exhibit a negative enthalpy of mixing with Al, suggesting the potential formation of strongly bound icosahedral clusters around solute elements with negative heat of mixing with Al. From **Table 1**, in the Al-Y-Fe system, minor element doping can introduce a significant 100°C change in T_x.

Similar minor alloying effects have been observed in other Al-based MG systems. In the Al-Y-Ni system, previous studies on crystallization kinetics and phase competition have indicated that the Al-rich region of the ternary alloy with around a 10–15 at. % of solute is a good glass former. [126–129] Addition of small amounts of various alloying elements such as La, Ce, B, Si, Ge, Cu, Mn, Fe, or Co has been extensively studied in the Al-Y-Ni system. [130–143] For instance, partial replacement of Y with La or Ce significantly improves the thermal stability of the amorphous phase in Al–Ni–Y. [132,143] Addition of B, Mn, Fe or Co to Al-Y-Ni system also increases the primary crystallization temperature and improve the thermal stability of the amorphous phase.[130,133] These studies showed that the Kissinger analysis activation energy of primary crystallization in doping composition increased, which indicate a better thermal stability after minor additions. However, the detailed reasons for the increase in T_x after minor additions remain unclear. There are also some elements that decrease the GFA of Al-Y-Ni MGs. Addition of Si and Ge to Al-Y-Ni induced chemical heterogeneity in the amorphous alloy due to the bigger difference of binding force between the addition elements and Y. Consequently, the onset temperature of primary crystallization decreases more quickly with the increasing Si and Ge content. [131,136]

Like the Al-Y-Fe-Cu system[30,144], Cu addition has been proven to change the primary crystallization behavior and the size of α-Al nanocrystals in the Al-Y-Ni system. Substituting 1 at. % of Cu for Al increases the thermal stability of the amorphous phase, whereas substituting Cu for Ni decreases its thermal stability. It is also found that substitution of Cu for Ni could decrease the average size of the nanocrystals and hence increase the number density of nanocrystals.[135,138,140,142] Similar effects are observed in systems like Al-Ce-Ni and Al-Sm-Ni systems, where Al substitution by Cu enhances amorphous structure stability while Ni substitution by Cu decreases it. [135] However, the reason behind the crystallization behavior change remains unclear.

In order to predict which alloy composition is a promising glass former, various parameters have been proposed as indicators of GFA, such as the reduced glass transition temperature $T_{rg}(=T_g/T_l)$, the width of the supercooled liquid region $\Delta T_x(=T_x-T_g)$, and $\gamma=[T_x/(T_g+T_l)]$ where T_l is the liquidus temperature. By analyzing critical cooling rates across a range of Al-based amorphous alloys, it has been observed that systems with a larger negative value of ΔG_{mix} exhibit higher GFA.[145] As another example, the improvement in GFA observed in $Al_{86}Ni_6Y_6Ce_2$ compared to $Al_{88}Ni_6Y_6$ amorphous alloy is attributed to an increase in the number of components. Based on the confusion principle, multi-component alloys having three or more elements increase complexity and reduce the energetic advantage of forming an ordered structure of longer-range periodicity, which could achieve better GFA.[146] However, these criteria, while insightful, still have limitations in terms of predictive capability.

A method called the "Cluster Line Method" has been developed to explain the microstructure of Al-based MGs. It helps identify the optimal compositions for glass formation in Al-RE-TM ternary metallic glasses by allowing each Al atom to be shared by both a TM-centered cluster and a RE-centered cluster.[147–149] With the “Cluster Line Method”, an optimal glass former in Al-RE-TM alloy system was pinpointed by the intersection of the two cluster lines and the composition of the lines was determined by the number of nearest neighbors given by the atomic radii of the corresponding elements. Yang et al. [150] applied this method in the Al-Y-Ni ternary phase diagram. As shown in **Fig. 13**, they introduced Ni into Al–Y by increasing the Ni content along the composition line linking the Ni apex and the $Al_{16.9}Y$ composition, such that the desired $Al_{16.9}Y$ ratio was maintained. Similarly, a composition line was constructed by linking the Y apex and the $Al_{9.4}Ni$ composition. $Al_{16.9}Y$ and $Al_{9.4}Ni$ are favorable SRO clusters in the Al-Y-Ni system determined by a simulation study.[116] The intercept of two lines gives a predicted composition $Al_{85.8}Ni_{9.1}Y_{5.1}$, which is then a likely candidate for easy glass formation in the Al–Ni–Y system. Using this method, $Al_{86}Ni_8Y_6$, which closely matches the predicted composition, was discovered. The amorphous structure of $Al_{86}Ni_8Y_6$ with a critical thickness of approximately 600 μm can be obtained under wedge casting condition. After adding La and Co as minor addition in the system, 1 mm diameter amorphous rods were prepared with $Al_{86}Ni_6Y_{4.5}Co_2La_{1.5}$, $Al_{86}Ni_7Y_5Co_1La_1$ and $Al_{86}Ni_7Y_{4.5}Co_1La_{1.5}$.[147,150]

At the local structure level, molecular dynamics (MD) simulations have explored icosahedral clusters (ICO) to understand GFA in MGs.[107,151–153] As **Fig.14** shows, ICO structures do not exhibit global periodic packing, leading to geometric frustration that promotes glass formation. For instance, in the Al-Sm system, the size and strong d-electron bonding characteristics of Sm atoms hinder FCC short-range order (FSRO) and enhance icosahedral short-range order (ISRO), favoring glass formation.[151] The correlation between ICO and GFA was also found in ternary systems. In Al-Sm-X (X being Ag, Au, Cu) systems, MD simulations have revealed a correlation between ICO and GFA.[153] Minor alloying elements like X also affect the composition of ICO-like clusters, influencing the nucleation process in Al-Sm-X systems. It was found that the $Al_{90}Sm_8Ag_2$ system exhibits the best GFA due to its largest number of Al within the ICO-like cluster, which is followed by the $Al_{90}Sm_8Cu_2$ system, and then by the $Al_{90}Sm_8Au_2$ system. In the Al-Fe system, the addition of Nb enhances GFA because Nb dissolves in icosahedral Al-Fe clusters, stabilizing icosahedral local symmetry. [154] Likewise, the improved GFA from doping Ni into the Al-Y-La system is explained by the formation of Ni-centered icosahedron-like polyhedra that enhance spatial connectivity between clusters.[155] Furthermore, adding 1% Ag to the Al-Ni-Y system enhances GFA by acting as "glue" atoms to strengthen the glassy structure.[156] However, the GFA decreased by adding more Ag content in the system. After increasing the content of Ag to 2%, Ag may affect the formation Ni-centered polyhedral clusters. New Y-centered polyhedral clusters with coordination number of 10-13 appear in the alloy, which lead to a decrease in GFA. In addition, Yi et al. [157] have reported that addition of 0.2% Si improved GFA of Al-Ni-La alloy by enhancing the random atomic packing density in its amorphous structure. However, increasing the Si content further resulted in greater structural heterogeneity, causing a decrease in the GFA of the base alloy. Although these studies indicated local arrangements could affect GFA in amorphous Al alloys, a comprehensive guideline for local structure is still under development.

Kinetic factors also significantly affect GFA. Wang et al. [158] suggest that Al-RE glass formers with hypereutectic compositions can exhibit large non-equilibrium undercooling because phase growth via the motion of steps is generally sluggish for faceted crystals or complex compounds. Changes in T_x in the Al-Y-Fe system due to Cu doping are believed to be related to transport behavior alterations, affecting the activation energy during the nucleation transient stage.[29,144] There is also an increase in T_g with microalloying of TM to Al-Y-Fe alloys due to reduced atomic mobility.[122]

As evidence accumulates regarding the impact of minor alloying on GFA and crystallization behavior in amorphous Al alloys, it is clear that these effects are significant. While some trends have emerged for specific additions and substitutions, a complete mechanistic understanding is still a work in progress.

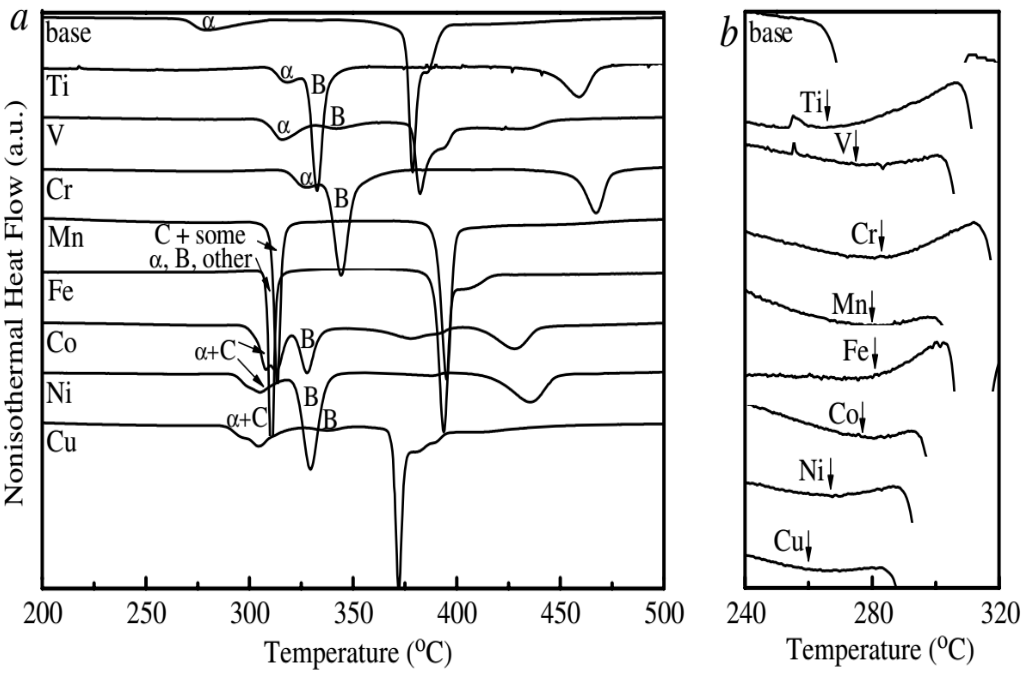

Fig. 12 (a) Isothermal DSC scans for different transient metals induced Al-Y-Fe MGs. The doping elements are shown on each curve. (b) T_g for each composition [122]

Table 1 A summary for the T_x for the primary crystallization in the Al-Y-Fe system with minor element doping [123]

Composition	**T_x (°C)**	**Composition**	**T_x (°C)**
$Al_{88}Y_7Fe_5$	267	$Al_{88}Y_7Fe_4Ni$	240
$Al_{87}Y_7Fe_5Pb$	247	$Al_{88}Y_7Fe_2Ni_3$	210
$Al_{87.5}Y_7Fe_5In_{0.5}$	232	$Al_{88}Y_6Fe_5Cu$	221
$Al_{87}Y_7Fe_5In$	229	$Al_{88}Y_7Fe_4Cu$	222
$Al_{86.5}Y_7Fe_5In_{1.5}$	223	$Al_{88}Y_7Fe_{4.5}Cu_{0.5}$	247
$Al_{86}Y_7Fe_5In_2$	220	$Al_{87}Y_7Fe_5Cu$	278
$Al_{87}Y_7Fe_5Ni$	283	$Al_{87.5}Fe_5Y_7Ti_{0.5}$	310

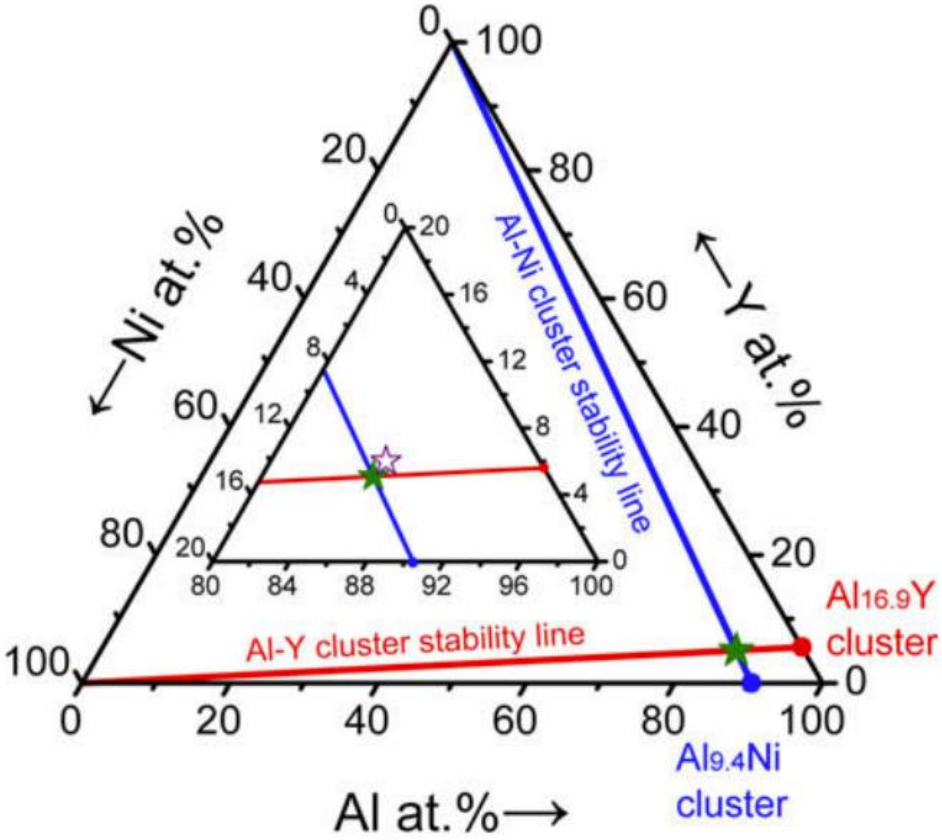

Fig. 13 An illustration of “Cluster Line Method” in the Al–Ni–Y ternary alloy phase diagram. Two solid lines corresponding to the ternary addition to the two respective binary clusters are shown for the whole system and the Al-rich corner (inset). The green star symbol at the intersection of the two lines is the favorable composition predicted, and the purple open star is the experimentally determined optimum glass formers. [150]

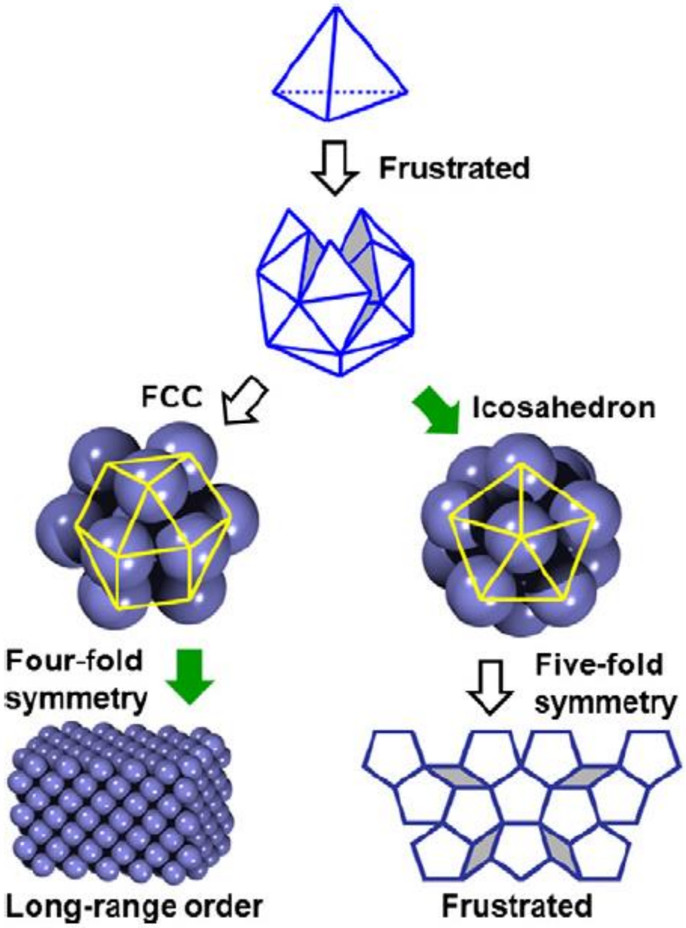

Fig. 14 Frustration map of the polytetrahedral packing of identical hard spheres. If one tries to pack the 3-D space with the icosahedral clusters, packing frustration arises again due to the incompatibility of the fivefold rotational symmetry with long-range translational order. Green solid arrow points to the optimal choice at each stage. [149]

II .3 Background of Fe-based MGs

II .3.1 Devitrification Behavior in Fe-B system

To elucidate the thermodynamics behind crystallization processes, it is useful to consider a hypothetical free energy diagram for the Fe-rich Fe-B alloy system.[159] As shown in **Fig. 15**, in binary Fe-B alloy system, we encounter two stable phases: α-Fe and Fe_2B, while Fe_3B presents itself as a metastable phase. The driving force propelling the transformation from the amorphous or glassy state to the crystalline phases is characterized by the difference in free energy between the glass or liquid and the pertinent crystalline phases. There are three crystallization reactions that amorphous alloys can follow[160]:

Polymorphic Crystallization: This process involves the transformation of the amorphous alloy into a supersaturated solid solution, metastable phase, or a stable crystalline phase without altering its composition. It closely resembles the transformation observed in pure metals or compounds. Polymorphic crystallization is feasible when the glassy phase transitions into, for instance, the Fe_3B phase (as seen in reaction 3).

Eutectic Crystallization: Eutectic crystallization is marked by the simultaneous crystallization of two or more phases. Subsequent decomposition can occur through reactions 2 or 4, resulting in a mixture of α-Fe and Fe_3B or Fe_2B. This process involves the separation of the reaction front into two distinct phases and typically proceeds at a slower pace compared to polymorphic crystallization. Eutectic crystallization boasts the highest driving force and can manifest across a wide range of concentration variations.

Primary Crystallization: This process revolves around the initiation and growth of a single crystalline phase with a composition differing from that of the matrix. For instance, reaction 1 in **Fig. 15** illustrates the free energy change during crystallization in amorphous matrix until equilibrium is attained. The primary crystalline phase can be either a terminal solid solution or an intermediate compound phase. The morphology of the primary crystal varies, ranging from spherical to highly dendritic, and is contingent on the solute compositions.

The primary crystallization behavior in Fe-B amorphous alloys has opened exciting possibilities for their use as magnetic materials. Just as in the case of Al-based metallic glasses, when Fe-based amorphous alloys go through primary crystallization, high density of BCC-Fe nanoparticles are formed in amorphous matrix. These particles allow Fe-based MG to become advanced soft magnetic materials, featuring a higher saturation magnetization when compared to their monolithic Fe-based MG counterparts.[31,32,161]

These Fe-based amorphous/nanocrystalline alloys find practical applications in various fields, including distribution transformers, reactors, and other devices. Their utility extends to power supplies, switching power supplies, instrumentation, vehicle electronics, mining and petroleum operations, and solar energy. Specific examples of these applications are detailed in **Fig. 16**.

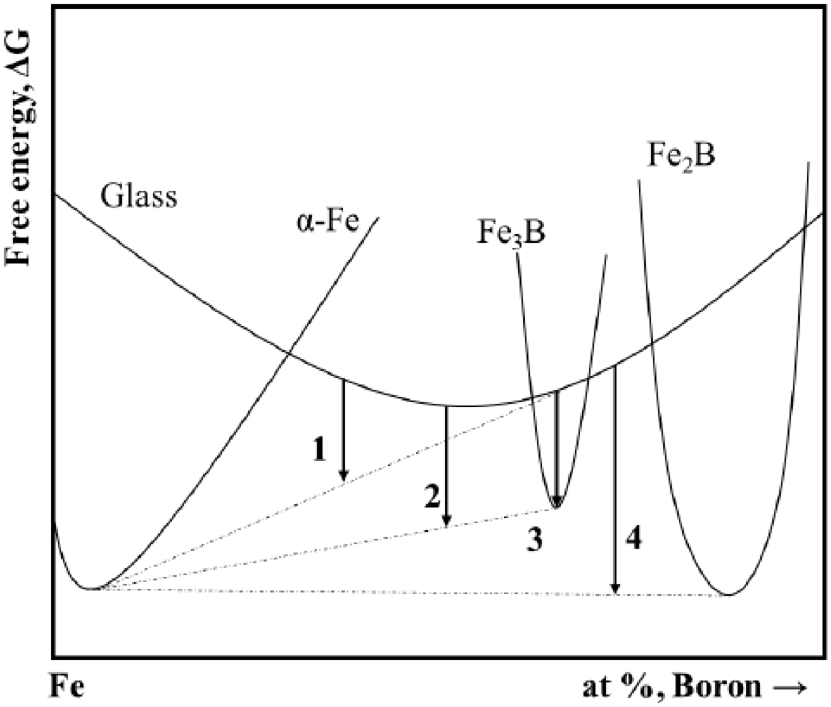

Fig. 15 Free energy vs. composition diagram for the Fe-rich Fe–B alloy system

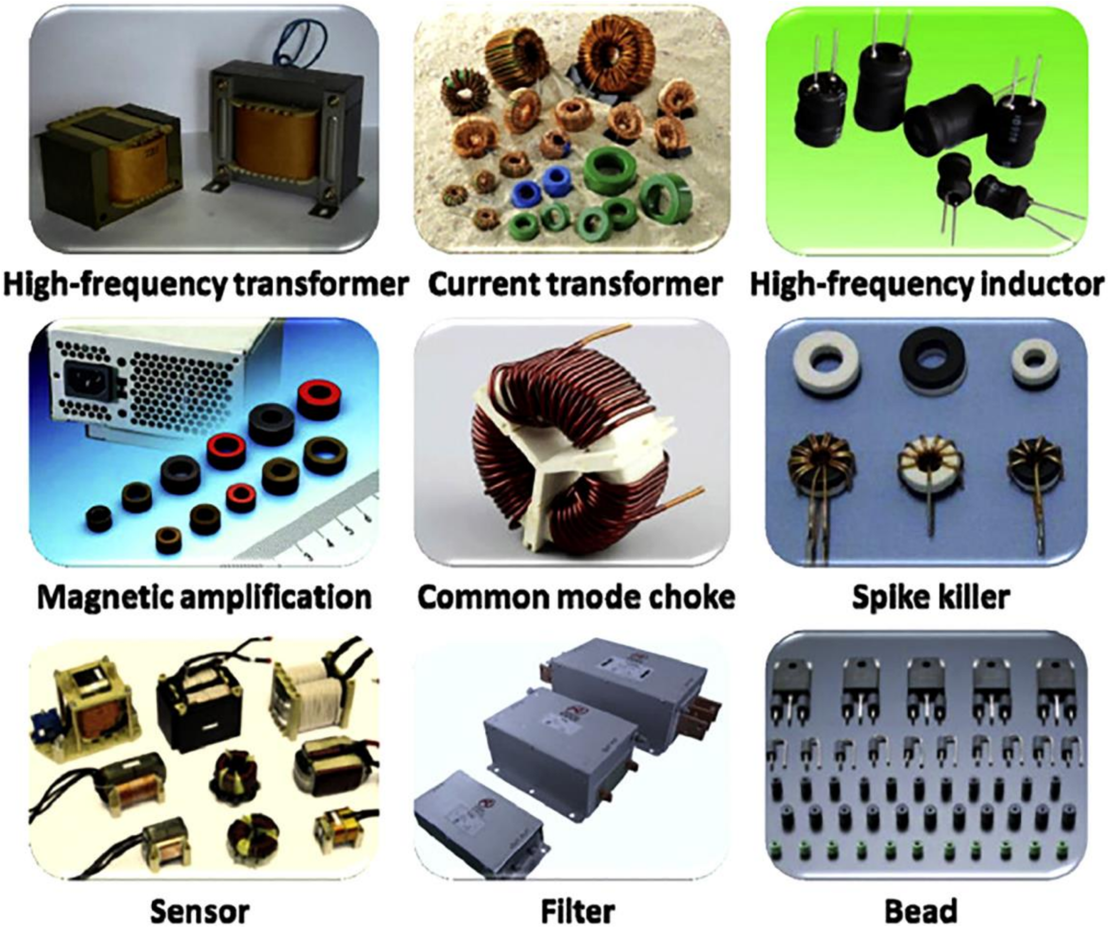

Fig. 16 Various cores fabricated by Fe-based amorphous/nanocrystalline soft magnetic ribbons. [162]

II .3.2 Alloy Design to Improve Magnetic Properties

The design of compositions for Fe-based amorphous/nanocrystalline alloys currently lacks precise quantitative criteria. Instead, specific compositions are typically determined through empirical guidelines and experimental trial and error. Recently, some composition design criteria have emerged, but they are often system-specific and not universally applicable. These empirical rules can be summarized as follows [163–165]:

First, Inoue's empirical principle suggests that an alloy should consist of three or more components with a substantial difference in atomic radius ratios (over 12%). The three primary components should have a negative heat of mixing, with larger negativity being preferred. A strong interaction between components is desired. Furthermore, a continuous change in atomic radii increases the viscosity of the supercooled liquid, facilitating the formation of a closely packed structure that hinders long-range atomic diffusion and inhibits crystallization, making it easier for the alloy to adopt a glassy structure.

Second, the eutectic point principle indicates that a lower reduced glass transition temperature makes it easier to form amorphous and deep eutectic alloy solutions. Lower temperatures help maintain the liquid structure, and the interval between the melting point and the glass transition temperature is reduced during cooling, shortening the time available for crystallization. Compositions at the eutectic point are distant from those forming stable compounds, making it challenging for crystals to grow and favoring the formation of amorphous structures.

Third, the principle of confusion suggests that increasing the degree of atomic mismatch between components increases structural complexity, supercooled liquid viscosity, and the likelihood of forming stable compounds. This, in turn, makes it easier for the alloy to adopt a glassy structure.

Many researchers have concentrated on Fe-based amorphous/nanocrystalline alloys with high B_s and high μ_e. As shown in **Fig. 17**, these materials outperform silicon steel, ferrite, and permalloy in terms of comprehensive properties. To enhance magnetic performance, researchers have explored the influence of nonmagnetic additives on controlling the crystallization process. The exclusion rules for these elements are (1) gas elements; (2) positive or small negative mixing enthalpies with Fe; (3) precious metals; (4) element that is prone to form refractory compounds with Fe because refractory compounds such as oxide inclusions act as hetero-nuclei that decrease the GFA greatly; (5) rare earth elements, which drastically decrease Bs and toughness; (6) radioactive elements; (7) rare elements; (8) toxic elements; (9) anti-ferromagnetic elements, which can improve the anti-corrosion properties but drastically decrease B_s. Researchers have also considered the atomic radius difference between Fe and other elements, mixing, and other factors. **Table 2** summarizes some elements which have been introduced into Fe-B system from different research reports. These reports have been used to guide the preparation of Fe-based amorphous alloys. However, it is worth noting that these nonmagnetic additives can have adverse effects on B_s, limiting the enhancement of B_s to around 1.9 T.[36]

Fe-based nanocrystalline alloy soft magnetic materials exhibit remarkable soft magnetic properties. This excellence stems from the disordered atomic arrangement inherent in nanocrystalline materials, which eliminates crystal anisotropy. As a result, nanocrystalline magnetic cores have high magnetic permeability, which provides good magnetism. In the pursuit of achieving a refined microstructure without relying on nonmagnetic additives, a new processing method involving crystallization during rapid heating has been proposed. By increasing the heating rate, the diameter of primary BCC-Fe crystals that precipitate from the amorphous matrix in binary metallic glasses, such as $Fe_{87}B_{13}$ [37]and $Fe_{86}B_{14}$ [38] , has been significantly reduced. These structural changes effectively lower the Hc of binary Fe-B alloys while simultaneously raising Bs beyond 1.9 T.[37] To gain better control over primary crystallization in Fe-B amorphous alloys, it is essential to study the nucleation mechanism of Fe-B MGs.

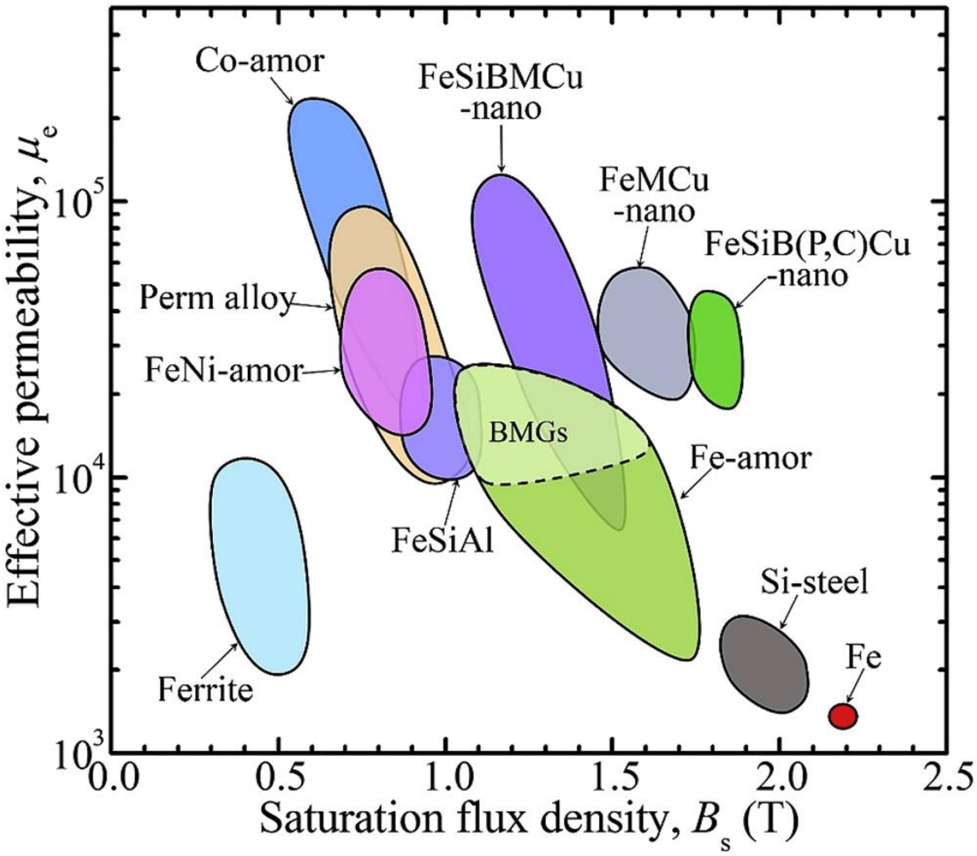

Fig. 17 The relationship between permeability (μe) at 1 kHz and saturation flux density (Bs) of soft magnetic materials. Reproduced with permission [166]

Table 2 The role of minor alloying elements in Fe-based amorphous/nanocrystalline alloys [167]

Element	Role	Advantages	Disadvantages
Silicon	Promote the GFA	Improving the high temp. magnetic properties	Bs↓
Boron	Promote the GFA	Decreasing the grain size	ΔT↓, decrease vol. % of α-Fe, Bs↓, not more than 10 at. % to be added
Copper	Grain refiner	μi↑, Hc↓, ΔT↑	No effect if Cu > 1.5 at.%
Niobium	Control the grain size	Impeding of Fe_2B formation, ΔT↑	No effect if Nb > 3 at.%, Bs↓
Zirconium	Control the grain size and promote the GFA	μi↑, Hc↓, core loss↓	Bs↓, casting problem
N-doping	Control the grain size	Bs↑, Hc↓	Using ammonia (explosive)
Phosphorous	Control the grain size	μi↑, Hc↓	Bs↓, casting problem
Nickel	(Fe, Ni) system	Improving the high temp. magnetic properties	Tc↓ (if Ni > 60 at. %), Bs↓ (at ambient temp.)
Cobalt	(Fe, Co) system	Improving the high temp. magnetic properties, ΔT↑, slowing down the precipitation of Fe_2B	Increase the cost, Bs↓ (at ambient temp.)
H-doping	N/A	Bs↑ (slightly), Tc↑	μi↓
Germanium	Control the grain size	Improving the high temp. magnetic properties, ΔT, Tc↑	GFA↓
Tungsten	Control the grain size	Tc↑, μi↑	Bs↓

Chapter III: Experiment Procedures

III .1 Sample Preparation

III .1.1 Arc Melting

The ingots with compositions of $Al_{88}Y_7Fe_5$, $Al_{87}Y_7Fe_5Cu_1$, $Al_{86}Y_7Fe_5Cu_2$, $Al_{84}Y_7Fe_5Cu_4$, $Al_{88}Y_7Fe_4Cu_1$, $Al_{88}Y_6Fe_5Cu_1$, and $Fe_{85}B_{15}$ were produced by arc melting. Preparation of the alloy ingots with the desired composition was conducted from high-purity elements. The mixtures of high-purity elements (99.999% Al, 99.98% Y, 99.99% Fe and 99.99% Cu) were placed on a water-cooled copper hearth inside of the vacuum chamber of arc-melter. The chamber was first evacuated to a high vacuum state of 2.0×10^{-5} torr and then back-filled with pure argon gas at a pressure of 0.5 atm. To further ensure purity, a pure Ti ingot was melted inside the melter to absorb residual oxygen. The mixtures of elements were melted with the arc plasma generated from the tungsten electrode and re-melted five times to ensure homogeneity.

III .1.2 Melt Spinning

The arc-melted alloy ingots were initially crushed to the appropriate size for placement inside a quartz tube. To regulate the liquid injection volume, a 1.0 mm diameter nozzle hole was drilled into the quartz tube. The quartz tube was then installed within the melt-spinner. As shown in **Fig. 18**, The chamber was evacuated and filled with pure argon gas at a pressure of 0.5 atm. Then, the alloy section was re-melted through induction heating and injected onto a rotating copper wheel with a tangential velocity of

55 m/s. This process produced ribbons that were approximately 20 μm thick and 2 mm wide.

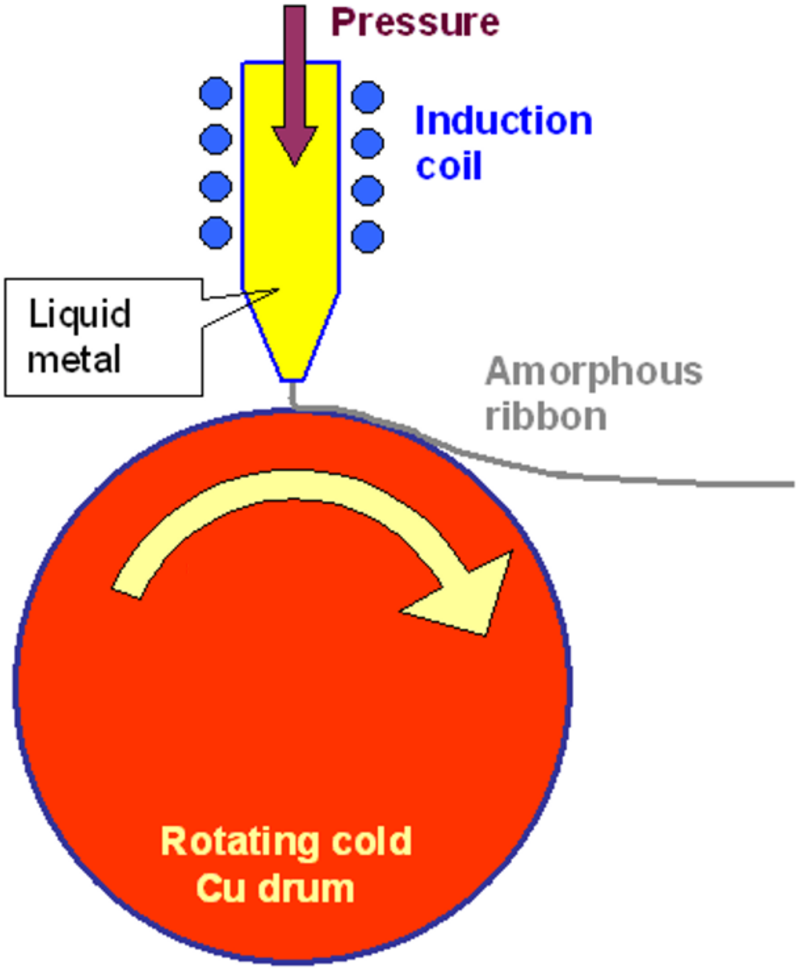

Fig. 18 Schematic illustration of the melt spinning apparatus.

III .2 Materials Characterization

III. 2.1. X-ray Diffraction

XRD measurements of Al-Y-Fe-(Cu) samples and Fe-B samples were performed on a Bruker D8 Discovery X-ray diffractometer. The samples were placed on the zero-diffraction plate during the XRD test. The 2θ range is 10-80˚. The data acquisition time is 200s for each increment of 5˚ under the Bruker XRD measurement. Structure analysis such as raw data exportation and phase identification is performed with the Bruker Eva software for the Bruker XRD data. Background correction was done through Origin Software by subtracting the baseline.

III. 2.2. Differential Scanning Calorimetry

DSC is a thermos-analytical technique in which the sample and reference are maintained at the same temperature and the difference in the amount of power flow W required to increase the temperature of a sample and the reference is measured. The constant pressure heat capacity C_p could be obtained through the DSC measurement.

A Perkin Elmer Diamond DSC was used for the isothermal annealing and continuous heating investigations. The sample is sealed in an aluminum pan because the upper temperature limit is below 600˚C. The sample weight is between 2 mg to 10 mg and the measured DSC signal is normalized from the weight. The temperature and heat flow were routinely checked and calibrated using indium, lead, and zinc samples. For the isothermal treatments, samples were heated to 200°C at a heating rate of 250 K/min and then to the targeted temperatures at 20 K/min to minimize the temperature overshot. The isothermal annealing temperatures were chosen so that the number of the Al nanoparticles is neither too large nor too small to be counted accurately from the TEM images. After the isothermal treatments, the samples were rapidly cooled to the room temperature at -250 K/min. The fast heating and cooling rates were used to avoid crystallization during the heating and cooling steps. The non-isothermal runs were performed under a constant heating rate of 20 K/min.

III. 2.3. Flash Differential Scanning Calorimetry

Fast scanning chip calorimeter, which is known as Flash-DSC (Flash DSC 2+, Mettler Toledo, **Fig.19 (a)**) was used to perform isothermal and continuous thermal scanning at fast heating rates. As shown in **Fig.19 (b)**, metallic glass ribbon samples were cut into the small pieces (smaller than 0.1 X 0.1 mm^2), and loaded on the MultiSTAR UFS 1 MEMS chip sensors. To attach the samples with rough surfaces with the thermal sensor, a little drop of distilled water was applied to the sensor with the sample. Distilled water can glue the sample onto the thermal sensor and does not damage thermal sensor or sample

III. 2.4. Microscopy Analysis

Al-based MGs specimens for TEM characterizations were thinned by ion milling (Prep Fischione Model 1050). Cross section samples prepared by using a double layered ion beam (±6°) at 3.5 kV. Ion milling was performed in an inert argon atmosphere and low temperature (liquid nitrogen, -150℃) to prevent oxidation and further nucleation. The ribbon specimen to be mounted in the specimen holder is smaller than the required diameter value of 3 mm. When mounting the sample to the TEM Cu grid, heating on the hot stage is avoided and leaving the sample at room temperature in a vacuum container will make the glue effective.

Fe-B Specimens were thinned to be electron transparent through focused ion beam (FIB) by a Thermo-fisher Helios PFIB. For the rough milling, the FIB voltage is 30 kV and the current decreased from 600 mA, 300 mA, 140 mA, 80 mA, 50 mA to 20 mA with the sample thickness decreasing. As a final milling procedure, a low kV polish (2kV, 100 mA) was performed to remove the amorphized material on the surface of the lamellae created by the high energy FIB under 30 kV.

TEM for nanocrystal characterization was finished by FEI Tecnai TF30. The nanocrystal of number density was measured in three different areas of each sample. Dark field images of the same location were employed to ensure an accurate number density determination. The thickness of sample was measured through EELS based on the log-ratio technique [168]:

$$\frac{t}{\lambda} = Ln(\frac{I_t}{I_0}) \qquad \text{Eq.14}$$

where it is the total number of electrons incident on the sample, I_0 is the number of un-scattered electrons, t is the thickness of the sample and λ is the scattering mean free path.

Fig. 20 shows the measurement of λ of Al-based MGs samples with different thickness were made by FIB. The thickness of each sample was measured through SEM. After measuring I_t and I_0 through EELS on TF30, λ could be calculated from Eq.14. The value of λ for the Al-based sample is 191 nm.

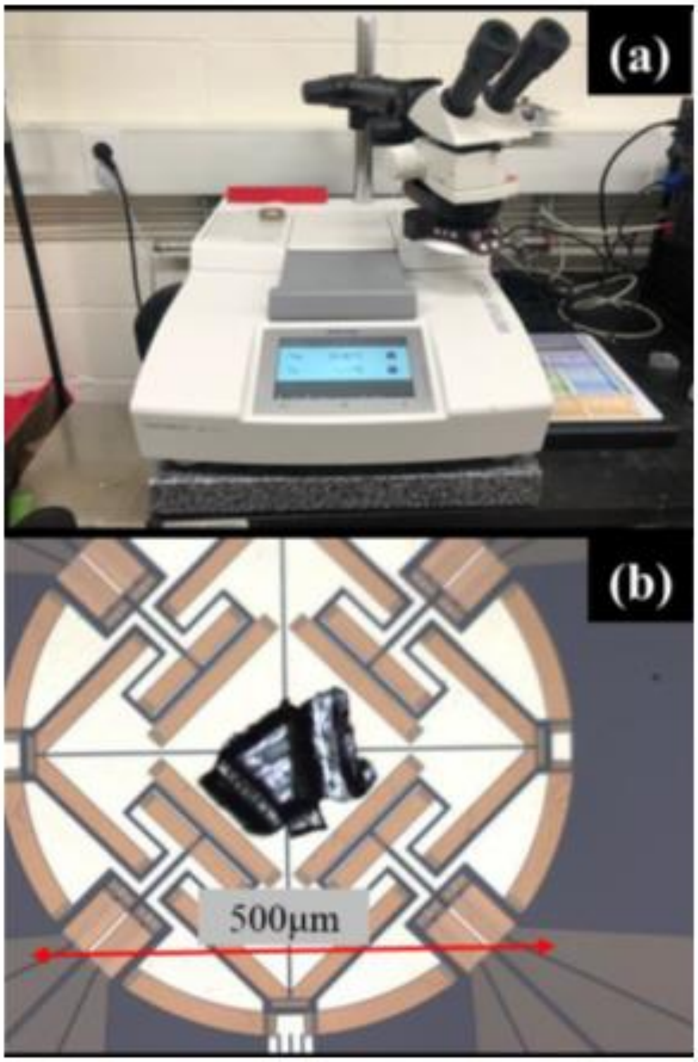

Fig. 19 (a) Flash-DSC 2+ used in this research and (b) optical microscopy image of the chip sensor with the metallic glass sample.

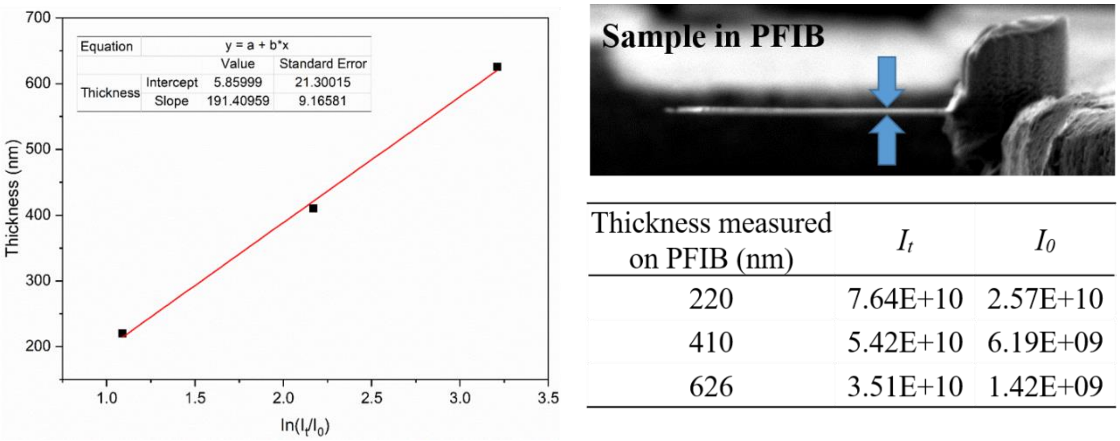

Thickness measured on PFIB (nm)	I_t	I_0
220	7.64E+10	2.57E+10
410	5.42E+10	6.19E+09
626	3.51E+10	1.42E+09

Fig. 20 Calibration of the scattering mean free path (λ=191 nm)

Chapter IV: Results and Discussion

IV.1 Nucleation Kinetics Studies for Primary Crystallization in Al-Y-Fe-Cu MGs

IV.1.1 Continuous Heating Treatment

The continuous heating trace for an amorphous $Al_{88}Y_7Fe_5$ sample at 20 K/min (**Fig. 21(a)**) shows the primary crystallization peak with the onset temperature at 540 K (267°C) and the sharp secondary crystallization peak starting at 638 K (365°C). The DSC trace of the crystallization products produced at different temperatures were analyzed by XRD (**Fig. 21(b)**). Prior to primary nucleation, the XRD shows an amorphous structure (**Fig. 21(b)**, curve 1). During the primary crystallization, the FCC-Al phase precipitates as a dispersion of nanocrystals surrounded by a glassy phase (**Fig. 21(b)**, curve 2). In summary, the crystallization pathway in $Al_{88}Y_7Fe_5$ is an initial primary reaction of FCC-Al from the matrix followed by the precipitation of intermetallic phases in the remaining sample volume at higher temperatures.

The shape of the primary crystallization signal (**Fig. 21(a)**) provides an indication of the controlling kinetic behavior. The initial onset of the reaction is sharp, and the heat evolution increases with increasing temperature, indicating rapid progress of the reaction. However, after the peak, the rate slows to reveal a large asymmetry in the signal. The main reason for the tail in heat production at higher temperatures has been generally attributed to the increased solute level in the remaining matrix acting to slow the growth rate of the nanocrystal population[169]. The separation as large as 52 degrees between the primary and the secondary crystallization peaks indicates the good stability of the nano-crystallized Al-based metallic glasses.

Fig. 22(a) represents the measured DSC heat flow curves for every component substitution by 1 at. % Cu at 20K/min that were measured. The corresponding crystallization temperatures derived from DSC analysis are provided in **Table 3**. It is quite noticeable that 1 at. % replacement of Al, Y, and Fe with Cu in the $Al_{88}Y_7Fe_5$ alloy brings about significant changes in the primary crystallization temperature. Substituting Y and Fe with Cu results in a substantial 46°C and 45°C decrease in T_{x1}, respectively, whereas the replacement of Al with Cu leads to an 11°C increase in T_{x1}. This outcome suggests that replacing 1% of Al with Cu in the $Al_{88}Y_7Fe_5$ amorphous alloy delays the initiation of primary crystallization, while substituting Y and Fe with Cu significantly accelerates the primary crystallization by lowering the primary crystallization onset temperature.

Considering that the 1 at. % Cu substitution does not exert a substantial influence on the thermodynamic driving free energy for nucleation and any alterations in the glass-to-crystal interfacial energy due to Cu segregation remain independent of the substituted component, these factors do not account for the notable changes in the observed primary crystallization onset temperatures. Nevertheless, because the crystallization onset temperature is sensitive to the delay time, it becomes necessary to investigate the evolution of delay time with minor alloying in order to understand the underlying physical mechanisms affecting nucleation and crystallization.

Since adding 1 at. % of Cu instead of Al increases T_{x1}. More Cu content was added into the system. Fig. 22(b) represents the measured DSC heat flow curves for Al substitution by 2 at. % and 4 at. % Cu at 20K/min. It turns out that T_{x1} drops after adding 2 at. % Cu, which means the thermal stability of $Al_{86}Y_7Fe_5Cu_2$ is relatively low compared to $Al_{87}Y_7Fe_5Cu_1$. From the simulation results from Y. Liu at. el.’s research[156] , adding 1% Ag to the Al-Ni-Y system enhances GFA by acting as "glue" atoms to strengthen the glassy structure. However, after increasing the content of Ag to 2%, Ag may affect the formation Ni-centered polyhedral clusters. New Y-centered polyhedral clusters with coordination number of 10-13 appears in the alloy, which lead to GFA decreasing. Cu may have the similar effect as Ag in Al-Y-Fe system, but further research is required. After adding 4 at. % Cu into the system, there is no primary crystallization in $Al_{84}Y_7Fe_5Cu_4$ MG. The Al content is low enough to form eutectic phase instead of pure FCC-Al.

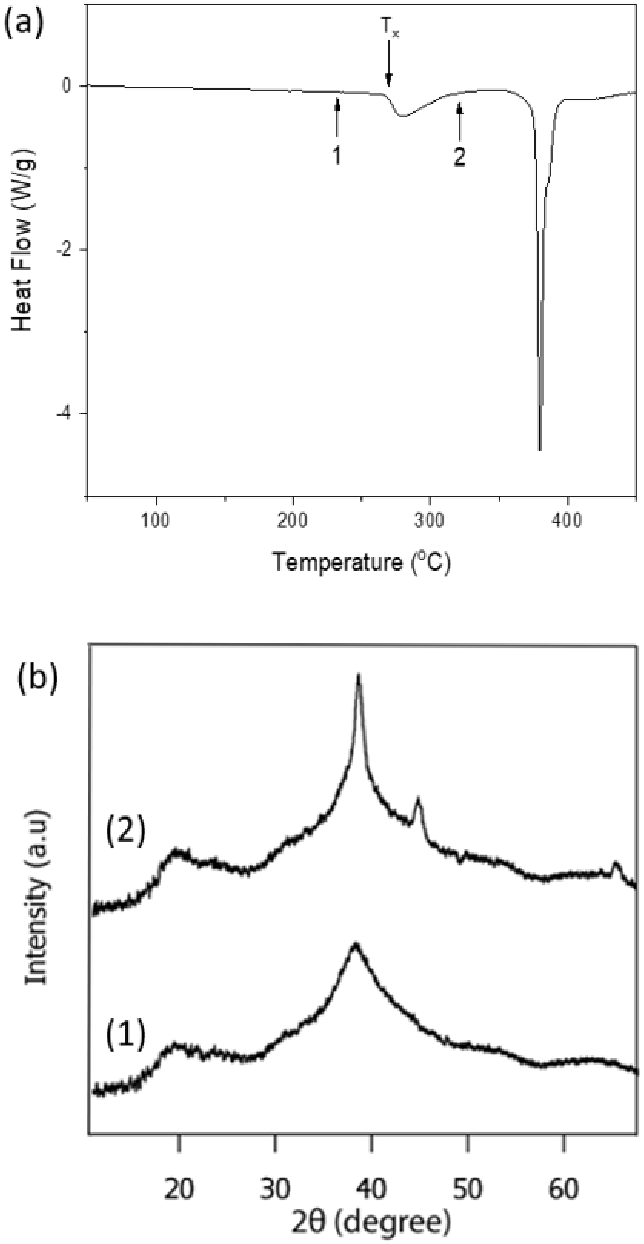

Fig. 21 (a) Continuous heating DSC trace (20 K/min) of $Al_{88}Y_7Fe_5$ metallic glass. The onset temperature for the primary crystallization is at 267°C. (b) The XRD traces corresponding to different annealing products from heating to different labeled temperatures.

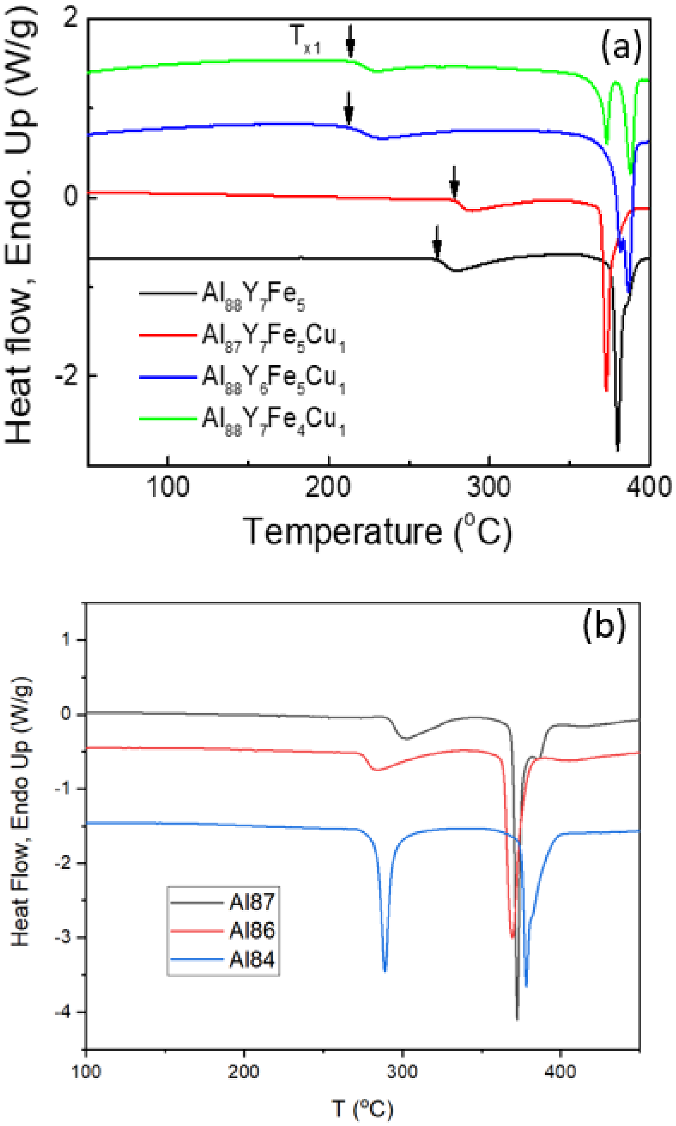

Fig. 22 (a) Heat flow curves by normal DSC at 20K/min for 1at. % Cu-doping in $Al_{88}Y_7Fe_5$ systems. The down black arrows point to the onset temperature of primary crystallization. (a) Heat flow curves by normal DSC at 20K/min for 2 at. % and 4 at. % Cu-doping instead of Al in $Al_{88}Y_7Fe_5$ systems.

Table 3 Summary of thermodynamic properties in different compositions by Cu-doping in $Al_{88}Y_7Fe_5$ system. The black up and down arrows give the increasing and decreasing trends compared to the values of $Al_{88}Y_7Fe_5$.

Composition	**T_{x1} (ºC)**	**T_{x2} (ºC)**
$Al_{88}Y_7Fe_5$	266	373
$Al_{87}Y_7Fe_5Cu_1$	277↑	369↓
$Al_{88}Y_6Fe_5Cu_1$	220↓	375↑
$Al_{87}Y_7Fe_4Cu_1$	221↓	365↓

IV.1.2 Isothermal Annealing Treatment

Isothermal annealing treatments provide information such as the number density, crystal size distribution as well as the transient delay time. The details of the heat treatment schedule are shown in **Fig. 23(a)**. In order to gain a perspective on the reaction progress with time at a single temperature, a comparison of XRD traces for $Al_{88}Y_7Fe_5$ samples annealed at 245 °C for various times is given in **Fig. 23(b)**. A broad peak, characteristic of an amorphous structure, centered at about the solvent species interatomic distance, is present in all traces. With the increased annealing time, the broad peak at $2\theta=38°$ (111) sharpens while peaks at 45° (200) and 65° (220) begin to rise out of the baseline indicating a growing volume fraction of aluminum nanocrystals. The qualitative X-ray information supplements quantitative TEM image analysis. Bright field TEM images from the samples annealed at the same temperature are given in **Fig. 24**, showing that the Al particle number density increases with the annealing time.

The isothermal annealing tests for the other three Cu doping compositions yielded similar results. **Fig. 25** represents bright field TEM images of $Al_{87}Y_7Fe_5Cu_1$ annealed at 245℃ for different durations. It is evident that the number density of Al particles increases with longer annealing times.

Fig. 26 compares TEM images from samples with different compositions. After annealing at temperatures below T_x, the size of Al particles formed in $Al_{87}Y_7Fe_5Cu_1$ is as similar as those formed in $Al_{88}Y_7Fe_5$. However, Al particles formed in $Al_{88}Y_7Fe_4Cu_1$ and $Al_{88}Y_6Fe_5Cu_1$ are notably smaller in size than in the other two compositions.

Although without the detailed thickness measurement for each TEM samples, it is apparent that the area number density of nanoparticles formed in in $Al_{88}Y_7Fe_4Cu_1$ and $Al_{88}Y_6Fe_5Cu_1$ annealing at 190 ℃ is significantly higher than in $Al_{88}Y_7Fe_5$ and $Al_{87}Y_7Fe_5Cu_1$ annealing at 240 ℃ (both annealing temperature is around 90% of T_x). To delve deeper into the analysis of nucleation behavior for each composition, we applied the thickness measurement method discussed in section III. 2.4 to study the nucleation density in each TEM sample. Further details regarding the density changes will be provided in the following sections.

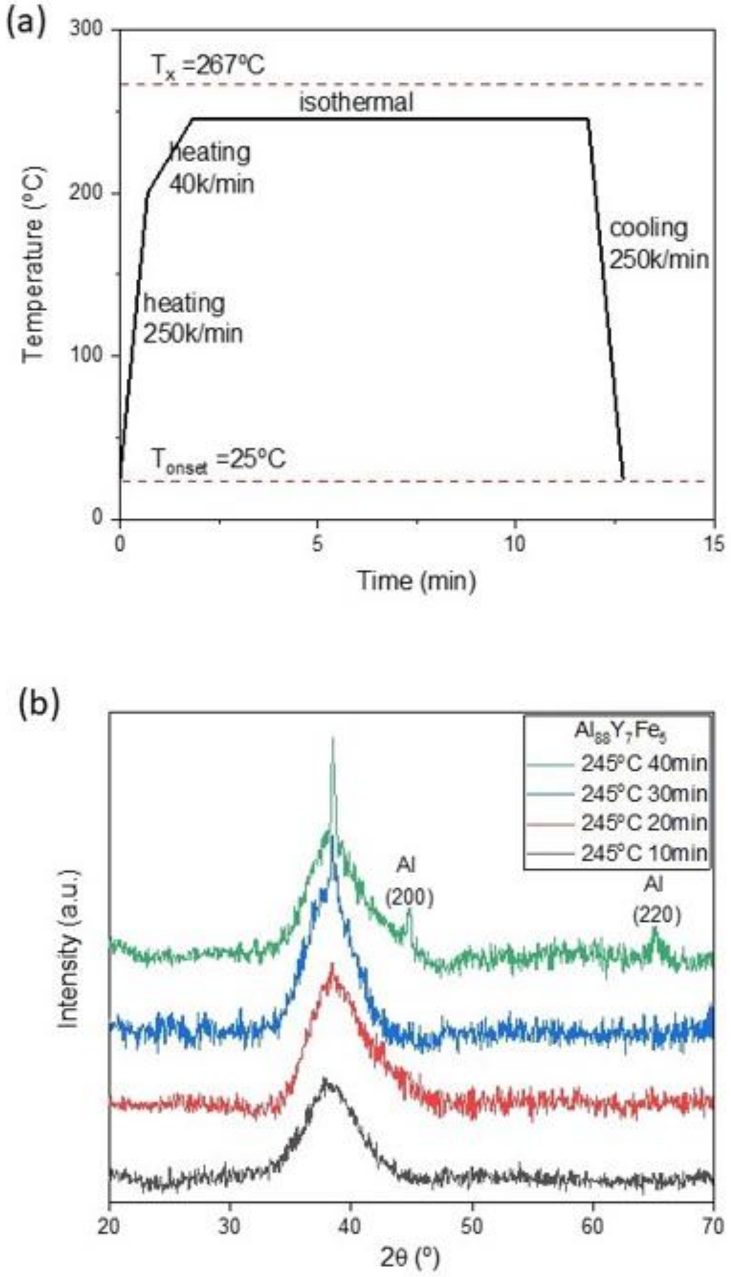

Fig. 23 (a)Schematic illustration for annealing treatments. (b)X-ray traces for $Al_{88}Y_7Fe_5$ annealed for various times at 245°C.

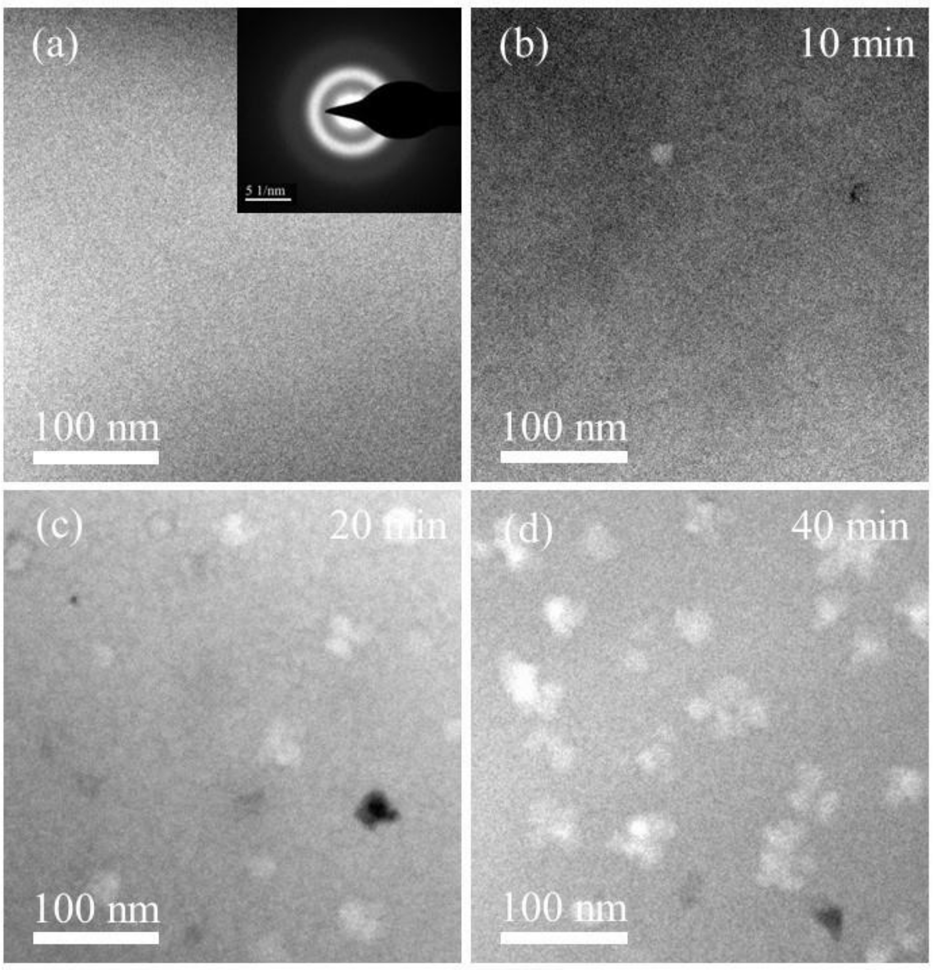

Fig. 24 Bright field TEM images for $Al_{88}Y_7Fe_5$ annealed for various times at 245°C. (a) as quenched, (b) 10 mins, (c) 20 mins and (d) 40 mins.

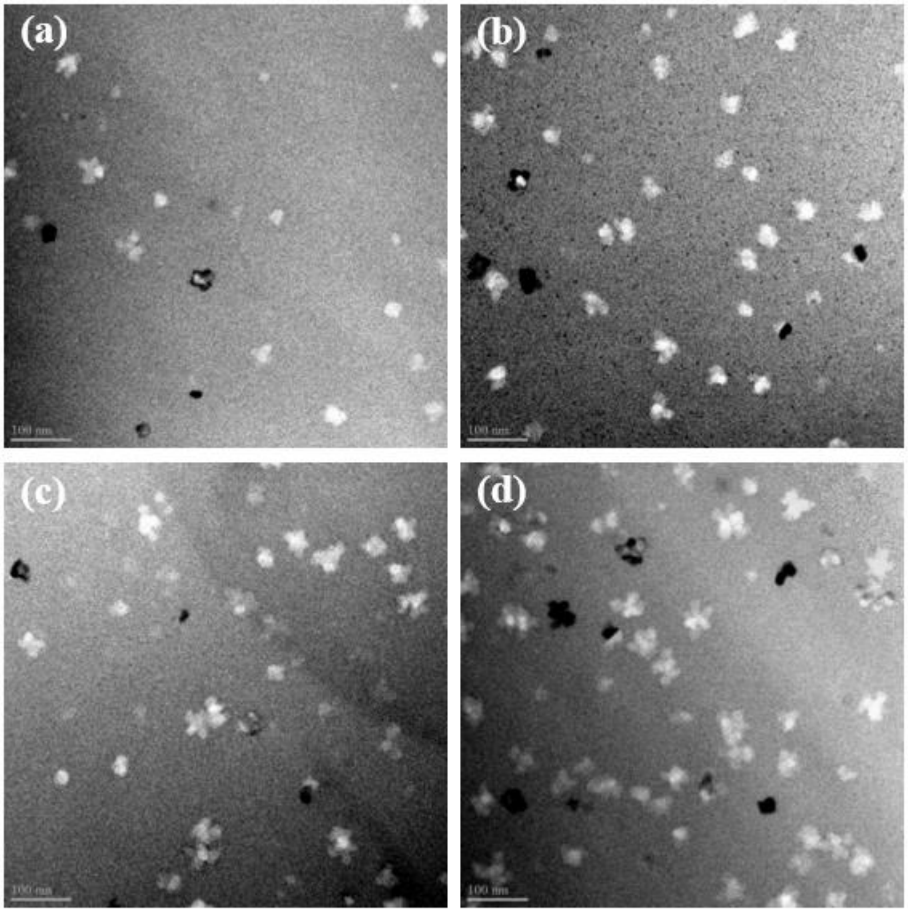

Fig. 25 Bright field TEM images of $Al_{87}Y_7Fe_5Cu_1$ which annealed under 245°C for different time range: (a) 3000s, (b) 5000s, (c) 7000s and (d) 9000s.

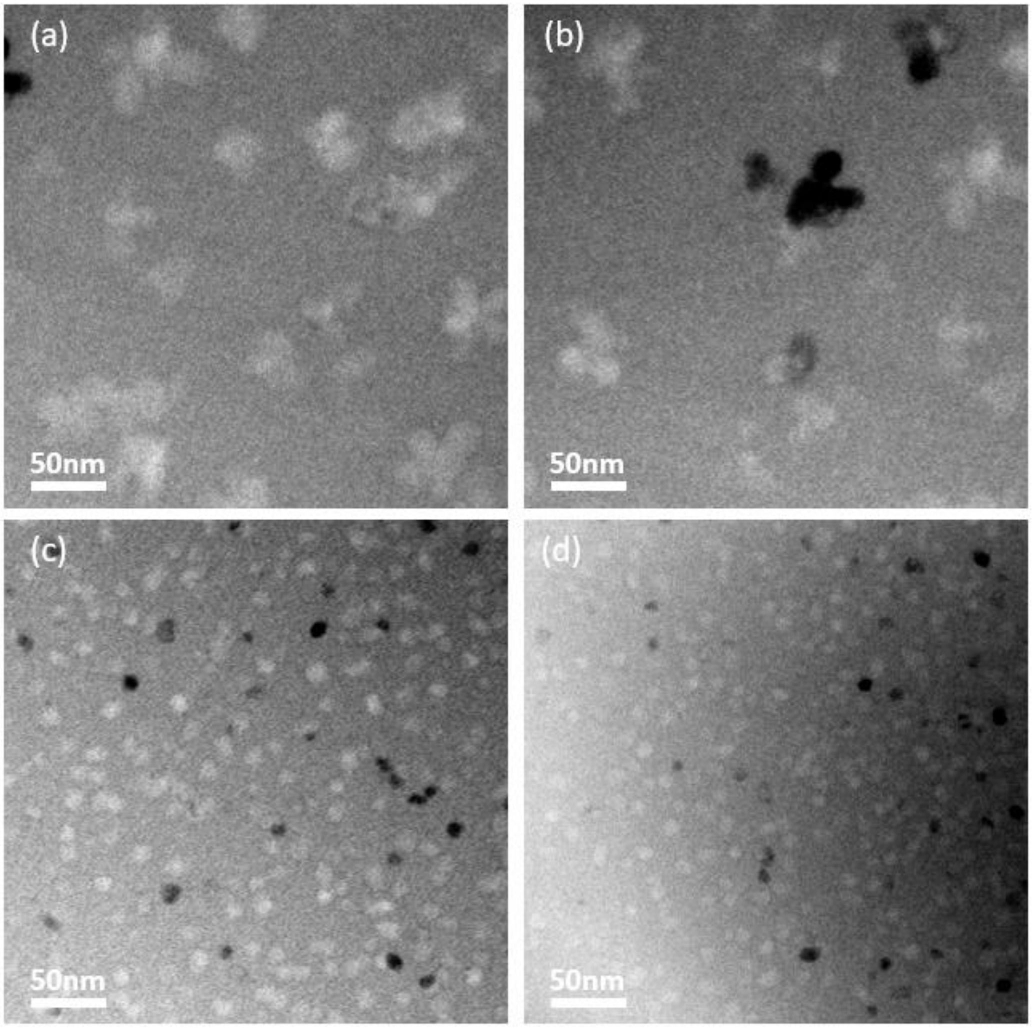

Fig. 26 Bright field TEM images of $Al_{88}Y_7Fe_5$, $Al_{87}Y_7Fe_5Cu_1$, $Al_{88}Y_7Fe_4Cu_1$, and $Al_{88}Y_6Fe_5Cu_1$ after annealing

IV.1.3 Delay Time Measurement by Flash-DSC

In marginal Al-based MGs, the glass transition signal often gets obscured by the primary crystallization process. Therefore, traditional DSC tests are not suitable for accurately pinpointing the glass transition temperature. However, this challenge can be overcome with Flash DSC. **Fig. 27** displays a set of heat flow curves for $Al_{87}Y_7Fe_5Cu_1$, measured using Flash DSC at a heating rate of 1000K/s. In this curve, both the glass transition signal and the crystallization signal are clearly discernible.

$Al_{87}Y_7Fe_5Cu_1$ samples were annealed at 245 ^{o}C for varying durations, ranging from 10 seconds to 7000 seconds. As the annealing time increases, the glass transition temperature shifts to higher values. This trend is also observed in other compositions. The plots of glass transition temperature against different annealing times for $Al_{87}Y_7Fe_5Cu_1$, $Al_{88}Y_6Fe_5Cu_1$ and $Al_{88}Y_7Fe_4Cu_1$ are presented in **Fig. 28(a)**, **Fig. 28(b)**, and **Fig. 28(c)**. Notably, these plots exhibit a distinct break point in the evolution of T_g with annealing time. The behavior before and after this break point follows different paths.

In metallic glasses, the emergence of crystals within the glass matrix suggests a change in composition. As the annealing time at a specific temperature increase, the divergence in the evolution of T_g with annealing time before and after the appearance of crystals is due to a combination of relaxation effects and compositional effects. Consequently, the turning point in T_g with annealing time, shifting from the relaxation effect to the superimposed effect of relaxation and composition, corresponds to the delay time for primary crystallization. Detailed delay time values at various temperatures are listed in **Table 4**.

To further validate whether the break point in glass transition with annealing time corresponds to the delay time for primary crystallization, we examined TEM images before and after this break point. As shown in **Fig. 29(a)**, at 247°C, the sample annealed for 1000 seconds remains amorphous. Conversely, for samples annealed beyond the break point for 3000 seconds, precipitated Al-fcc nanocrystals could be detected (**Fig. 29(b)**). These findings confirm that the delay time measurement method based on Flash DSC is both feasible and reliable, particularly for marginal Al-based metallic glass systems.

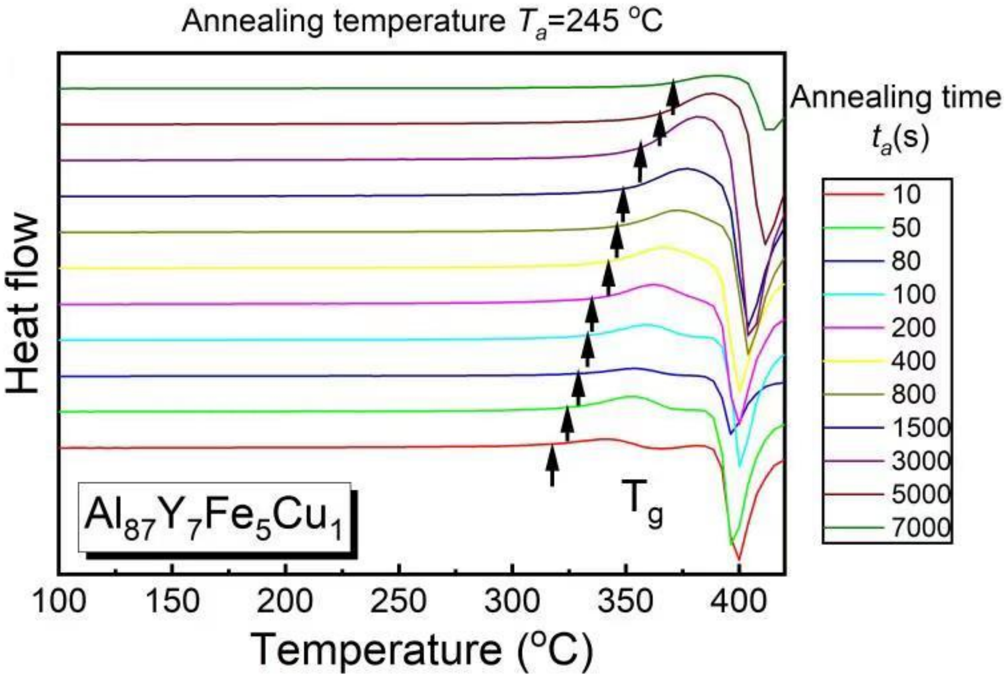

Fig. 27 A series of Flash DSC heat flow curves at 1000 K/s for $Al_{87}Y_7Fe_5Cu_1$ correspond to different annealing time t_a ranging from 10s to 7000s.

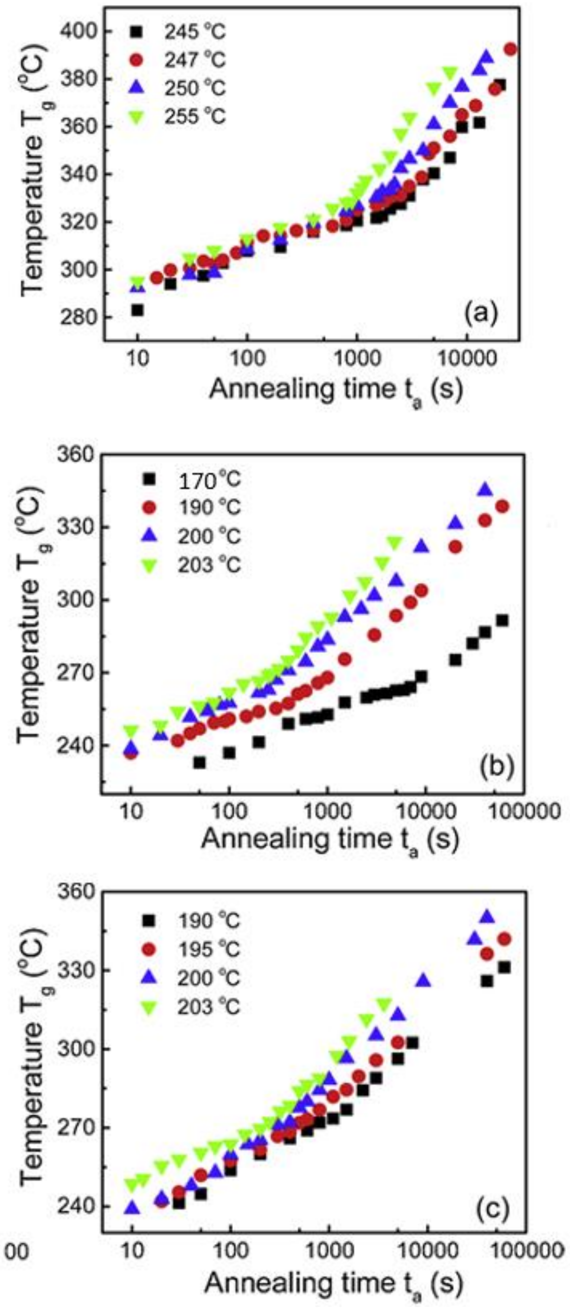

Fig. 28 Plot of glass transition temperature T_g and annealing time t_a (a) $Al_{87}Y_7Fe_5Cu_1$ annealing at 245°C, 247°C, 250°C and 255°C; (b) $Al_{88}Y_7Fe_4Cu_1$ annealing at 170°C, 190°C, 200°C and 203°C; (c) $Al_{88}Y_6Fe_5Cu_1$ annealing at 190°C, 195°C, 200°C and 203°C

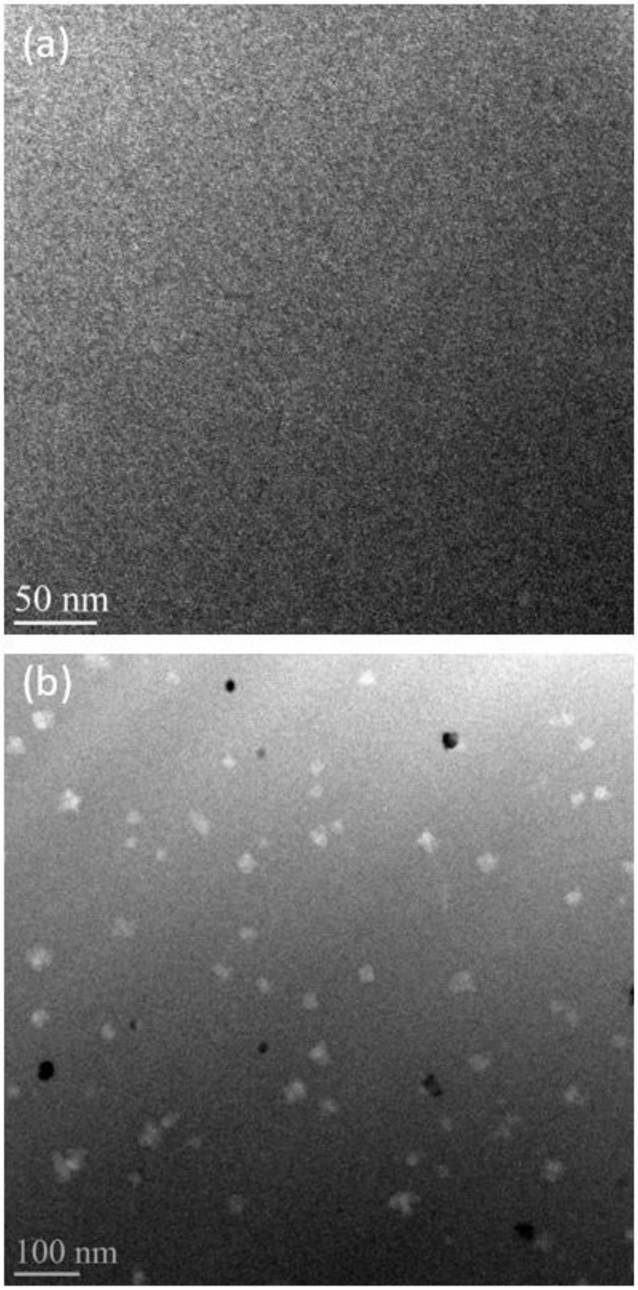

Fig. 29 Bright field TEM images of $Al_{87}Y_7Fe_5Cu_1$ annealing under 247 ^{o}C: (a) before break point, (b) after break point.

Table 4 Delay time τ for different temperature in compositions by minor-alloying in $Al_{88}Y_7Fe_5$ systems. (The delay time of $Al_{88}Y_7Fe_5$ is collected from Shen's work [20])

Composition	Annealing Temperature (ºC)	Delay time (s)
$Al_{88}Y_7Fe_5$	237	966
	240	525
	245	275
	247	225
$Al_{87}Y_7Fe_5Cu_1$	245	3027
	247	2380
	250	2036
	255	820
$Al_{88}Y_6Fe_5Cu_1$	190	1312
	195	780
	200	503
	203	344
$Al_{88}Y_7Fe_4Cu_1$	170	4645
	190	703
	200	359
	203	270

IV.1.4 Particle Density Distribution

The particle counting on the TEM images and the volume information obtained from the thickness measurement yielded the resulting nanocrystal number density for $Al_{88}Y_7Fe_5$ subjected to isothermal treatment at temperatures ranging from 237°C to 247°C (20 to 30 degrees lower than T_x) for various lengths of time (**Fig. 30**). An equivalent sphere method is used to quantify the size of the crystal where the crystal is treated as a circle with the same area. The temperature range was chosen so that the transient time was measurably large, but the crystallization reaction occurred over an accessible laboratory timescale. Similar plots have also been obtained by in situ x-ray powder diffraction measurement of the relative volume fraction of the crystalline component variation with time [170] or by integrating either the isothermal DSC trace [47] or the NMR spectra [50].

Similarly, **Fig. 31** presents a series of relationships between particle density and annealing time $Al_{87}Y_7Fe_5Cu_1$, $Al_{88}Y_7Fe_4Cu_1$, and $Al_{88}Y_6Fe_5Cu_1$. The observed behavior illustrates three distinct stages, corresponding to the transient stage, the steady nucleation stage, and the crystal growth stage.

During the transient stage, the nucleation rate is so low that it is not possible to detect nanocrystals under TEM. In the steady state nucleation stage, the nucleation rate remains constant and is represented by the slope of the curve which represents J_{ss}. By extrapolating the curve of steady-state growth, the point where it intersects the time axis indicates the delay time. In the crystal growth stage, a plateau is observed, indicating that the number density of particles remains constant. After this stage, no new nucleation occurs, but existing crystal particles continue to grow while also coarsening which is the coarsening state. The coarsening stage, where the crystal number density decreases as the largest crystals grow at the expense of the smallest ones, is not depicted in **Fig. 30** and **Fig. 31**, as the experimental annealing time was not long enough to reach this stage.

From both **Fig. 30** and **Fig. 31**, it is evident that as the annealing temperature decreases, the curves shift towards longer durations, resulting in an increased delay time and a decreased steady-state nucleation rate. Furthermore, the addition of just 1 at. % of Cu has a substantial impact. The maximum nucleation density of $Al_{87}Y_7Fe_5Cu_1$ is 1.5 (± 0.2) × 10^{21} m^{-3} at 255 °C, while the nucleation density of $Al_{88}Y_7Fe_4Cu_1$ can reach 2.7 (± 0.2) × 10^{22} m^{-3} at 203 °C.

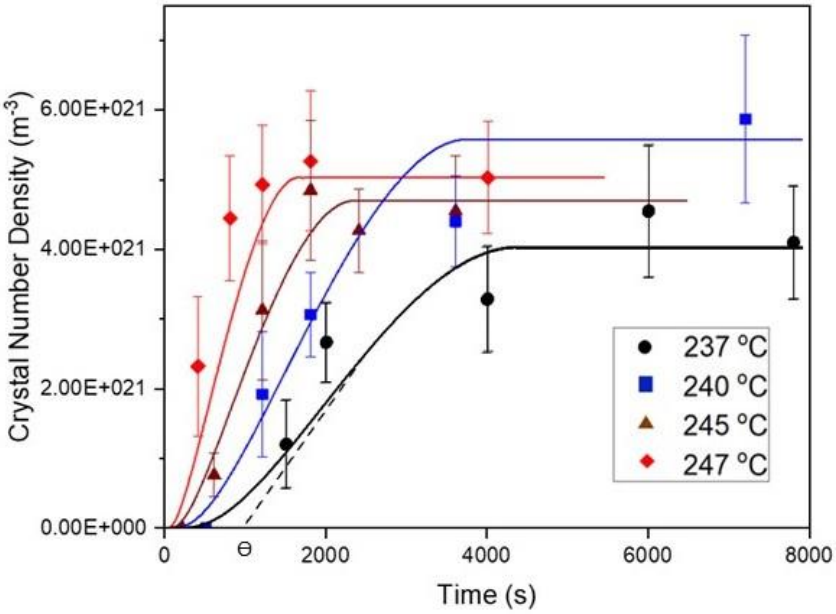

Fig. 30 The experimental (points) and calculated (solid curves) aluminum nanocrystal number density at various temperatures and times for $Al_{88}Y_7Fe_5$. θ is the intersection of the extrapolation of the nucleation curve and the time axis, which represents delay time.

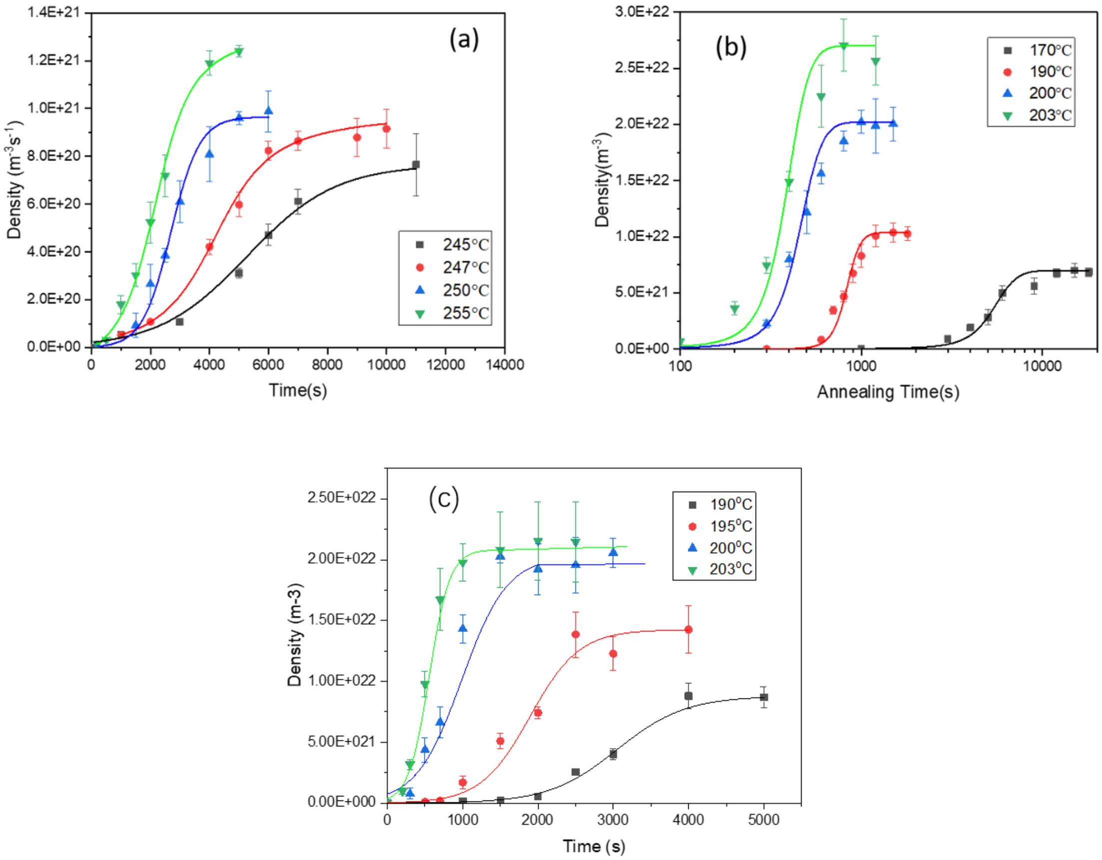

Fig. 31 The particle density vs. annealing time relationships for $Al_{87}Y_7Fe_5Cu_1$, $Al_{88}Y_7Fe_4Cu_1$, and $Al_{88}Y_6Fe_5Cu_1$. (a) $Al_{87}Y_7Fe_5Cu_1$ annealing at 245, 247, 250 and 255 °C; (b) $Al_{88}Y_7Fe_4Cu_1$ annealing at 170, 190, 200 and 203 °C; (c) $Al_{88}Y_6Fe_5Cu_1$ annealing at 190, 195, 200 and 203 °C.

IV.1.5 MRO Seeded Nucleation Model

FEM experiments were conducted on as-quenched Al-Y-Fe with or without Cu addition amorphous ribbons, then compared to electron scattering simulations from atomistic models to determine the size and volume fraction of the Al-like regions. The experiments, and analysis are described in detail elsewhere[26]. The conclusion is that the Al-like regions have a mean radius of about 0.85 nm and a number density of 2×10^{25} to 6×10^{25} m^{-3} in the as-quenched glass. The inherent MRO is different from the quench-in nuclei. Under CNT, density of Al nuclei formed in Al-Y-Fe MGs during quenching is calculated around 1×10^{13} m^{-3} in experimental temperature range, which is much lower than MRO density. (Appendix A). The detailed MRO information for each composition is listed in **Table 5**.

In the analysis of the primary crystallization kinetics in amorphous Al based alloys, it is recognized that the MRO regions are present within the melt-quenched amorphous phase as an inherent spatial heterogeneity. Based upon the structural heterogeneity, the crystallization kinetics can be analyzed by classical nucleation theory [171] with the MRO as the heterogenous nucleation site. The steady state nucleation rate can be expressed as:

$$J_{SS} = \rho\beta Z\, exp\left(-\frac{\Delta G^{*}(r)}{kT}\right) \qquad \text{Eq.10}$$

where ρ is the nucleation site density, β is the attachment frequency, Z is the Zeldovich factor accounts for the decay of supercritical clusters, $\Delta G^{*}(r)$ is the nucleation barrier and k is the Boltzmann constant.

For an idealized spherical cluster with a radius of r, which develops from an MRO region that is also treated as spherical of radius r_0 (**Fig. 6**), the overall work of cluster formation, $\Delta G(r)$ is obtained as[172]

$$\Delta G(r) = G_{crystal} - G_{amorphous}$$

$$= (\frac{4}{3}\pi r^3 \Delta G_V + 4\pi r_o^2 \sigma_{MRO\ /crystal} + 4\pi r^2 \sigma_{crystal\ /glass}) - (\frac{4}{3}\pi r_0^2 \Delta G_V + 4\pi r_0^2 \sigma_{MRO\ /glass})$$

$$= \frac{4}{3}\pi(r^3 - r_o^3)\Delta G_V + 4\pi(r^2 - r_o^2)\sigma_{crystal/glass} + 4\pi r_o^2 \sigma_{MRO/crystal} \qquad \text{Eq.15}$$

where ΔG_v is the volumetric driving free energy, $\sigma_{crystal/\ glass}$ is the nanocrystal-glass interfacial energy, $\sigma_{MRO/crystal}$ is the MRO-nanocrystal interfacial energy and $\sigma_{MRO/glass}$ is the MRO-glass interfacial energy. Because the MRO regions are viewed as defective Al crystals with no chemical difference between the MRO core and the Al crystal rim, there is an essentially low structural misfit at the MRO/crystal interface and complete wetting. Therefore, $\sigma_{MRO/glass}$ is regarded the same as $\sigma_{crystal/glass}$. Also $\sigma_{MRO/crystal}$ is estimated to be very small. Based on the interface energy of icosahedral quasicrystal/amorphous interfaces that are reported as 6~14 (mJ/m^2) [105,173], $\sigma_{MRO/crystal}$ is estimated to be about 9 (mJ/m^2). During crystallization, the MRO core with distorted Al-like order rearranges and merges into the nucleated nanocrystal (**Fig. 32(c)**) with negligible energy change. As noted in **Fig. 32**, the initial MRO/glass interface is replaced by the MRO/nanocrystal and nanocrystal/glass interfaces after crystallization.

To further test the validity of heterogenous nucleation model, the homogeneous nucleation of Al crystals was calculated. Without the MRO in system, $\Delta G(r)$ is obtained as

$$\Delta G(r) = \frac{4\pi}{3} r^3 \Delta G_V + 4\pi r^2 \sigma_{crystal/glass} \qquad \text{Eq.16}$$

where ΔG_v is the volumetric driving free energy, $\sigma_{crystal/glass}$ is the nanocrystal-glass interfacial energy. r is the radius of cluster. There is a maximum in ΔG occurring at the critical cluster radius (r^*), which is determined from $(d\Delta G/dr)|_{r=r^*}=0$.

$$r^* = -2\sigma_{crystal/glass} \,/\, \Delta G_v \qquad \text{Eq.17}$$

By inserting Eq. 16 and Eq. 17 into Eq. 10, the steady state nucleation rate can be calculated. The calculation result is plotted in **Fig. 33**. Compared to the experiment result, the homogeneous nucleation rate is 10^{13} times slower in experimental temperature range (237 to 247 ^{o}C). Besides, under homogeneous nucleation model, $\Delta G^*/kT$ is around 85, which is much higher than heterogenous nucleation ($\Delta G^*/kT$ is around 13). From the calculation, homogeneous nucleation cannot account for the nanocrystal number densities in the experimental temperature range due to the very low nucleation rate. Thus, the heterogenous nucleation model is more appropriate.

The parameters used in Eq. 15 have been evaluated to determine predictions for the nucleation rate. The $\sigma_{crystal/glass}$ value is calculated to be $(0.16\pm0.003) +10^{-5}T$ (J/m^2) through the method developed by Spaepen (Appendix B). The driving free energy, ΔG_v based on the parallel tangent construction (Appendix C), is -1.0185×10^6 $(T-T_l)$ J/m^3 within an error range of $(2.0941\sim0.8823)\times10^6$ J/m^3 where T_l is calculated as 860±20 K. The r_0 value as 0.85 nm is obtained from FEM [26].

Each of the evolving clusters will grow and shrink at a rate determined by the attachment frequency across the matrix/cluster interface:

$$\beta = \frac{1}{2Z^2\tau} \qquad \text{Eq.19}$$

Where Z is the Zeldovich factor, τ is the delay time for nucleation and is defined as the time required to establish the steady-state nucleation in a system[172,174,175], which can be obtained from experiment.

By extrapolating the linear part of the particle number density vs. annealing time curve to intersect with the time axis (**Fig. 30** and **Fig. 31**), the delay time τ can be obtained. The value of τ at the four different temperatures for each composition are summarized in **Table 6**, **Table 7**, **Table 8**, and **Table 9** separately. Under the assumption that the delay time satisfies the Arrhenius relationship the temperature dependence of τ is given by

$$\tau = \tau_o\, exp(\,Q/RT) \qquad \text{Eq.20}$$

where Q is the activation energy governing atom attachment.

After fitting the discrete τ values at the four experimental temperatures, the continuous τ (T) could be obtained and plotted in **Fig. 34**. The activation energy Q obtained from the fitting from all four compositions are within the range expected for diffusion in MG. [176]

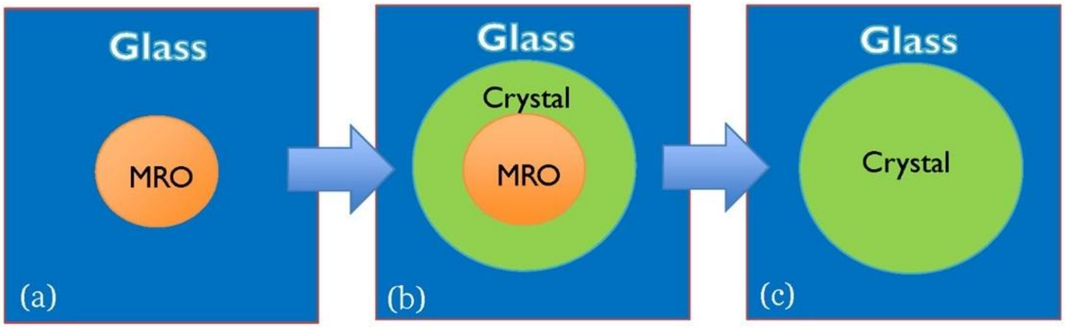

Fig. 32 (a) and (b) A schematic illustration of a nanocrystal nucleated on a disordered aluminum-like medium range order (MRO) region. The MRO/glass interface is replaced by the MRO/crystal interface. (c) The MRO rearranges and merges into the nanocrystal after nucleation.

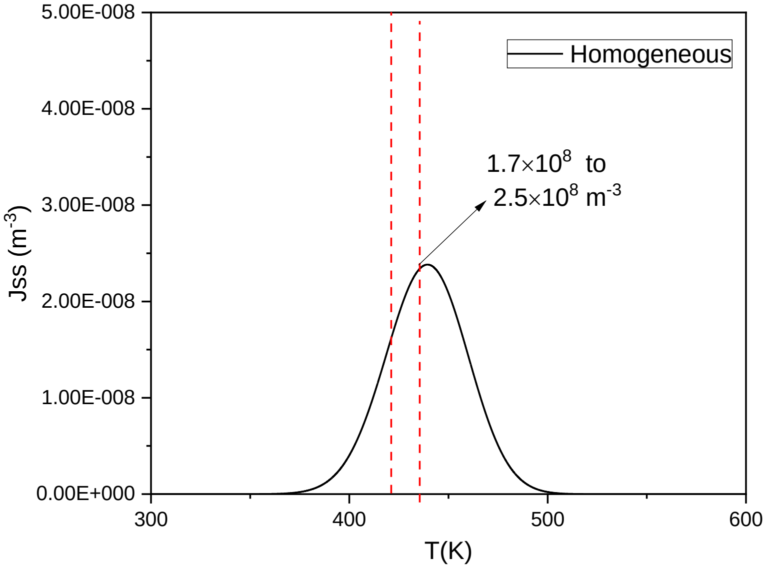

Fig. 33 J_{ss} vs T under homogeneous nucleation model. Red dash lines represent the temperature range in the experiment.

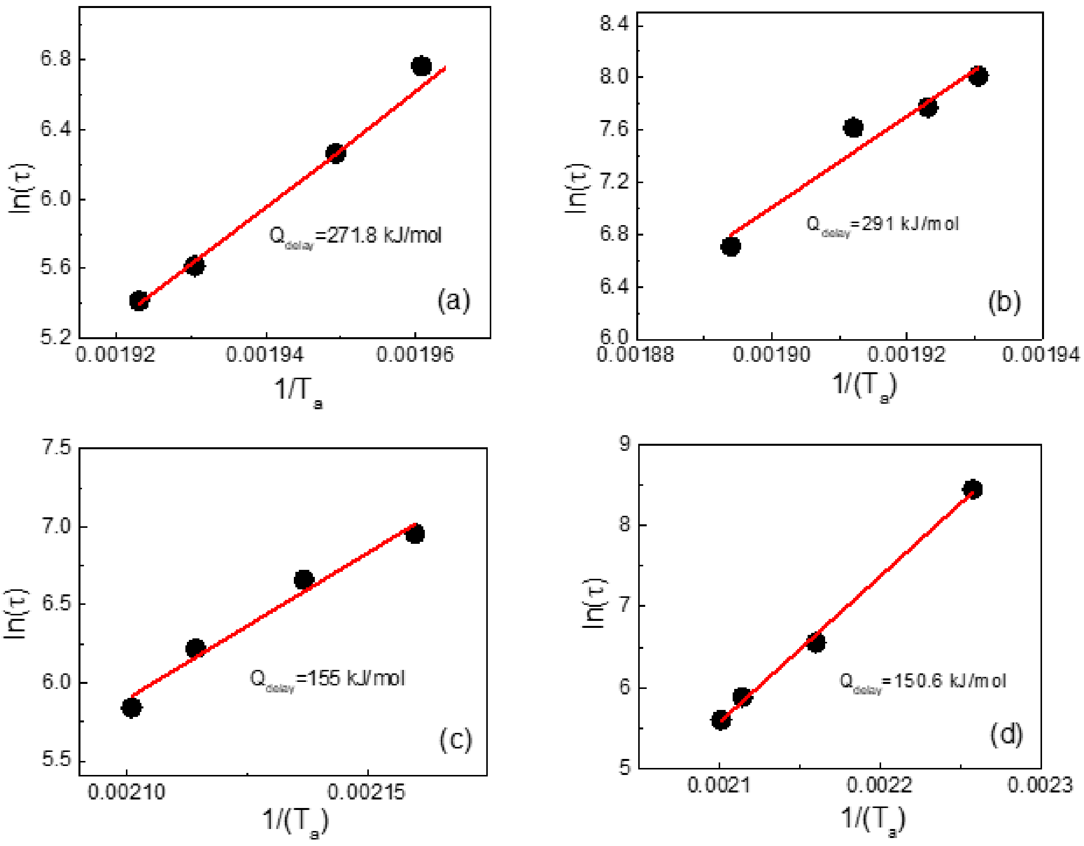

Fig. 34 Relationship between annealing temperature and delay time for four compositions (a) $Al_{88}Y_7Fe_5$, (b) $Al_{87}Y_7Fe_5Cu_1$, (c) $Al_{88}Y_6Fe_5Cu_1$ and (d) $Al_{88}Y_7Fe_4Cu_1$. The data points are the delay times measured directly from Flash DSC. The line is the delay time fitted by Arrhenius function. The activation energy Q are listed in the figure for each composition $Al_{88}Y_6Fe_5Cu_1$ and $Al_{88}Y_7Fe_4Cu_1$ have much lower Q compared to $Al_{88}Y_7Fe_5$ and $Al_{87}Y_7Fe_5Cu_1$

Table 5 Summary of thermodynamic and structural parameters used in the nucleation model.

Parameter	Symbol	Value
Volume energy (J/m^3)	ΔG_v	-8.76×108+1.0185×106T
MRO radius (m)	r_0	0.85×10^{-9} ($Al_{88}Y_7Fe_5$)
		0.9×10^{-9} ($Al_{87}Y_7Fe_5Cu_1$)
		0.82×10^{-9} ($Al_{88}Y_7Fe_4Cu_1$)
		0.82×10^{-9} ($Al_{88}Y_6Fe_5Cu_1$)
MRO-nanocrystal interface energy (J/m^2)	$\sigma_{MRO/crystal}$	0.00895
Glass-nanocrystal interface energy (J/m^2)	$\sigma_{glass/crystal}$	0.16+10-5T
Volume density of MRO (m^{-3})	ρ	5.2×10^{25} ($Al_{88}Y_7Fe_5$)
		2.2×10^{25} ($Al_{87}Y_7Fe_5Cu_1$),
		5.8×10^{25} ($Al_{88}Y_7Fe_4Cu_1$)
		5.2×10^{25} ($Al_{88}Y_6Fe_5Cu_1$),

Table 6 Summary of the delay times measured by Flash DSC, the delay time and the steady state nucleation rate measured by TEM for $Al_{88}Y_7Fe_5$

Temperature (°C)	τ from Flash DSC (s)	τ from TEM (s)	J_{ss} ($m^{-3}s^{-1}$)
237	965	1100 ± 150	3.01×10^{18}
240	525	640 ± 100	3.98×10^{18}
245	275	300 ± 70	5.41×10^{18}
247	225	180 ± 50	6.67×10^{18}

Table 7 Summary of the delay times measured by Flash DSC, the delay time and the steady state nucleation rate measured by TEM for $Al_{87}Y_7Fe_5Cu_1$

Temperature (°C)	τ from Flash DSC (s)	τ from TEM (s)	J_{ss} ($m^{-3}s^{-1}$)
245	3027	3376±411	1.85×10^{17}
247	2380	2361±376	2.51×10^{17}
250	2036	1651±394	3.79×10^{17}
255	820	967±215	5.15×10^{17}

Table 8 Summary of the delay time measured by Flash DSC, the delay time and the steady state nucleation rate measured by TEM for $Al_{88}Y_6Fe_5Cu_1$

Temperature (°C)	τ from Flash DSC (s)	τ from TEM (s)	J_{ss} ($m^{-3}s^{-1}$)
190	1312	1680±405	4.24×10^{18}
195	780	909±120	8.85×10^{18}
200	503	499±31	2.55×10^{19}
203	344	295±50	4.67×10^{19}

Table 9 Summary of the delay times measured by Flash DSC, the delay time and the steady state nucleation rate measured by TEM for $Al_{88}Y_7Fe_4Cu_1$

Temperature (°C)	τ from Flash DSC (s)	τ from TEM (s)	J_{ss} ($m^{-3}s^{-1}$)
170	4645	4119±475	2.68×10^{18}
190	703	706±49	4.28×10^{19}
200	359	325±31	8.01×10^{19}
203	270	264±15	11.14×10^{19}

IV.1.6 Nucleation Kinetics Calculation

In order to test the MRO catalyzed nucleation model, a comparison was made between the experimental and model predicted values of the steady state nucleation rate (J_{ss}). The number and type of sites suitable for nucleation existing within the liquid must be identified to calculate the steady state nucleation rate. After substituting the parameter values from **Table 5** into Eq. 10, the steady state nucleation rate is calculated as the curve in **Fig. 35**. The calculated J_{ss} has a peak shape because at low temperatures, the nucleation is diffusion limited whereas at high temperatures, the nucleation is driving force limited. All the experimental J_{ss} data, obtained by measuring the slope of the linear part of the N_v vs. t_{anneal} plot (**Fig. 30** and **Fig. 31**), lie on the lower temperature side of the peak because it is impossible to bypass the nose of the TTT (time-temperature-transformation) curve under the experimental heating rate in DSC (20 K/min). At the same time the high values for J_{ss} highlight the importance of the transient period to enable glass formation by rapid quenching. It is evident that extending the duration of the transient period is a key factor in promoting glass formation in bulk volumes.

An integration of the nucleation rate including the transient rate, J(t) yields the nanocrystal number density, Nv as given by

$$\mathrm{N}_{v} = \int_0^t J(t)V(t)dt = \int_0^t J_{SS}(T)exp\left(\frac{-\tau}{t}\right)V(t)dt \qquad \text{Eq.21}$$

where V(t) is the volume fraction available for nucleation of a new crystal. As nucleation and growth occurs, the volume of material available for new nucleation is reduced. Ultimately, there is a reduction in the number of MRO sites. V(t) can be expressed as:

$$V(t) = 1 - \frac{V_T(t)}{V_{tangent}} \qquad \text{Eq.22}$$

$$V_T(t) = \sum \frac{4}{3} \pi r_i^3 \qquad \text{Eq.23}$$

where $V_T(t)$ represents the transformed volume fraction, $V_{tangent}$ is maximum volume fraction of FCC-Al which can be obtained from the tangent line (calculated by the lever rule through the red line in **Fig. 36(a)**) and r_i stands for the radius of each nanocrystal.

In order to understand the transition volume at different annealing time ($V_T(t)$), a rejection layer around Al nanocrystal needs to be considered. Take $Al_{88}Y_7Fe_5$ as an example, **Fig. 36(b)** shows the shell enriched with Y and Fe around an Al nanocrystal. This region has a changed composition so that it is not available for further nucleation. Allen et al. [169] indicate that the rare earth element diffuses much slower than the transition metal. In Al-Y-Fe MGs, Y is the slower diffuser. Thus, the composition of the outer shell can be estimated by the interface contour [169] (IC) in **Fig. 36(a)**. In a ternary system A, B, C where B and C are solutes in A the tie line gives the interface composition of the matrix and precipitate only when $D_B = D_C$. If $D_B \neq D_C$ the interface compositions deviate from the tie line values. For differing component diffusivities, the interface contour which includes all bulk alloy compositions in a two-phase field that yield a given set of precipitate and matrix compositions at the interface is useful in analyzing growth. For the current analysis the ratio $D_{Fe}/D_Y \approx 100$ has been used which is reasonable for the large observed differences in the composition profiles of the rare earth and transition metal[169]. The application of the IC through Al-7Y-5Fe yields the matrix composition of Al-12.4Y-5.1Fe and the precipitate composition Al-0.01Y-0.4Fe as shown in **Fig. 36(a)**.

For this composition, the outer shell volume can be calculated as 1.1 times the Al nanocrystal volume. Then, the total transformed volume is about 2.1 times the Al nanocrystal volume. With parameter evaluations mentioned above, the fitting curve for the transformed volume fraction changes for $Al_{88}Y_7Fe_5$ during annealing at 245°C is presented in **Fig.37(a)**. Substituting the J_{SS} and $V_T(t)$ values into Eq. 21, the resulting simulation curve is shown in **Fig.37(b)**. The simulation curve agrees well with the experimental plot.

By applying the same method, the calculated N_v values are plotted as the smooth curves in both **Fig. 30** and **Fig. 31**, which also show a good agreement with the experimental N_v data points. In addition, the multiplication of Eq. 19 and Eq.21 yields

$$ln(J_{SS}\tau) = ln(\frac{\rho}{2Z}) - (\frac{\Delta G^*}{kT}) \qquad \text{Eq.24}$$

The value of Z as 0.01 is used to calculate the intercept ln(ρ/2Z). From Eq.24, there is a linear relationship between $\ln(J_{ss}\tau)$ and $(\Delta G^*)/kT$. The calculated results of the $\ln(J_{ss}\tau)$ vs. $(\Delta G^*)/kT$ from experiment is shown in **Fig. 38**. The fitting curve of all 4 compositions exhibit linear relationships. For example, in $Al_{87}Y_7Fe_5Cu_1$, the intercept from the experiment is 60.67±2.21 and the slope is -0.91±0.36. This result is reasonable compared to the theoretical calculated values which are 58.93 and -1. Besides, for $Al_{88}Y_7Fe_4Cu_1$, the intercept from the experiment is 64.16±1.26 and the slope is -1.09±0.18. The theoretical calculated values are 62.87 and -1 respectively. Therefore, the experiment result of $Al_{88}Y_7Fe_4Cu_1$ is also in a reasonable range. The good fit also confirms the established nucleation model and indicates that a common mechanism is operating over the experimental range.

Besides, the model was also satisfied with other constraints: (1) The surface energy between crystal and glass is larger than a half of grain boundary energy of Al. (2) Critical nucleus radius r* is bigger than the MRO radius. (3) $\Delta G^*/kT$ of each composition is between 12 and 60. (4) ΔG_v equals zero at the liquidus. (5) The delay time activation energy is within the reasonable range.

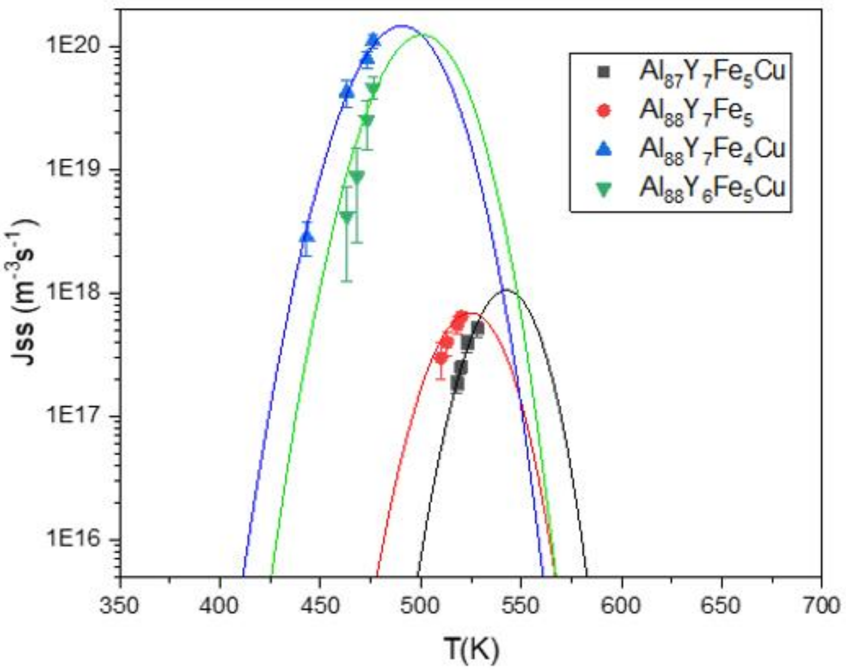

Fig. 35 The calculated steady state nucleation rate (continuous curve) plotted together with the experimental J_{ss} (data points) for $Al_{88}Y_7Fe_5$, $Al_{87}Y_7Fe_5Cu_1$, $Al_{88}Y_6Fe_5Cu_1$ and $Al_{88}Y_7Fe_4Cu_1$

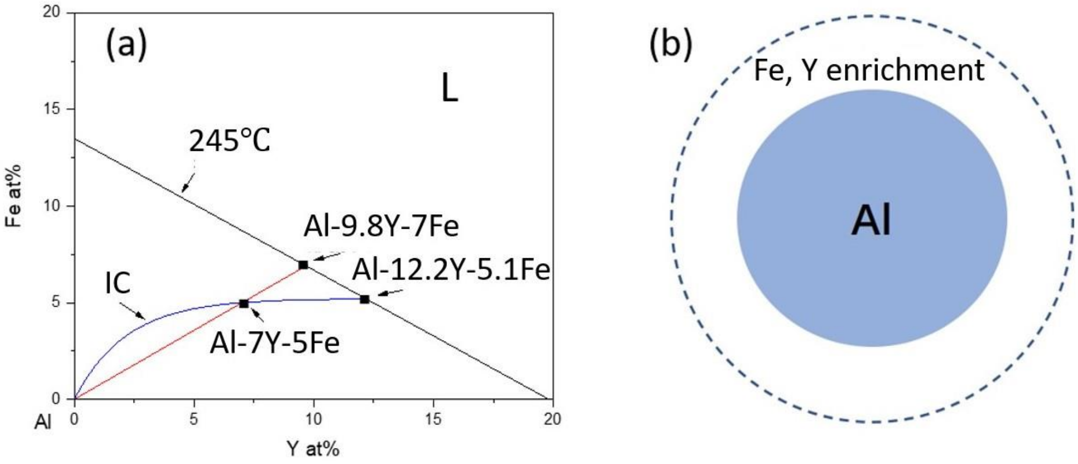

Fig. 36 (a) Al-Y-Fe ternary phase diagram. The red line represents the tangent line which shows the composition of liquidus at equilibrium which is Al-9.8Y-7Fe. The blue curve is the interface contour which shows the composition of liquidus at interface which is Al-12.2Y-5.1Fe. (b) Schematic showing the transformation affected region in the matrix

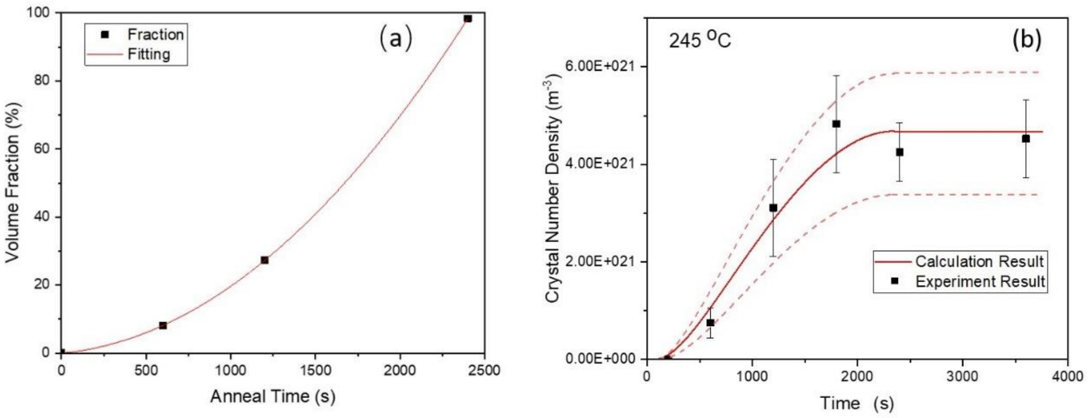

Fig. 37 (a) Transformed Volume Fraction for $Al_{88}Y_7Fe_5$ annealing at 245 ^{o}C (b) Simulation result for $Al_{88}Y_7Fe_5$ annealing at 245 ^{o}C where the solid curve is the calculation result and dashed curves represent the uncertainty of the calculation.

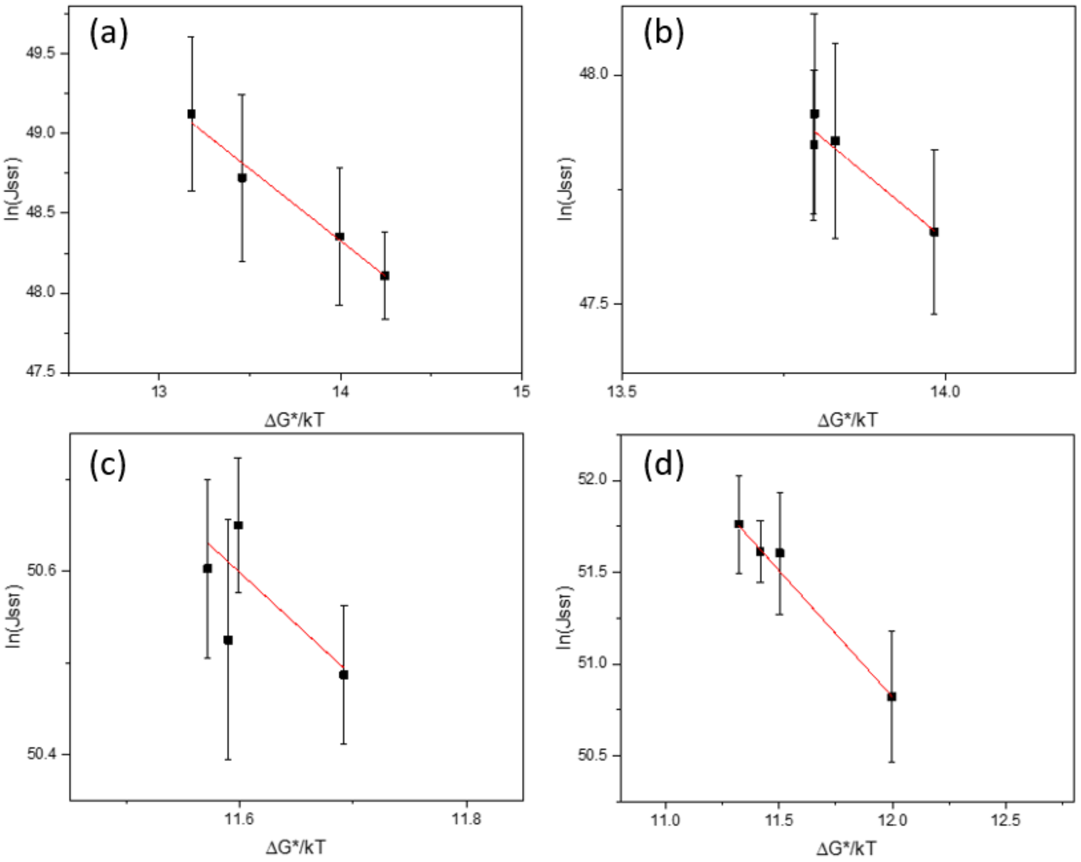

Fig. 38 The correlation between calculated ln($J_{ss}\tau$) vs ($\Delta G^*/kT$) for (a) $Al_{88}Y_7Fe_5$, (b) $Al_{87}Y_7Fe_5Cu_1$, (c) $Al_{88}Y_6Fe_5Cu_1$ and (d) $Al_{88}Y_7Fe_4Cu_1$.

IV.1.7 Summary

Primary crystallization of amorphous alloys is an important pathway to the synthesis of nanoscale microstructures. Previous studies have indicated that amorphous Al alloys contain spatial heterogeneities composed of Al-rich regions exhibiting MRO. The heterogeneities can act as a catalyst to promote a high density of Al nanocrystals. From the quantitative structural analysis, a nucleation model has been developed for the MRO catalysis of Al nanocrystals that is based upon Al nucleating around the MRO core to lower the nucleation barrier. With the MRO seeded nucleation model and the kinetic data from the delay time (τ) measurement, the evolution of the measured Al nanocrystal density (N_v) can be accounted for during the primary crystallization through the isothermal annealing treatments. Also, the predicted values of steady state nucleation rates (J_{ss}) are consistent with the experimental results. In addition, MRO seeded nucleation model has satisfied the constraints set by the thermodynamic, kinetic and structural parameters. The model reflects a generic scheme for the treatment of MRO mediated nucleation reactions which may be applied more broadly to nucleation in materials characterized by the presence of spatial heterogeneities.

From separate measurements of the nucleation delay time the origin of the large effect of the Cu substitution has been linked mainly to the changes in the delay time. In fact, from **Fig. 35**, the J_{ss} of $Al_{88}Y_7Fe_4Cu_1$ is almost 100 times of $Al_{87}Y_7Fe_5Cu_1$. Compared to the change of MRO density (2 times), delay time change should be considered as the main factor in controlling the nucleation. Since the delay time is directly related to the atom attachment to an evolving nucleus, the Cu substitution is impacting the ability of Al atoms to attach to the nucleus. The mechanism underlying the changes in attachment frequency requires further study, but there is some insight from an MD study of Al-Sm alloys. The MD simulations indicated that the mobile Al atoms are constrained by the icosahedral like clusters in the glass and move as groupings. With increasing Sm content, the population of the icosahedral like clusters grows to further restrict the Al mobility that in turn inhibits crystal nucleation and promotes glass formation [62]. It is reasonable to expect that the Cu substitution in Al-Y-Fe alloys can have a similar effect on the Al attachment frequency, but further experimental study and analysis are necessary.

IV.2 Nanocrystal Evolution during Ultra-Fast Heating in an Fe-B Amorphous Alloy

IV.2.1 Thermal Analysis

To investigate how the rate of heating affects the crystallization behavior, both DSC and Flash DSC have been applied. Samples (4-5 mg of mass) encapsulated in Al pans were used for DSC. Flash DSC samples (0.15-0.25 µg of estimated mass) were prepared by cutting ribbons into small pieces and transferred using a hair onto the center of a UFH-1 sensor.

DSC traces for the $Fe_{85}B_{15}$ MG are displayed in **Fig. 39(a)**. Two crystallization exothermic peaks are evident with the crystallization onset temperatures ($T_x^{BCC\text{-}Fe}$, T_x^{Fe3B}) marked by arrows. An endothermic signal related to the glass transition was not detected in the conventional DSC test. The results are given in **Fig. 39(b)** for the as-spun $Fe_{85}B_{15}$ MG and the heat-treated $Fe_{85}B_{15}$ MGs heated at the rate of 0.67 K/s up to the 1st (708 K) and the 2nd (750 K) crystallization peak temperature followed by the immediate cooling at the maximum cooling rate of DSC (8.3 K/s) to the room temperature. It was determined that the 1st and 2nd crystallization peaks of $Fe_{85}B_{15}$ MG are related to the precipitation of the stable BCC-Fe and the metastable Fe_3B phase, respectively.

Before analyzing Flash-DSC measurements, there are several calibrations needs to be considered. One important consideration when using Flash DSC is the thermal lag between the sample's temperature and the programmed furnace temperature. This lag can cause a significant deviation in the measured onset temperature in Flash DSC curves from their actual values.[177] The extent of this thermal lag increases with both temperature and heating rate. To ensure accurate temperature calibration, it is crucial to directly determine the thermal lag for the specific sample under investigation.[178]

However, in contrast to metallic glasses like those based on gold [179] or zirconium[178], which can be repeatedly melted and vitrified using Flash DSC, it is not feasible to examine the effects of heating rate on the T_m or melting enthalpy of binary $Fe_{85}B_{15}$ metallic glass due to its exceptionally high melting temperature (> 1000 °C). Therefore, considering the temperature range relevant to the crystallization temperature of $Fe_{85}B_{15}$ metallic glass, we used standard samples of aluminum (Al, T_m = 660.3 °C) and zinc (Zn, T_m = 419.5 °C) for temperature calibration.[180–182]

Fig. 40(a) displays the measured melting temperature of Al and Zn as a function of heating rate (φ). To minimize the thermal resistance between the sample and sensor, small pieces of Al (0.07 μg) and Zn (0.08 μg) were applied as shown in **Fig. 40(b)**. The non-linear dependence of the onset temperature on heating rate can be described as $T_m^{cor} = T_m^{mea} + a \cdot \varphi - b \cdot \varphi^{0.5}$.[183] By fitting the measured T_m^{mea}in **Fig. 40(a)** with this empirical correlation, the heating rate dependence of $T_m^{mea}$was obtained as below:

Zn: $T_m^{cor} = T_m^{mea} + 8.0 \cdot 10^{-6} \cdot \varphi - 0.004 \cdot \varphi^{0.5}$ Eq.25

Al: $T_m^{cor} = T_m^{mea} + 8.0 \cdot 10^{-6} \cdot \varphi - 0.004 \cdot \varphi^{0.5}$ Eq.26

Measured Flash DSC curves were adjusted with the sample temperature correction function in STARe software (Mettler Toledo) by comparing standard and measured T_m of Al and Zn. To correct the heating rate dependence of the measured temperature, sample temperature calibration was performed using the values of the standard T_m and T_m^{cor} as a function of φ, as described in Eq.25 and Eq.26.

To obtain the accurate thermal analysis results, the effect of sample mass on the onset temperature is another consideration. Typically, the mass of Flash DSC samples has been determined by comparing the melting enthalpy with the value measured on samples with a known mass. However, due to their high $\boldsymbol{T_m}$ and low glass forming ability, the melting enthalpy of the $Fe_{85}B_{15}$ MG cannot be estimated with the Flash DSC. Thus, Flash DSC sample mass of $Fe_{85}B_{15}$ was estimated by comparing the normalized crystallization enthalpy ($\Delta \boldsymbol{H_x}$) and volume estimated by optical microscope (OM) images. **Fig. 41(a)** shows the DSC and Flash DSC curves obtained at the 5 K/s. The DSC trace was conducted with 4.4 mg of a $Fe_{85}B_{15}$ sample encapsulated in Al pans. The measured $\Delta \boldsymbol{H_x}$ is 183 J/g. The measured crystallization enthalpy ($\boldsymbol{H_x^{Flash}}$) of the Flash DSC sample, which is the area of the crystallization peaks is measured as $25.6 \cdot 10^{-3}$ mJ. From the simple correlation ($\boldsymbol{H_x^{Flash}/mass_{Flash} = H_x^{DSC}/mass_{DSC} = \Delta H_x \ = 183\, J/g}$), the mass of Flash DSC sample was estimated as 0.14 μg. **Fig. 41(b)** is the optical microscope image of the $Fe_{85}B_{15}$ sample used for Flash DSC test. By assuming that sample is a rectangle with thickness of 30 μm, and the density of $Fe_{85}B_{15}$ is 7.02 g/cm^3, the sample mass is estimated as 0.176 μg. From the similar mass between estimated from the $\Delta \boldsymbol{H_x}$ comparison (0.150 μg, **Fig. 41(a)**) and OM image (0.176 μg, **Fig. 41(b)**), the heat flow of the Flash DSC curves obtained at the heating rates from 10 K/s to 5000 K/s were normalized with the sample mass estimated from OM images.

Through the careful temperature and enthalpy calibration, corrected Flash DSC traces were successfully obtained at the heating rates from 5 K/s to 5000 K/s in **Fig. 42(a)**. **Fig. 42(b)** represents the magnified curves with the endothermic heat flow related to the glass transition. It is evident that endothermic glass transition signals are observed in the Flash DSC curves from the heating rate of 500 K/s.

From **Fig 42(a)**, as the heating rate increases, Tx increases, and the crystallization reaction peaks become sharper with a larger amplitude. From a heating rate of 500 K/s the T_g signal starts to become detectable. Unlike the DSC curves showing two crystallization peaks, the Flash DSC results show an additional third peak, related to the transition of metastable Fe_3B compound into stable Fe_2B compound and BCC-Fe.[184] By summarizing the DSC and Flash DSC results, Kissinger plot of Tx and crystallization peak temperature (T_p) that can reflect the crystallization activation energy and growth kinetics was obtained as shown in **Fig 42(c)**.

After applying the mass calculation, a continuous heating transformation (CHT) curve could be plotted as **Fig. 43**. The average values and the standard deviation of onset temperatures obtained from repeated Flash DSC tests were used to construct the CHT curve. The CHT curve in **Fig. 43** demonstrates that the crystallization area of primary BCC-Fe in $Fe_{85}B_{15}$ is relatively narrow. Thus, the maximum heating temperature and cooling rate of the fast-heating process should be controlled to prevent the deterioration of the magnetic properties of $Fe_{85}B_{15}$ MG composite due to the formation of the Fe_3B hard magnet phase that can degrade the soft magnetic property of Fe-based MG nanocomposites.[185]

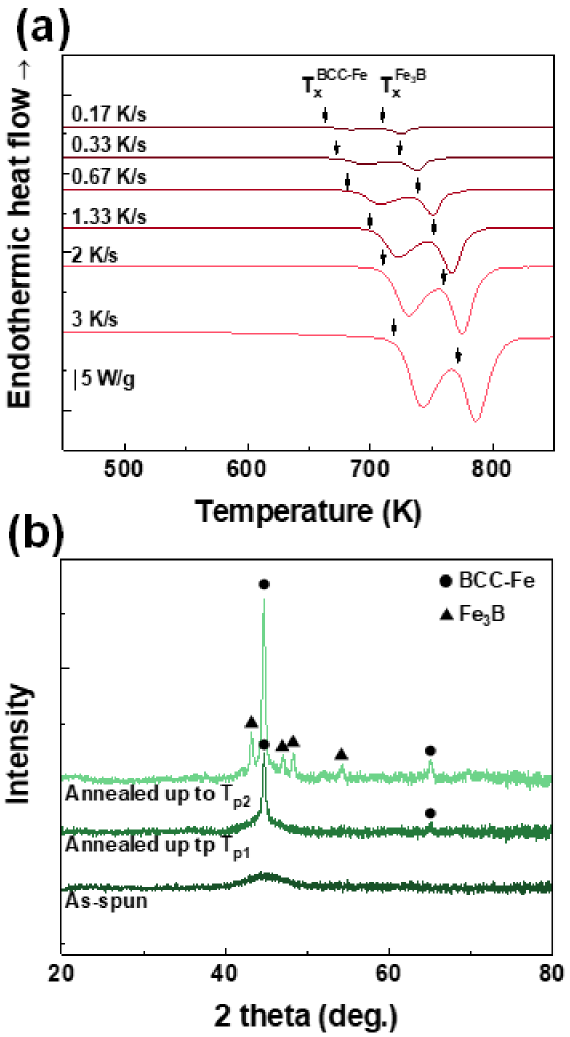

Fig. 39 (a) DSC traces of $Fe_{85}B_{15}$ MG obtained at various heating rates. (b) XRD results of as-spun $Fe_{85}B_{15}$ MG and $Fe_{85}B_{15}$ MG composite annealed at 0.67 K/s up to 1st and 2nd peak temperature

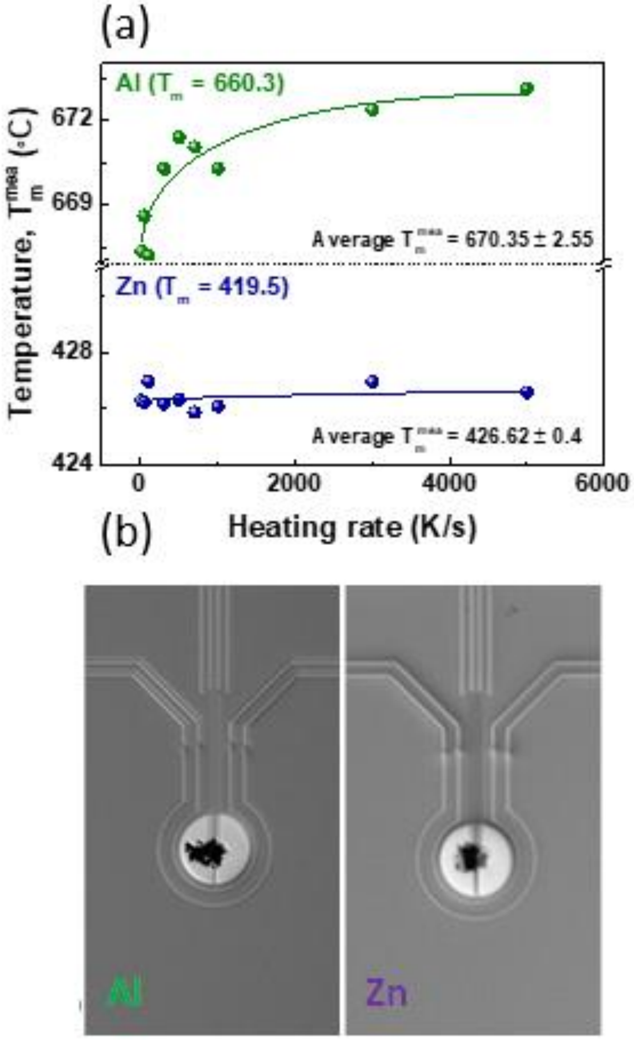

Fig. 40 (a) Measured melting temperature ($\boldsymbol{T_m^{mea}}$) of Al and Zn as a function of the heating rate. (b) Optical microscope image of Al and Zn on the UFH-1 sensor.

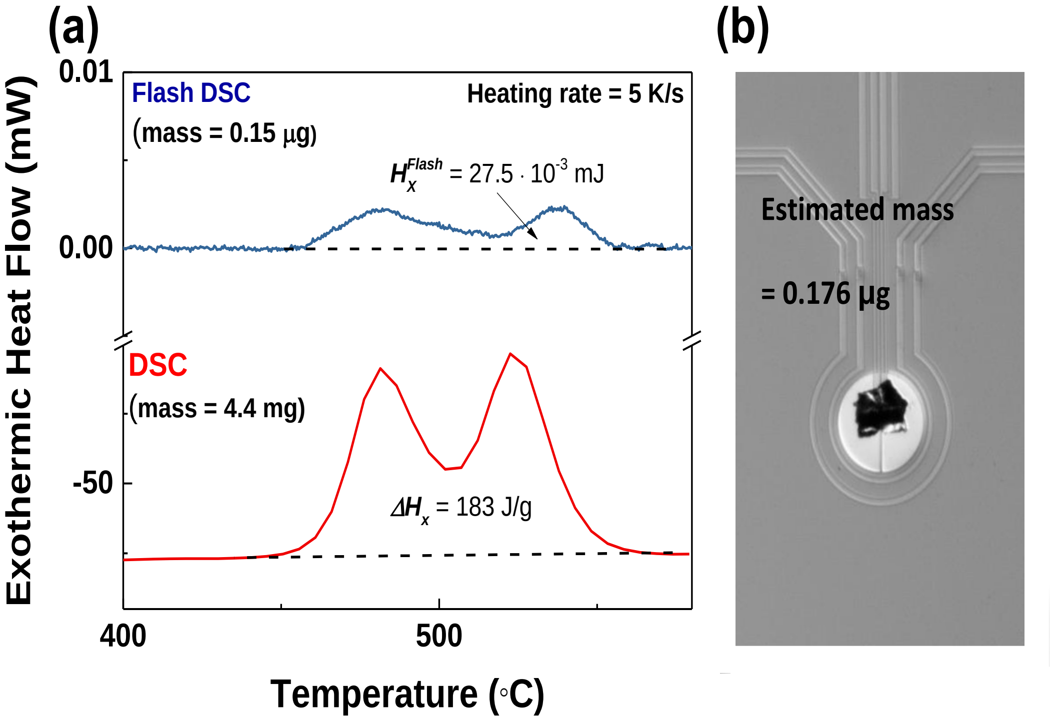

Fig 41 (a) DSC and Flash DSC curves of $Fe_{85}B_{15}$ MG obtained at the heating rate of 5 K/s. (b) Optical microscope image of Al and Zn on the UFH-1 sensor.

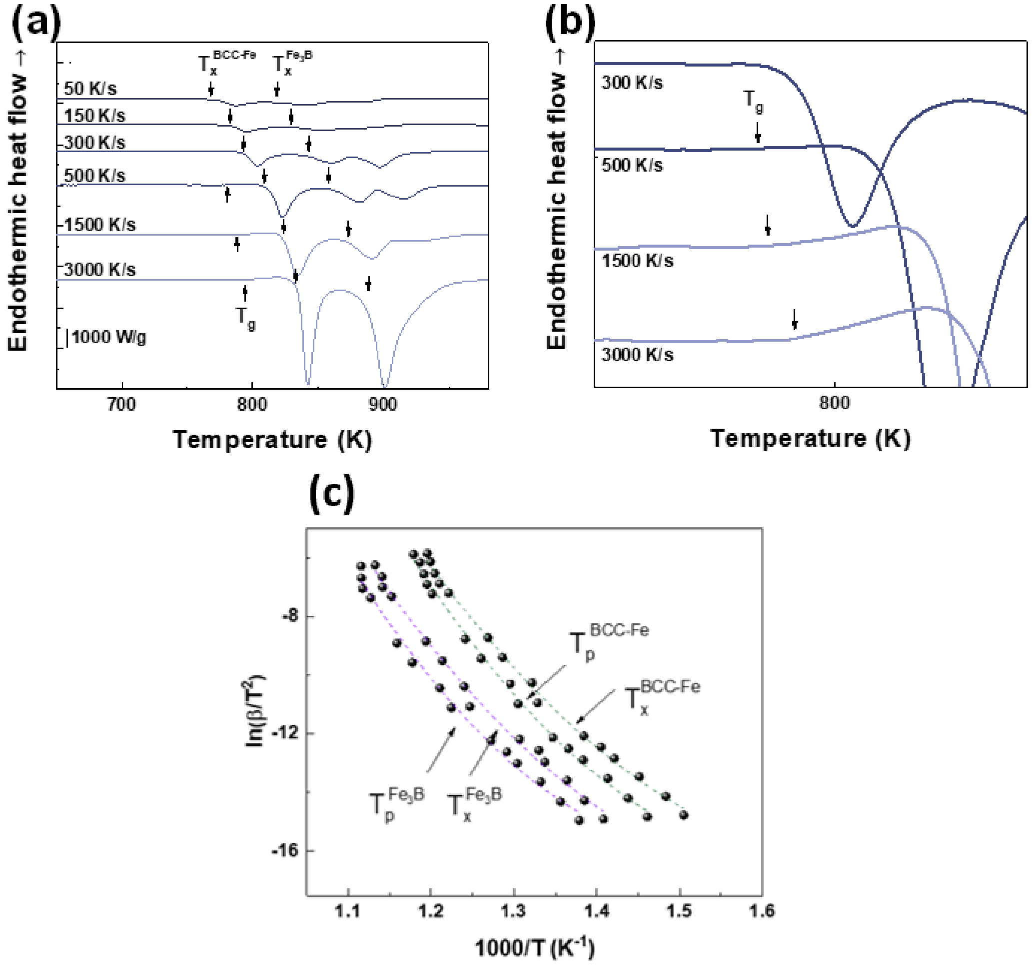

Fig. 42 (a) Representative Flash-DSC results (b) Magnified curves showing glass transition signal (c) Kissinger plot of Crystallization onset temperature and peak temperature of BCC-Fe and Fe_3B crystalline phases.

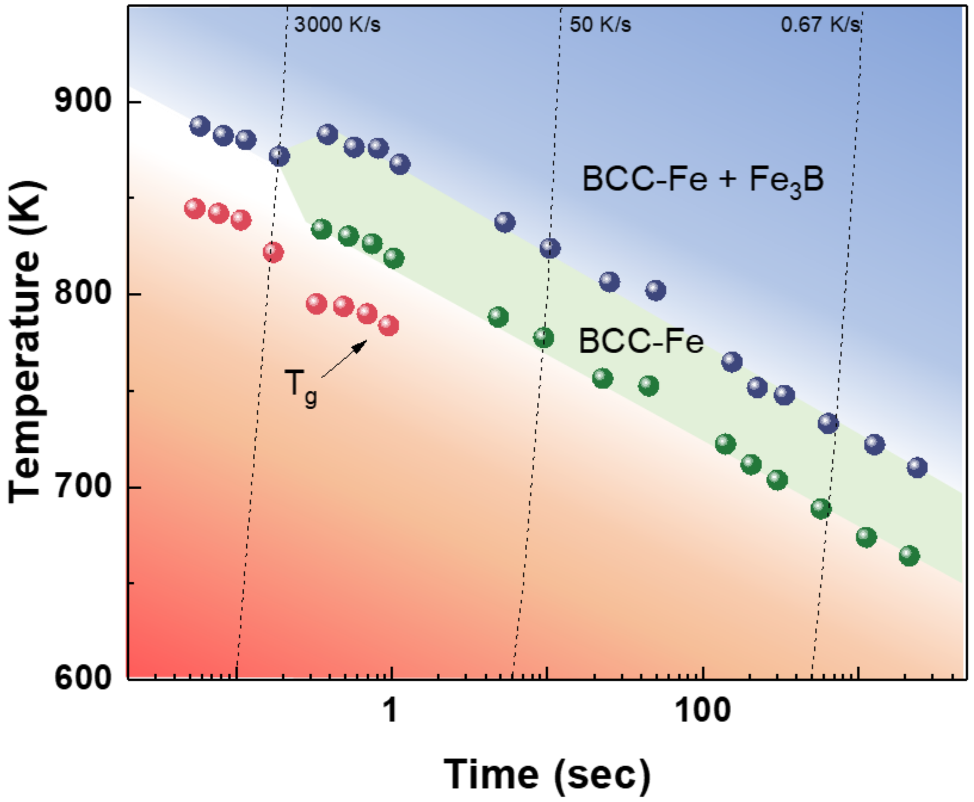

Fig. 43 Continuous Heating Transformation curve transposed from DSC and Flash DSC results.

IV.2.2 Microstructure Analysis

TEM images of the samples after heating at rates of 0.67 K/s (by DSC), 50 K/s, 500 K/ and 3000 K/s (by Flash DSC) up to their first crystallization peak temperature (T_p, T_p (0.67K/s) = 709 K, T_p (50K/s) = 791 K, T_p (500K/s) = 829 K, and T_p (3000K/s) = 893 K) are shown in **Fig. 44**. The samples were heated by DSC at the constant heating rate of 0.67 K/s up to first T_p and cooled to room temperature immediately at the cooling rate of 8.3 K/s, which is the maximum cooling rate of DSC. The Flash DSC was used to heat the samples at the fast-heating rate of 50 K/s, 500 K/s, and 3000 K/s. To suppress the additional growth of BCC-Fe, samples heated by Flash DSC were cooled to room temperature at the cooling rate of 40000 K/s after the short holding sequence of 0.1s. BCC-Fe nanocrystals are evident in the TEM images and the inserted SAED patterns of the MG after the heating up to T_p.

From the TEM images, size distributions of the precipitated BCC-Fe were obtained as shown in **Fig. 45**. For the accuracy of the data, diameters of BCC-Fe were measured and collected from many bright and dark-field images with different magnifications. As clearly shown in **Fig. 46**, average diameters of BCC-Fe and width of the size distributions are decreasing with the increased heating rate. From the size distribution data, correlation of heating rate and size/number density of BCC-Fe is obtained as shown in **Fig. 46**. Similar with the previous reports on the fast-heating process of binary $Fe_{87}B_{13}$ and $Fe_{86}B_{14}$ amorphous alloys induced by the Cu block rapid heater, the average diameter decreases rapidly from 50 nm (0.67 K/s) to 17 nm (50 K/s) with a minimum dimeter of about 15 nm (500 K/s).

However, it should be mentioned that the additional growth of BCC-Fe might occur during the cooling of the sample heated at 0.67 K/s, because of the limited cooling rate ($\leqslant$ -0.83 K/s) of conventional DSC used in this study. In addition, the number density of BCC-Fe nanocrystals increased with the heating rate from 0.09×10^{22} m^{-3} (0.67 K/s) to 1.6×10^{22} m^{-3} (500 K/s). However, even with the fast-heating rates spanning to 3000 K/s, measured average diameter was as similar as 500 K/s.

In order to interpret the limited size reduction shown in **Fig. 47**, the growth kinetics of primary BCC-Fe were examined, including the isothermal annealing test and compositional profile analysis. The representative TEM images of the $Fe_{85}B_{15}$ MG annealed at 663 K for various annealing times are shown in **Fig. 47**. By using DSC, ribbon samples were annealed at 663 K for different times and immediately cooled to room temperature. The bright field TEM image of $Fe_{85}B_{15}$ MG annealed at 663 K for 100s shows the monolithic amorphous matrix. With continued exposure BCC-Fe nanocrystals embedded in the matrix nucleate and grow with annealing time. The measured number density (Black solid points) and average radius (Blue opened points) of BCC-Fe with annealing time are summarized in **Fig. 48**.

After the transient nucleation stage (τ = 175s) at 663 K, the number density of BCC-Fe nanocrystals increased with a steady state nucleation rate, $J_{SS} = 2.23 \cdot 10^{18}\ \mathrm{m^{-3}s^{-1}}$. The saturated number density observed in the growth stage is $8.2 \cdot 10^{20}\ \mathrm{m^{-3}}$. During growth, the average radius of the BCC-Fe nanocrystals initially increased parabolically and saturated at about 38 nm. When the diffusion coefficient is independent of concentration, growth of the average radius of BCC-Fe (R) can be fitted by [185]:

$$\boldsymbol{R} = \boldsymbol{S} \cdot \sqrt{\boldsymbol{D} \cdot \boldsymbol{t}} \qquad \text{Eq.27}$$

Here, S $(= \frac{C_m - \bar{C}(t)}{C_p - C_m} = 1.3$, $\bar{C}$ is the average solute content in the matrix. and C_p, C_m are the crystal and matrix compositions at the interface, respectively.) is the parabolic growth constant that depends on the concentrations at the nanocrystal glass interface. D is diffusion coefficient of B in the Fe-B amorphous matrix, which was reported as $D = 2.0 \cdot 10^{-4} \cdot \exp{(-1.8 \cdot 10^5/RT)}$ [186]. The initial increase in the average radius with the annealing time (t) was fitted with Eq.27 (Blue dashed line). However, at the later stage of growth, there is a large difference between the fitted value and the measured average radius. The deviation from parabolic growth behavior observed in the isothermal test highlights the need to consider the influence of the diffusion-field impingement on the growth kinetics involving the high number density and fast heating rate.

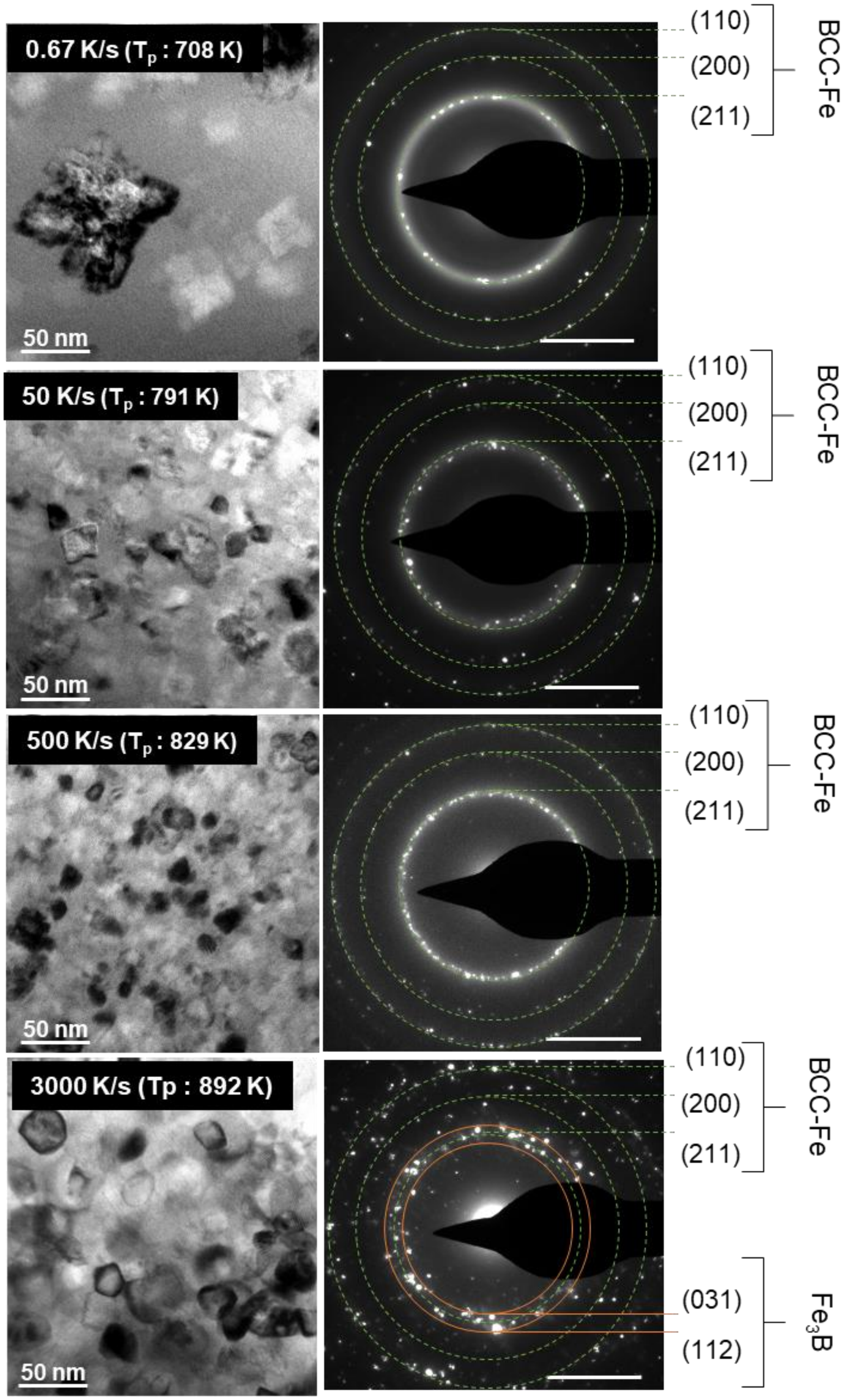

Fig. 44 TEM images and SAED patterns of annealed $Fe_{85}B_{15}$ alloys with the heating rate of 0.67 K/s, 50 K/s, 500 K/s, and 3000 K/s up to their $T_p^{BCC\text{-}Fe}$.

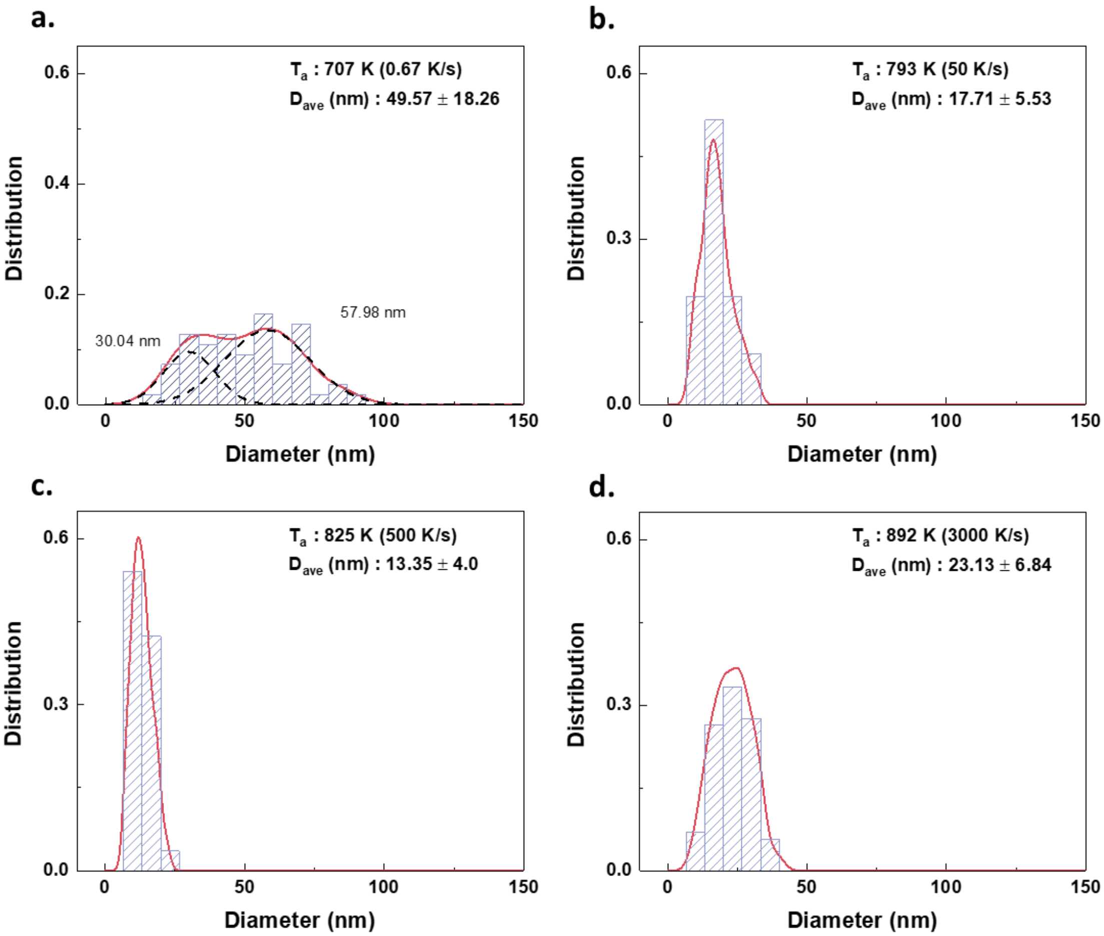

Fig. 45 Size distribution of the precipitated nanocrystals in annealed $Fe_{85}B_{15}$ alloys heated at the heating rate of 0.67 K/s, 50 K/s, 500 K/s, and 3000 K/s up to their $T_p^{BCC\text{-}Fe}$. Red solid lines are the kernel density estimation.

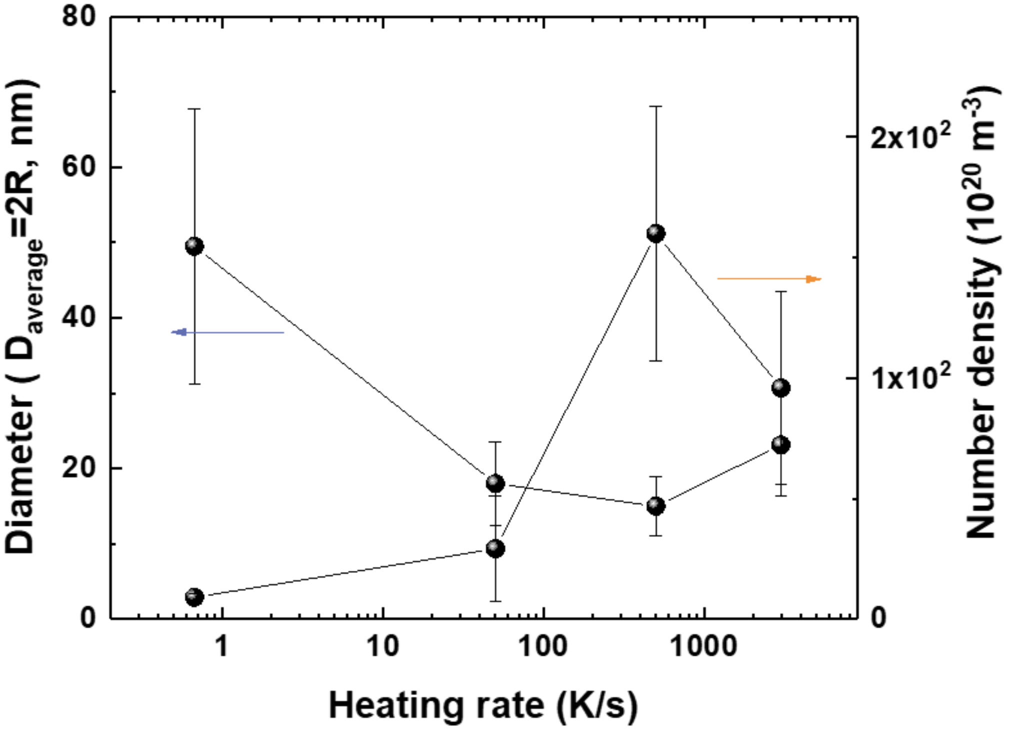

Fig. 46 Average diameter and number density changes of BCC-Fe in annealed $Fe_{85}B_{15}$ as a function of heating rate (K/s).

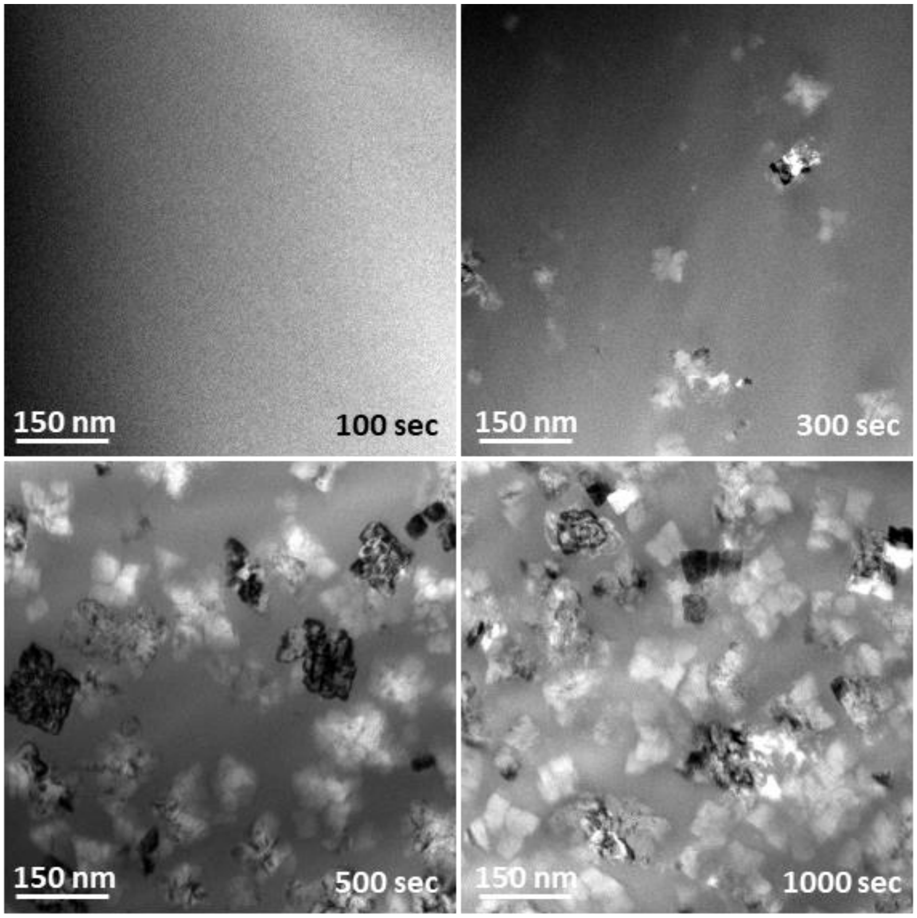

Fig. 47 Bright-field TEM images of $Fe_{85}B_{15}$ MG annealed at 633 K (= $T_x^{0.67\ K/s}$ - 50 K) for annealing time of 100s, 300s, 500s, and 1000s.

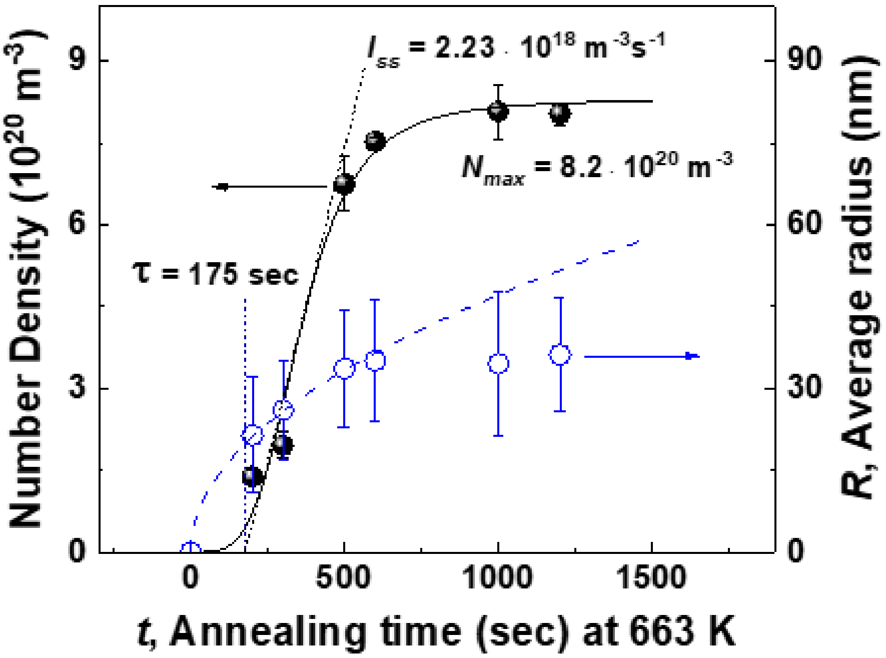

Fig. 48 Number density (Black solid points) and average radius (Blue open points) of BCC-Fe changing as a function of annealing time.

IV.2.3 Impingement in Fe-B MG

To interpret the influence of the impingement on the growth kinetics of BCC-Fe nanocrystals in $Fe_{85}B_{15}$ MG during fast heating, the diffusion-field between two adjacent nanocrystals was calculated at different heating rates. Growth of BCC-Fe nanocrystals redistributes the B solute atoms around the nanocrystals and results in the solute enriched area [187]. It has been suggested that growth of nanocrystals is inhibited by the impingement of the diffusion field[169]. The concentration of B in the matrix ahead of the interface of BCC-Fe during the isothermal annealing is given as [169,188] :

$$c = c_0 + 0.5\left(c_m - c_p\right) \cdot S^3 \exp\left(\frac{S^2}{4}\right) \cdot [s^{-1} \exp\left(-\frac{s^2}{4}\right) - \frac{\sqrt{\pi}}{2}(1 - \mathrm{erf}\,(\frac{S}{2}))] \qquad \text{Eq.28}$$

Here, $s = \frac{r}{\sqrt{D \cdot t}}$, and r is the radius of diffusion field. C_0 (= 0.15) is the initial composition of B in the matrix, C_p (= $8 \cdot 10^{-7}$), and C_m (= 0.29) are the B solute content in the precipitate and the matrix compositions at the interface, respectively [189]. S (= 1.3) is the parabolic growth constant which has the same physical meaning with S in Eq. 27. The measured volume fractions of BCC-Fe in TEM images of $Fe_{85}B_{15}$ MG heated at different rates to T_p (**Fig. 44**) are similar ($V_f^{Tp} = 0.143 \pm 0.006$). Thus, the isothermal annealing time (t) to reach V_f^{Tp} after the continuous heating at the rate of φ can be obtained from the slope of the tangential lines in **Fig. 49(a)** based on additive reaction ($t\left(V_f^{Tp}, T_p\right) = \left|\frac{\delta T_p}{\delta \varphi}\right|_{V_f^{Tp}}$) [190].

The transformation times associated with the non-isothermal annealing at the heating rates of 0.67 K/s (T_p = 709 K), 50 K/s (T_p = 785 K), and 500 K/s (T_p = 823 K) are 30s, 0.33s, and 0.04s. respectively. The expected spacing between nanocrystals (R_{space}), which corresponds to the number density of $0.08 \times 10^{22}\ \mathrm{m}^{-3}$ (0.67 K/s), $0.29 \times 10^{22}\ \mathrm{m}^{-3}$ (50 K/s), and $1.6 \times 10^{22}\ \mathrm{m}^{-3}$ (500 K/s) are 108 nm, 70 nm, and 40 nm, respectively. The calculated compositional profiles after the isothermal annealing at 709 K for 30s and 791 K for 0.33s are shown in **Figs. 49(b)** and **(c)** corresponding to the continuous heating at 0.67 K/s and 50 K/s, respectively. A faster heating process (50 K/s) resulted in separated solute rich areas between two nanocrystals (**Fig. 49(c)**). However, a further increase of heating rate (500 K/s) reduced the R_{space} to 40 nm and generated the diffusion-field impingement again (**Fig. 49(d)**). Hence, the enriched B concentration in the matrix inhibits the additional nucleation and size reduction of BCC-Fe as indicated in the microstructures in TEM images of **Fig. 43**.

Moreover, As described in **Fig. 49(b)**, the deviation from parabolic growth behavior occurs from the annealing time of 600s. It is expected that this difference is induced by the diffusion field impingement on the growth kinetics involving the high number density of BCC- nanocrystals. To explain this idea, compositional profile around BCC-Fe after the isothermal annealing at 663 K for 300s and 600s were calculated as shown in **Fig. 50**. Unlike the 300s which resulted in the separated solute rich areas between two nanocrystals, large diffusion field impingement is generated after the annealing for 600s.

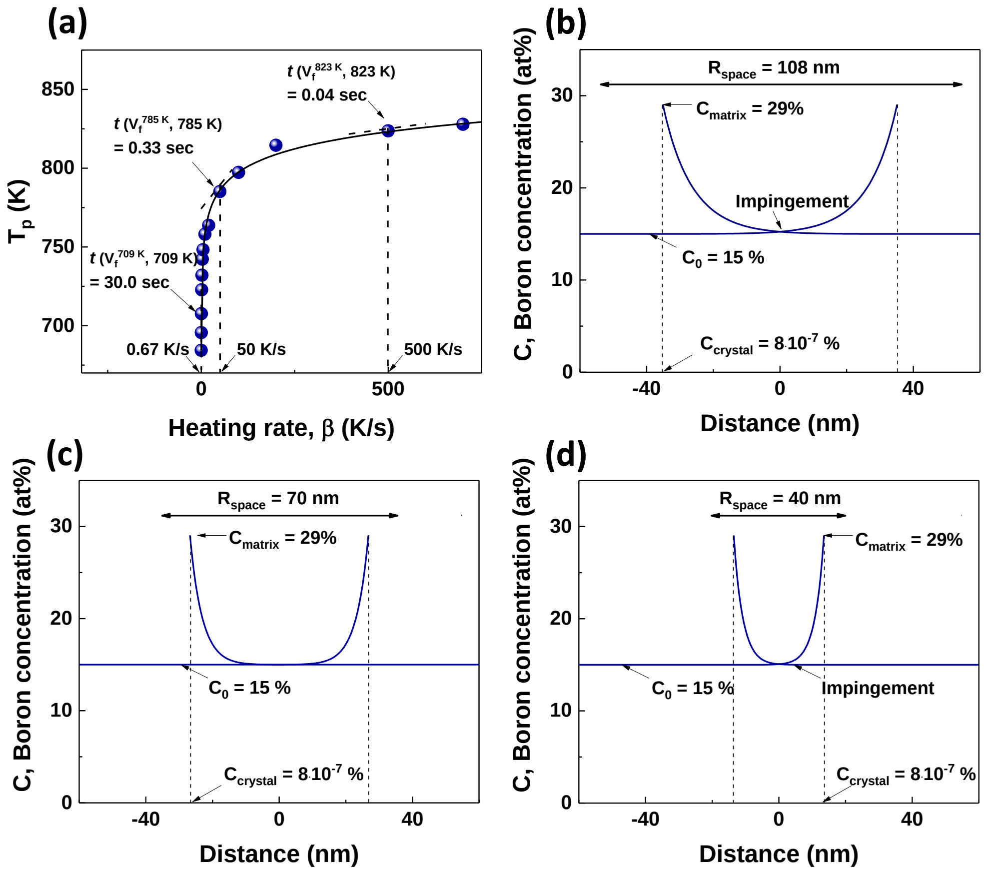

Fig. 49 (a) Contour plot of $V_f^{Tp}(\beta, T_p)$ with the tangential lines representing $t\left(V_f^{Tp}, T_p\right)$. Calculated diffusion field for B concentration (b) 108 nm, (c) 70nm, and (d) 40 nm separation with midpoint between nanocrystals. Detailed annealing conditions for calculations are described in the text.

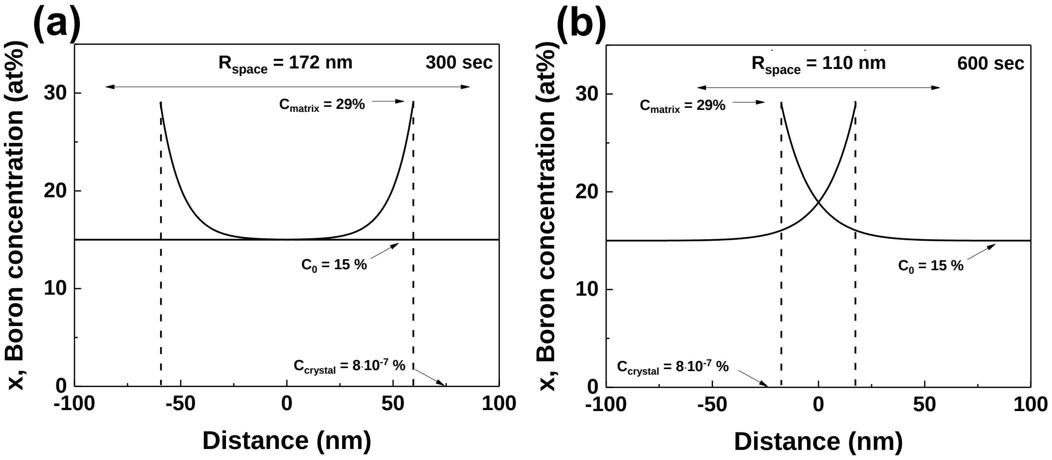

Fig. 50 Calculated diffusion field of B concentration after the isothermal annealing for (a) 300s and (b) 600s.

IV.2.4 Summary

This study highlights the importance of proper heating conditions for the processing of soft magnet materials with optimized microstructures. The size of the precipitated BCC-Fe nanocrystals in an amorphous $Fe_{85}B_{15}$ alloy during heating decreased from 50 nm to 15 nm and their number density increased from $0.09 \times 10^{22}\ m^{-3}$ to $1.6 \times 10^{22}\ m^{-3}$ with increasing heating rate from 0.67 K/s to 500 K/s. The diameter and number density of BCC-Fe nanocrystals are saturated at the heating rate of 3000 K/s. The CHT curve obtained from DSC and Flash DSC results explains that the primary crystallization of BCC-Fe occurred over the narrow temperature range. Thus, heating temperature should be controlled precisely to prevent the crystallization of the Fe_3B hard magnet phase that degrades the magnetic properties of $Fe_{85}B_{15}$ MG above 3000 K/s. Isothermal annealing tests and analysis of compositional profile were performed to interpret the limited size reduction of BCC-Fe and the eutectic decomposition of BCC-Fe and Fe_3B. The compositional profile of B solute between adjacent nanocrystals revealed that the diffusion-field impingement is the reason for the limited size reduction. The analysis results demonstrate that fast heating over 500 K/s is unnecessary for the manipulation of the binary Fe-B MG composite with the best magnetic properties and in fact will yield eutectic crystallization of BCC-Fe and Fe_3B with diminished magnetic performance.

Chapter V Concluding Remarks

Amorphous alloys offer an effective system for the separate study of the influence of local heterogeneities on the nucleation and growth mechanisms without the influence of excess vacancies or dislocations that confound the kinetics in crystalline materials. Thus, amorphous alloys provide a good model system for the systematic study of the influence spatial heterogeneities on the crystallization reaction.

In Al-Y-Fe-Cu amorphous alloys, the primary crystallization reaction yields ultrahigh densities from 10^{21} to 10^{23} m^{-3} of Al nanocrystals (10-20 nm in diameter) in an amorphous matrix. Structural analysis by TEM and FEM, kinetics measurements by DSC and Flash-DSC demonstrate that the nano-crystallization reaction is controlled by a heterogeneous nucleation catalyzed by medium range order (MRO) heterogeneities and is strongly affected by transient (non-steady state) kinetics. From the quantitative structural analysis, a nucleation model has been developed for the MRO catalysis of Al nanocrystals that is based upon Al nucleating around the MRO core to lower the nucleation barrier. With the MRO seeded nucleation model and the kinetic data from the delay time (τ) measurement, the evolution of the measured Al nanocrystal density (Nv) can be accounted for during the primary crystallization through the isothermal annealing treatments. Also, the predicted values of steady state nucleation rates (Jss) and the enthalpy ΔH at the onset crystallization temperature (Tx) given by the nucleation model are consistent with the experimental results. In addition, MRO seeded nucleation model has satisfied the constraints set by the thermodynamic, kinetic and structural parameters. The model reflects a generic scheme for the treatment of MRO mediated nucleation reactions which may be applied more broadly to nucleation in materials characterized by the presence of spatial heterogeneities.

We have also established that minor solute substitution by Cu has a dramatic effect on the crystallization behavior in terms of the nanocrystal densities and transient behavior that is related to local spatial heterogeneities. Compared to the change of MRO density (2 times), delay time change should be considered as the main factor in controlling the nucleation. Since the delay time is directly related to the atom attachment to an evolving nucleus, the Cu substitution is impacting the ability of Al atoms to attach to the nucleus. The mechanism underlying the changes in attachment frequency requires further study, but there is some insight from an MD study of Al-Sm alloys. The MD simulations indicated that the mobile Al atoms are constrained by the icosahedral like clusters in the glass and move as groupings. With increasing Sm content, the population of the icosahedral like clusters grows to further restrict the Al mobility that in turn inhibits crystal nucleation and promotes glass formation [62]. It is reasonable to expect that the Cu substitution in Al-Y-Fe alloys can have a similar effect on the Al attachment frequency, but further experimental study and analysis are necessary.

The primary crystallization in Fe-based glasses such as Fe-B-Si and Fe-B-Nb is of critical importance in optimizing the magnetic properties. The application of our nucleation model to the Fe-based glasses will serve as a test of the generality of the model. In this study, we discovered the size of the precipitated BCC-Fe nanocrystals in an amorphous $Fe_{85}B_{15}$ alloy during heating decreased from 50 nm to 15 nm and their number density increased from 0.09×10^{22} m^{-3} to 1.6×10^{22} m^{-3} with increasing heating rate from 0.67 K/s to 500 K/s. The CHT curve obtained from DSC and Flash DSC results visualized that the primary crystallization of BCC-Fe occurred at the relatively narrow heating rate range from 0.67 K/s to 3000 K/s, and Fe_3B phase that degrades the magnetic properties precipitated above the 3000 K/s. Isothermal annealing tests and analysis of compositional profile were performed to interpret the limited size reduction of BCC-Fe and eutectic decomposition of BCC-Fe and Fe_3B at in the high temperature regime. The compositional profile of B solute between adjacent nanocrystals revealed that the diffusion field impingement is the reason for the limited size reduction and eutectic decomposition of BCC-Fe and Fe_3B at high temperature regime. The analysis results demonstrate that fast heating over the 10^4 K/s is unnecessary for the manipulation of the binary Fe-B MG composite with the best magnetic properties and in fact will yield eutectic crystallization of BCC-Fe and Fe_3B with diminished magnetic performance.

Chapter VI Future Work

Further experiments and analysis are planned based on the present work. The new model on the primary nucleation of Al-Y-Fe and Al-Y-Fe-Cu systems has provided a basis for examination in other Al-based MGs system. This model provides guidance to the minor additions' effects in Al-Y-Fe alloys. Apart from the minor alloying effect of Cu, there are some other elements that can be introduced in the Al-Y-Fe system. It is found that the crystallization behavior and GFA are very sensitive to the minor alloy addition. Adding Ti and V into Al-Y-Fe alloy improved the difference between T_x and T_g which leads to better GFA. For Ti, V and Cu, all three elements have a negative enthalpy of mixing with Al. It suggests that strongly bound icosahedral clusters may form around the solute elements which have negative heat of mixing with Al. Based on the previous work and the commonly used prediction. Zr and Pd are picked as their negative enthalpy of mixing with Al. Pd has similar size with Cu but shows much lower heat of mixing with Al. For Zr, not only the mixing enthalpy with Al is negative but also the size mismatch with Al becomes bigger. TEM characterization and Flash DSC will be applied to measure the delay time for one specific composition which will be picked up from Zr and Pd. With similar techniques, the nucleation mechanism can be studied to control the crystallization. By increasing the delay to forestall crystallization it can be possible to achieve bulk Al-based MGs.

In addition, Fe-B binary MGs shows similar primary nucleation as Al-Y-Fe MGs. It is possible to control the nanocrystal nucleation in Fe-B MGs and get primary crystallized Fe-B MGs with brilliant soft magnetic properties. In this study, we successfully explained the heating rate influence on the diameter changes of BCC-Fe in binary $Fe_{85}B_{15}$ amorphous alloy. It was revealed that growth of BCC-Fe in $Fe_{85}B_{15}$ is governed by B-enriched diffusion field and their impingement. But the nucleation behavior at the high temperature regimes and eutectic crystallization (BCC-Fe+Fe_3B) is not discussed yet. As a future plan of this study, further analysis is planned based on the research procedures shown previous sections. Besides, influence of the B solute on the crystallization kinetics of BCC-Fe and Fe_3B in binary $Fe_{100-x}B_x$ amorphous alloys needs to be discussed.

Appendix A Quenched-in Nuclei Calculation under CNT

The goal of this set of calculations is to obtain an estimate of the nuclei number of size distribution that are quenched in during the melt spinning of Al alloys.

Assumption 1: The temperature of the melt drops linearly with time from the melting temperature, T_m, to room temperature T_r.

Assumption 2: During the quench, the melt has sufficient time to rearrange itself to equilibrium values.

Assumption 3: Once quenched in the nuclei do not grow significantly.

Assumption 4: Quenched-in nuclei are spherical in nature.

With these four assumptions, the distribution of quenched in nuclei can be assessed using conventional nucleation theory to calculate the flux of critical nuclei as a function of temperature, J(T), and then integrate this flux over temperature (and therefore time) during the quench to obtain.

$$\mathrm{N} = \frac{1}{\dot{\mathrm{T}}}\int_{\mathrm{T_m}}^{\mathrm{T_r}} \mathrm{J}\,(\mathrm{T})\mathrm{dT} \qquad \text{Eq C.1}$$

where the cooling rate is $\dot{\mathrm{T}} = 400000$ K/s which is around the critical cooling rate.

The flux of critical nuclei as a function of temperature (J(T)) is given by

$$\mathrm{J}(\mathrm{T_n}) = \boldsymbol{\rho\beta Z}\, exp\left(-\frac{\Delta G^*(r)}{kT}\right) \qquad \text{Eq C.2}$$

where ρ is the nucleation site density which is the density of Al atoms ($5.29\times10^{25}/\mathrm{m}^3$), β is the attachment frequency, *k* is the Boltzmann constant and *Z* is the Zeldovich factor that is estimated as 0.01. ΔG^* is the nucleation barrier given by

$$\Delta G^* = -\frac{4\pi\, \mathrm{r}^{*2}\sigma + (4/3)\pi\, \mathrm{r}^{*3}\, \Delta G_V}{\mathrm{kT}} \qquad \text{Eq C.3}$$

where r^* is the critical size, σ is the surface free energy, ΔG_V is the volume free energy associated with the liquid to solid transformation. The critical size can be taken from $r^* = -2\sigma/\Delta G_v$. Both ΔG_V and σ were calculated through methods listed in previous sections.

Fig. A1 represents the number of nuclei formed during quenching. Under CNT, density of Al nuclei formed in Al-Y-Fe MGs during quenching is around $1\times10^{13}/m^3$ in experimental temperature range. Besides, even changing the r* to the radius of MRO (0.85 nm), the number density can only reach $5\times10^{19}/m^3$, which is much lower than the MRO density tested under FEM ($5.2\times10^{25}/m^3$). Moreover, the calculations are based on the assumption of equilibrium at all temperatures, which is very unlikely at the rapid quench rate used for glass formation. Thus, the inherent MRO is different from the quench-in nuclei.

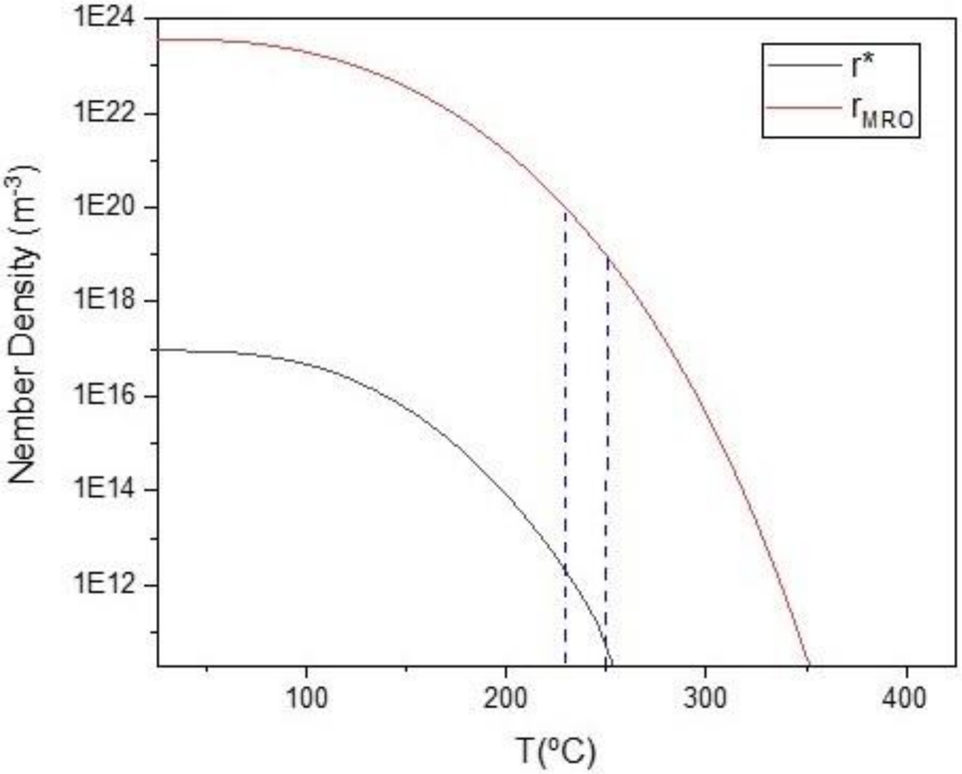

Fig. A1 Quenched-in nuclei calculation under CNT in Al-Y-Fe MG

Appendix B: Liquid-Solid Interface Energy

The crystal-glass interface energy $\sigma_{crystal/glass}$ is calculated through Spaepen's linear model[171], which evaluates the surface energy through the unstable equilibrium of a spherical crystal in an undercooled melt with an infinitely thin interface and a physical interface of width δ. The governing relations are listed below.

$$\sigma = \tilde{\sigma}\lambda T_L \Delta S_f \qquad \text{Eq B.1}$$

$$\tilde{\sigma} = \tilde{\delta}\{(\tilde{h} - \tilde{T}\tilde{s}) * (\tilde{h} - \tilde{T}\tilde{s} - \tilde{T} + 1) * \frac{1}{4}[(\tilde{h} - \tilde{T}\tilde{s})^{\frac{1}{2}} + (\tilde{h} - \tilde{T}\tilde{s} - \tilde{T} + 1)^{\frac{1}{2}}]^2\}^{\frac{1}{3}} \qquad \text{Eq B.2}$$

$$\tilde{h} = \Delta H_i / \Delta H_f \qquad \text{Eq B.3}$$

$$\tilde{s} = \Delta S_i / \Delta S_f \qquad \text{Eq B.4}$$

$$\tilde{T} = T / T_M \qquad \text{Eq B.5}$$

$$\tilde{\delta} = \delta / \lambda \qquad \text{Eq. B.6}$$

where $\tilde{s}, \tilde{h}, \tilde{T}, \tilde{\delta}$ and $\tilde{\sigma}$ are dimensionless parameters, ΔH_f is the enthalpy of fusion, ΔS_f is the entropy of fusion, ΔH_i and ΔS_i are the difference between the enthalpy or entropy of the interface and its respective value in the bulk liquid, T_M is the melting temperature, δ is the interface thickness and λ is an atomic dimension. The values and physical meanings of these parameters are summarized in **Table B1**. When the enthalpy is integrated across the interfacial layer region, the enthalpy term is directly proportional to the molar volume. Therefore, $\tilde{h}$ was estimated to be -0.10~-0.13. $\tilde{s}$ is calculated by $\tilde{s} = \frac{s_I + 1.46\Delta s_v}{\Delta s_f} - 1$, where s_I is the configurational entropy in the first interfacial layer (0.113 k/atom)[171], Δs_f is the entropy fusion per atom (1.38 k/atom for Al from thermodynamic evaluation), and $\Delta s_v$is the vibrational entropy. $\Delta s_v$is calculated to be 0.37 k/atom by $\Delta s_v = 3\gamma k \ln\frac{V_L}{V_c}$, where γ is the Gruneisen constant (2.12 for Al[191,192]), $\frac{V_L}{Vc}$is the relative expansion on melting and is calculated to be 1.06 by the density of the liquid and the solid Al at the melting point[193,194]. The $\sigma_{crystal/glass}$ value is calculated to be (0.16±0.003) +10^{-5}T (J/m^2)

Table B1 Summary of values and physical meaning of the parameters used in the Spaepen method calculation.

Parameter	T_L (K)	$\tilde{\delta}$	$\tilde{h}$	$\tilde{s}$	λ (m)	ΔS_f (J/m^3K)
Physical meaning	Liquidus temperature of metastable Al	Dimensionless thickness of one layer of interface	Dimensionless enthalpy of fusion	Dimensionless entropy of fusion	Atomic spacing	Entropy of fusion
Value	860	0.967	-0.10~-0.12	-0.52	0.39×10^{-9}	$1.0798\times10^{9}/T_L$

Appendix C: Driving Free Energy

According to the parallel tangent method described in the literature[15], the volume free energy (driving force) ΔG_v could be calculated as follows.

$$G_{\mathrm{XS,L}} = X_{Al}X_Y L_{L,Al-Y} + X_{Al}X_{Fe}L_{L,Al-Fe} + X_Y X_{Fe} L_{L,Fe-Y} + X_{Al}X_Y X_{Fe} L_{\text{Al-Y-Fe}} \quad \text{Eq C.1}$$

$$G_{ID,L} = RT[\, X_{Al}\, ln(X_{Al}) + X_Y\, ln(X_Y) + X_{Fe}\, ln(X_{Fe})\,] \quad \text{Eq C.2}$$

$$G_L = (X_{Al}G_{L,Al} + X_Y G_{L,Y} + X_{Fe}G_{L,Fe}) + G_{XS,L} + G_{ID,L} \quad \text{Eq C.3}$$

$$\Delta G_v = \Delta G_{FCC-L} = G_{FCC,Al} - \left(G_L - X_Y \frac{\delta G_L}{\delta X_Y} - X_{Fe}\frac{\delta G_L}{\delta X_{Fe}}\right) \quad \text{Eq C.4}$$

where the subscript “x_s” refers to the excess mixing energy, the subscript “ID” refers to the ideal mixing energy, L is an interaction parameter.

The values of the thermodynamic parameters are summarized in **Table C1**. After substituting all the parameters into the ΔG_{FCC-L}expression (Eq C.1), the driving force could be calculated. The $L_{Al-Y-Fe}$ parameter value has not been reported by the literature and was estimated to be zero because the $x_{Al}x_{Fe}x_Y L_{Al-Y-Fe}$term is very small. Also, none of the interaction parameter values were obtained directly for the Al-Y-Fe system and the reported values from different literature reports have discrepancies. Finally, the driving free energy ΔG_v can be calculated as -1.0185×10^6 (T-T_L) J/m^3 within an error range of (2.0941~0.8823) $\times10^6$ J/m^3 where T_L is calculated as 860±20 K.

Table C1 Thermodynamic parameters for Al-Y-Fe system.

Thermodynamic parameter (J/mol)	Reference
$L_{Al-Y-Fe} = 0$	[169]
$L_{L,Al-Fe} = (-91976.5 + 22.1314T) + (-5672.58 + 4.8728T)(x_{Al} - x_{Fe})$ $+121.9(x_{Al} - x_{Fe})^2$	[195]
$L_{L,Fe-Y} = (-36095.134 - 3.602385T + 0.0016606922T^2) +$ $(-5490.9858 - 16.447786T)(x_{Fe} - x_Y) + (26444226 - 23.30126T)(x_{Fe} - x_Y)^2$	[196]
$L_{L,Al-Y} = (-202611.3 + 4.63942T) + (-54350.11 + 0.28402T)(x_{Al} - x_Y)$ $+(83347.01 - 34.76401T)(x_{Al} - x_Y)^2 + (15488.69 - 0.7988T)(x_{Al} - x_Y)^3$ $+(-51205.9 + 30.2161T)(x_{Al} - x_Y)^4$	[197]
$G_{FCC,Al}(T \leq 700K) = -7976.15 + 137.093038T - 24.3671976T \times log(T)$ $-0.001884662T^2 - 0.000000877664T^3 + 74092/T$	[198]
$G_{FCC,Al}(T > 700K) = -11276.24 + 223.0484T - 38.5844296T \times log(T) +$ $0.018531982T^2 - 0.000005764227T^3 + 74092/T$	
$G_{L,Al}(T \leq 700K) = 3028.879 + 125.251171T - 24.367197T \times \log(T)$ $-0.001884662T^2 - 8.77664 \times 10^{-7}T^3 + 74092/T + 7.932 \times 10^{-20}T^7$	
$G_{L,Al}(T > 700K) = -271.21 + 211.206579T - 38.5844296T \times log(T)$ $+0.018531982T^2 - 5.764227 \times 10^{-6}T^3 + 74092/T + 7.934 \times 10^{-20}T^7$	
$G_{L,Y} = 3934.1 + 59.92169T - 14.814700T \times log(T) - 0.01562350T^2$ $+1.44295 \times 10^{-6}T^3 - 140695/T$	
$G2_{L,Fe} = 5.89269 \times 10^{-8}T^3 + 77358.5/T - 3.6751551 \times 10^{-21}T^7$	

REFERENCES

[1] W. Klement, R.H. Willens, P. Duwez, Non-crystalline structure in solidified Gold-Silicon alloys, Nature 187 (1960) 869–870. https://doi.org/10.1038/187869b0.

[2] P. Duwez, TYPICAL EXAMPLE OF METASTABILITY: METALLIC GLASSES., Journal of Vacuum Science and Technology B: Microelectronics and Nanometer Structures 1 (n.d.) 218–221. https://doi.org/10.1116/1.582490.

[3] A.L. Greer, E. Ma, Bulk Metallic Glasses: At the Cutting Edge of Metals Research, MRS Bull 32 (2007) 611–619. https://doi.org/10.1557/MRS2007.121.

[4] J.J. Kruzic, Bulk Metallic Glasses as Structural Materials: A Review, Adv Eng Mater 18 (2016) 1308–1331. https://doi.org/10.1002/ADEM.201600066.

[5] M. Fukuhara, M. Takahashi, Y. Kawazoe, A. Inoue, Electronic rule for formation of glassy alloys, Appl Phys Lett 90 (2007) 073114. https://doi.org/10.1063/1.2472565.

[6] A. Inoue, T. Zhang, T. Masumoto, Glass-forming ability of alloys, J Non Cryst Solids 156 (1993) 473–480. https://doi.org/10.1016/0022-3093(93)90003-G.

[7] A. Inoue, Amorphous, nanoquasicrystalline and nanocrystalline alloys in Al-based systems, Prog Mater Sci 43 (1998) 365–520. https://doi.org/10.1016/S0079-6425(98)00005-X.

[8] A. Inoue, Bulk Amorphous Alloys - Practical Characteristics and Applications, (1999).

[9] A. Inoue, T. Zhang, T. Masumoto, Al–La–Ni Amorphous Alloys with a Wide Supercooled Liquid Region, Materials Transactions, JIM 30 (1989) 965–972. https://doi.org/10.2320/MATERTRANS1989.30.965.

[10] A. Inoue, M. Yamamoto, H.M. Kimura, T. Masumoto, Ductile aluminium-base amorphous alloys with two separate phases, J Mater Sci Lett 6 (1987) 194–196. https://doi.org/10.1007/BF01728983/METRICS.

[11] G. Wilde, H. Sieber, J.H. Perepezko, Glass formation versus nanocrystallization in an Al92Sm8 alloy, Scr Mater 40 (1999) 779–783. https://doi.org/10.1016/S1359-6462(99)00029-9.

[12] X. Wang, D. Wang, B. Zhu, Y. Li, F. Han, Crystallization kinetics and thermal stability of mechanically alloyed Al76Ni8Ti8Zr4Y4 glassy powder, J Non Cryst Solids 385 (2014) 111–116. https://doi.org/10.1016/j.jnoncrysol.2013.11.015.

[13] R.I. Wu, G. Wilde, J.H. Perepezko, Glass formation and primary nanocrystallization in Al-base metallic glasses, Materials Science and Engineering: A 301 (2001) 12–17. https://doi.org/10.1016/S0921-5093(00)01390-3.

[14] J.H. Perepezko, R.J. Hebert, W.S. Tong, Amorphization and nanostructure synthesis in Al alloys, Intermetallics (Barking) 10 (2002) 1079–1088. https://doi.org/10.1016/S0966-9795(02)00144-9.

[15] J.H. Perepezko, R.J. Hebert, W.S. Tong, J. Hamann, H.R. Rösner, G. Wilde, Nanocrystallization Reactions in Amorphous Aluminum Alloys, Mater Trans 44 (2003) 1982–1992. https://doi.org/10.2320/matertrans.44.1982.

[16] M.J. Styles, W.W. Sun, D.R. East, J.A. Kimpton, M.A. Gibson, C.R. Hutchinson, On the competition in phase formation during the crystallisation of Al-Ni-Y

metallic glasses, Acta Mater 117 (2016) 170–187. https://doi.org/10.1016/j.actamat.2016.07.016.

[17] K.L. Sahoo, R. Sahu, A. Mitra, Kinetic aspects of the nanocrystallization and evolution of microhardness in Al92-xNi8Lax amorphous alloys, Materials and Manufacturing Processes 22 (2007) 497–501. https://doi.org/10.1080/10426910701236007.

[18] V. Sidorov, P. Svec, D. Janickovic, V. Mikhailov, L. Son, Magnetic properties and crystallization behavior of Al-Co-Ce(Dy) amorphous ribbons, J Magn Magn Mater 395 (2015) 324–328. https://doi.org/10.1016/j.jmmm.2015.07.072.

[19] A.P. Tsai, T. Kamiyama, Y. Kawamura, A. Inoue, T. Masumoto, Formation and precipitation mechanism of nanoscale Al particles in Al-Ni base amorphous alloys, Acta Mater 45 (1997) 1477–1487. https://doi.org/10.1016/S1359-6454(96)00268-6.

[20] Y. Shen, J.H. Perepezko, Investigation of the nucleation delay time in Al-based metallic glasses by high rate calorimetry, J Non Cryst Solids 502 (2018) 9–14. https://doi.org/10.1016/J.JNONCRYSOL.2018.10.014.

[21] Y.E. Kalay, L.S. Chumbley, I.E. Anderson, Crystallization behavior in a highly driven marginal glass forming alloy, J Non Cryst Solids 354 (2008) 3040–3048. https://doi.org/10.1016/J.JNONCRYSOL.2007.12.006.

[22] D. V. Louzguine-Luzgin, A. Inoue, Investigation of a rapidly solidified Al-based nanocomposite with extremely high number density of precipitates, Materials Science and Engineering A 448–451 (2007) 1026–1028. https://doi.org/10.1016/J.MSEA.2006.02.259.

[23] A.L. Greer, Metallic Glasses, Science (1979) 267 (1995) 1947–1953. https://doi.org/10.1126/SCIENCE.267.5206.1947.

[24] W.G. Stratton, J. Hamann, J.H. Perepezko, P.M. Voyles, X. Mao, S. V. Khare, Aluminum nanoscale order in amorphous Al92 Sm8 measured by fluctuation electron microscopy, Appl Phys Lett 86 (2005) 1–3. https://doi.org/10.1063/1.1897830/329837.

[25] F. Yi, P.M. Voyles, Analytical and computational modeling of fluctuation electron microscopy from a nanocrystal/amorphous composite, Ultramicroscopy 122 (2012) 37–47. https://doi.org/10.1016/j.ultramic.2012.07.022.

[26] F. Yi, S.D. Imhoff, J.H. Perepezko, P.M. Voyles, Nucleation of Al Nanocrystals in Solute-Substituted Al Metallic Glasses I: Structural characterization, (2023). https://doi.org/10.48550/arxiv.2301.04803.

[27] D. V. Louzguine, A. Inoue, Investigation of structure and properties of the Al-Y-Ni-Co-Cu metallic glasses, J Mater Res 17 (2002) 1014–1018. https://doi.org/10.1557/JMR.2002.0149.

[28] D. V. Louzguine-Luzgin, A. Inoue, Structure and transformation behaviour of a rapidly solidified Al-Y-Ni-Co-Pd alloy, J Alloys Compd 399 (2005) 78–85. https://doi.org/10.1016/J.JALLCOM.2005.02.018.

[29] T. Duan, Y. Shen, S.D. Imhoff, F. Yi, P.M. Voyles, J.H. Perepezko, Nucleation kinetics model for primary crystallization in Al–Y–Fe metallic glass, J Chem Phys 158 (2023) 064504. https://doi.org/10.1063/5.0135730.

[30] J.H. Perepezko, S.D. Imhoff, Primary crystallization reactions in Al-based metallic glass alloys, J Alloys Compd 504 (2010). https://doi.org/10.1016/J.JALLCOM.2010.02.063.
[31] Y. Yoshizawa, S. Oguma, K. Yamauchi, New Fe-based soft magnetic alloys composed of ultrafine grain structure, J Appl Phys 64 (1988) 6044–6046. https://doi.org/10.1063/1.342149.
[32] K. Suzuki, N. Kataoka, A. Inoue, T. Masumoto, A. Makino, High Saturation Magnetization and Soft Magnetic Properties of bcc Fe–Zr–B and Fe–Zr–B–M (M=Transition Metal) Alloys with Nanoscale Grain Size, Materials Transactions, JIM 32 (1991) 93–102. https://doi.org/10.2320/MATERTRANS1989.32.93.
[33] G. Herzer, Nanocrystalline soft magnetic materials, J Magn Magn Mater 157–158 (1996) 133–136. https://doi.org/10.1016/0304-8853(95)01126-9.
[34] L. Cui, H. Men, A. Makino, T. Kubota, K. Yubuta, M. Qi, A. Inoue, Effect of Cu and P on the Crystallization Behavior of Fe-Rich Hetero-Amorphous FeSiB Alloy, Mater Trans 50 (2009) 2515–2520. https://doi.org/10.2320/MATERTRANS.M2009206.
[35] M. Ohta, Y. Yoshizawa, Recent progress in high Bs Fe-based nanocrystalline soft magnetic alloys, J Phys D Appl Phys 44 (2011) 064004. https://doi.org/10.1088/0022-3727/44/6/064004.
[36] K. Suzuki, R. Parsons, B. Zang, K. Onodera, H. Kishimoto, T. Shoji, A. Kato, Nanocrystalline soft magnetic materials from binary alloy precursors with high saturation magnetization, AIP Adv 9 (2019) 35311. https://doi.org/10.1063/1.5079778/1077198.
[37] B. Zang, R. Parsons, K. Onodera, H. Kishimoto, A. Kato, A.C.Y. Liu, K. Suzuki, Effect of heating rate during primary crystallization on soft magnetic properties of melt-spun Fe-B alloys, Scr Mater 132 (2017) 68–72. https://doi.org/10.1016/J.SCRIPTAMAT.2017.01.030.
[38] R. Parsons, B. Zang, K. Onodera, H. Kishimoto, T. Shoji, A. Kato, K. Suzuki, Nano-crystallisation and magnetic softening in Fe–B binary alloys induced by ultra-rapid heating, J Phys D Appl Phys 51 (2018) 415001. https://doi.org/10.1088/1361-6463/AADAD6.
[39] D. V. Louzguine, A. Inoue, Crystallization behaviour of Al-based metallic glasses below and above the glass-transition temperature, J Non Cryst Solids 311 (2002) 281–293. https://doi.org/10.1016/S0022-3093(02)01375-3.
[40] A.L. Greer, Crystallisation kinetics of Fe80B20 glass, Acta Metallurgica 30 (1982) 171–192. https://doi.org/10.1016/0001-6160(82)90056-6.
[41] L.C. Chen, F. Spaepen, Analysis of calorimetric measurements of grain growth, J Appl Phys 69 (1991) 679–688. https://doi.org/10.1063/1.347349.
[42] J. William, R Mehl, Reaction kinetics in processes of nucleation and growth, Trans. Metall. Soc. AIME (1939). https://search.iczhiku.com/paper/SVJeV2doAnwD8vn5.pdf (accessed October 20, 2023).
[43] M. Avrami, Kinetics of Phase Change. I General Theory, J Chem Phys 7 (1939) 1103–1112. https://doi.org/10.1063/1.1750380.

[44] M. Avrami, Kinetics of Phase Change. II Transformation-Time Relations for Random Distribution of Nuclei, J Chem Phys 8 (1940) 212–224. https://doi.org/10.1063/1.1750631.

[45] M. Avrami, Granulation, Phase Change, and Microstructure Kinetics of Phase Change. III, J Chem Phys 9 (1941) 177–184. https://doi.org/10.1063/1.1750872.

[46] A. Calka, A.P. Radlinski, Decoupled bulk and surface crystallization in Pd85 Si15 glassy metallic alloys: Description of isothermal crystallization by a local value of the Avrami exponent, J Mater Res 3 (1988) 59–66. https://doi.org/10.1557/JMR.1988.0059.

[47] T. Demirtaş, Y.E. Kalay, Kinetics of fcc-Al nanocrystallization in Al90Tb10 metallic glass, J Non Cryst Solids 378 (2013) 71–78. https://doi.org/10.1016/j.jnoncrysol.2013.06.020.

[48] R. Lück, K. Lu, W. Frantz, JMA analysis of the transformation kinetics from the amorphous to the nanocrystalline state, Scripta Metallurgica et Materiala 28 (1993) 1071–1075. https://doi.org/10.1016/0956-716X(93)90012-H.

[49] P. Bruna, E. Pineda, D. Crespo, Phase-field modeling of glass crystallization: Change of the transport properties and crystallization kinetic, J Non Cryst Solids 353 (2007) 1002–1004. https://doi.org/10.1016/j.jnoncrysol.2006.12.086.

[50] M.D.H. Lay, A.J. Hill, P.G. Saksida, M.A. Gibson, T.J. Bastow, 27Al NMR measurement of fcc Al configurations in as-quenched Al85Ni11Y4 metallic glass and crystallization kinetics of Al nanocrystals, Acta Mater 60 (2012) 79–88. https://doi.org/10.1016/J.ACTAMAT.2011.09.007.

[51] K.C. Russell, Nucleation in solids: The induction and steady state effects, Adv Colloid Interface Sci 13 (1980) 205–318. https://doi.org/10.1016/0001-8686(80)80003-0.

[52] K.C. Russell, Linked flux analysis of nucleation in condensed phases, Acta Metallurgica 16 (1968) 761–769. https://doi.org/10.1016/0001-6160(68)90148-X.

[53] T. Duan, W. Kim, M. Gao, J.H. Perepezko, Crystallization of an undercooled Zn-based glass forming alloy, J Non Cryst Solids 627 (2024) 122823. https://doi.org/10.1016/J.JNONCRYSOL.2024.122823.

[54] O. Söhnel, J.W. Mullin, Interpretation of crystallization induction periods, J Colloid Interface Sci 123 (1988) 43–50. https://doi.org/10.1016/0021-9797(88)90219-6.

[55] J. Deubener, M.C. Weinberg, Crystal-liquid surface energies from transient nucleation, J Non Cryst Solids 231 (1998) 143–151. https://doi.org/10.1016/S0022-3093(98)00412-8.

[56] K.F. Kelton, A.L. Greer, Transient nucleation effects in glass formation, J Non Cryst Solids 79 (1986) 295–309. https://doi.org/10.1016/0022-3093(86)90229-2.

[57] I. Gutzow, J. Schmelzer, Kinetics of Crystallization and Segregation: Nucleation in Glass—Forming Systems, The Vitreous State (1995) 217–282. https://doi.org/10.1007/978-3-662-03187-2_6.

[58] V.M. Fokin, A.M. Kalinina, V.N. Filipovich, Nucleation in silicate glasses and effect of preliminary heat treatment on it, J Cryst Growth 52 (1981) 115–121. https://doi.org/10.1016/0022-0248(81)90178-0.

[59] V.M. Fokin, E.D. Zanotto, N.S. Yuritsyn, J.W.P. Schmelzer, Homogeneous crystal nucleation in silicate glasses: A 40 years perspective, J Non Cryst Solids 352 (2006) 2681–2714. https://doi.org/10.1016/j.jnoncrysol.2006.02.074.
[60] Y.T. Zhu, T.C. Lowe, R.J. Asaro, Assessment of the theoretical basis of the rule of additivity for the nucleation incubation time during continuous cooling, J Appl Phys 82 (1997) 1129–1137. https://doi.org/10.1063/1.365879.
[61] H.A. Kramers, Brownian motion in a field of force and the diffusion model of chemical reactions, Physica 7 (1940) 284–304. https://doi.org/10.1016/S0031-8914(40)90098-2.
[62] The process of diffusion through a rubber membrane, Proceedings of the Royal Society of London. Series A, Containing Papers of a Mathematical and Physical Character 97 (1920) 286–307. https://doi.org/10.1098/RSPA.1920.0034.
[63] D.T. Wu, The time lag in nucleation theory, J Chem Phys 97 (1992) 2644–2650. https://doi.org/10.1063/1.463052.
[64] G. Tarjus, D. Kivelson, Breakdown of the Stokes-Einstein relation in supercooled liquids, J Chem Phys 103 (1995) 3071–3073. https://doi.org/10.1063/1.470495.
[65] R. Androsch, C. Schick, J.W.P. Schmelzer, Sequence of enthalpy relaxation, homogeneous crystal nucleation and crystal growth in glassy polyamide 6, Eur Polym J 53 (2014) 100–108. https://doi.org/10.1016/j.eurpolymj.2014.01.012.
[66] P. Šimon, E. Illeková, S.C. Mojumdar, Kinetics of crystallization of metallic glasses studied by non-isothermal and isothermal DSC, J Therm Anal Calorim 83 (2006) 67–69. https://doi.org/10.1007/s10973-005-7067-z.
[67] L.Q. Xing, A. Mukhopadhyay, W.E. Buhro, K.F. Kelton, Improved Al-Y-Fe glass formation by microalloying with Ti, Philos Mag Lett 84 (2004) 293–302. https://doi.org/10.1080/09500830410001716113.
[68] P Predecki, BC Giessen, NJ Grant, New metastable alloy phases of gold silver and aluminum, Transactions of the Metallurgical Society of AIME (1985). https://scholar.google.com/scholar_lookup?&title=&journal=Trans.%20TMS-AIME&volume=233&pages=1438-39&publication_year=1965&author=Predecki%2CP.&author=Giessen%2CB.C.&author=Grant%2CN.J. (accessed October 20, 2023).
[69] H.A. Davies, J.B. Hull, An amorphous pahse in a splat-quenched A1-17.3 at %Cu alloy, Scripta Metallurgica 6 (1972) 241–245. https://doi.org/10.1016/0036-9748(72)90174-3.
[70] A. Inoue, A. Kitamura, T. Masumoto, The effect of aluminium on mechanical properties and thermal stability of (Fe, Co, Ni)-Al-B ternary amorphous alloys, J Mater Sci 16 (1981) 1895–1908. https://doi.org/10.1007/BF00540638/METRICS.
[71] Y. He, S.J. Poon, G.J. Shiflet, Synthesis and Properties of Metallic Glasses That Contain Aluminum, Science (1979) 241 (1988) 1640–1642. https://doi.org/10.1126/SCIENCE.241.4873.1640.
[72] U. Köster, U. Herold, Glassy Metals I, Springer-Verlag, Berlin (1981) 225. https://doi.org/10.1007/3540104402_10.
[73] R.D. Sá Lisboa, C. Bolfarini, W.J. Botta F., C.S. Kiminami, Topological instability as a criterion for design and selection of aluminum-based glass-former alloys, Appl Phys Lett 86 (2005) 1–3. https://doi.org/10.1063/1.1931047/931498.

[74] M.C. Gao, F. Guo, S.J. Poon, G.J. Shiflet, Development of fcc-Al nanocrystals in Al-Ni-Gd metallic glasses during continuous heating DSC scan, Materials Science and Engineering A 485 (2008) 532–543. https://doi.org/10.1016/J.MSEA.2007.08.009.

[75] Q. Li, E. Johnson, M.B. Madsen, A. Johansen, L. Sarholt-Kristensen, Crystallization of Al-based metallic glasses. Structural aspects, Philosophical Magazine B 66 (1992) 427–442. https://doi.org/10.1080/13642819208220112.

[76] S. Walter, D. Suttor, T. Erny, B. Hahn, P. Greil, J. Europ, B. Gerhard Wilde, N. Boucharat, R.J. Hebert, H. Rösner, W.S. Tong, J.H. Perepezko, H. Rösner, J.H. Perepezko, R.J. Hebert, W.S. Tong, Nanocrystallization in Al-rich Metallic Glasses, Adv Eng Mater 5 (2003) 125–130. https://doi.org/10.1002/ADEM.200390019.

[77] E. Pekarskaya, J.F. Löffler, W.L. Johnson, Microstructural studies of crystallization of a Zr-based bulk metallic glass, Acta Mater 51 (2003) 4045–4057. https://doi.org/10.1016/S1359-6454(03)00225-8.

[78] J.J. Yi, L.T. Kong, M. Ferry, C.G. Tang, G. Sha, J.F. Li, Origin of the separated α-Al nanocrystallization with Si added to Al86Ni9La5 amorphous alloy, Mater Charact 178 (2021). https://doi.org/10.1016/J.MATCHAR.2021.111199.

[79] J. Antonowicz, M. Kedzierski, E. Jezierska, J. Latuch, A.R. Yavari, L. Greer, P. Panine, M. Sztucki, Small-angle X-ray scattering from phase-separating amorphous metallic alloys undergoing nanocrystallization, J Alloys Compd 483 (2009) 116–119. https://doi.org/10.1016/j.jallcom.2008.08.117.

[80] A.K. Gangopadhyay, T.K. Croat, K.F. Kelton, Effect of phase separation on subsequent crystallization in Al88Gd6La2Ni4, Acta Mater 48 (2000) 4035–4043. https://doi.org/10.1016/S1359-6454(00)00196-8.

[81] K.K. Sahu, N.A. Mauro, L. Longstreth-Spoor, D. Saha, Z. Nussinov, M.K. Miller, K.F. Kelton, Phase separation mediated devitrification of Al88Y 7Fe5 glasses, Acta Mater 58 (2010) 4199–4206. https://doi.org/10.1016/j.actamat.2010.04.011.

[82] G. Abrosimova, A. Aronin, A. Budchenko, Amorphous phase decomposition in Al-Ni-RE system alloys, Mater Lett 139 (2015) 194–196. https://doi.org/10.1016/j.matlet.2014.10.076.

[83] G.E. Abrosimova, A.S. Aronin, O.I. Barkalov, M.M. Dement’eva, Formation of the nanostructure in amorphous alloys of the Al-Ni-Y system, Physics of the Solid State 55 (2013) 1773–1778. https://doi.org/10.1134/S1063783413090023.

[84] Y.B. Wang, H.W. Yang, B.B. Sun, B. Wu, J.Q. Wang, M.L. Sui, E. Ma, Evidence of phase separation correlated with nanocrystallization in Al85Ni5Y6Fe2Co2 metallic glass, Scr Mater 55 (2006) 469–472. https://doi.org/10.1016/j.scriptamat.2006.05.005.

[85] Y.E. Kalay, I. Kalay, J. Hwang, P.M. Voyles, M.J. Kramer, Local chemical and topological order in Al-Tb and its role in controlling nanocrystal formation, Acta Mater 60 (2012) 994–1003. https://doi.org/10.1016/j.actamat.2011.11.008.

[86] B. Radiguet, D. Blavette, N. Wanderka, J. Banhart, K.L. Sahoo, Segregation-controlled nanocrystallization in an Al-Ni-La metallic glass, Appl Phys Lett 92 (2008) 103126. https://doi.org/10.1063/1.2897303.

[87] J. Antonowicz, A.R. Yavari, W.J. Botta, P. Panine, Phase separation and nanocrystallization in Al92Sm8 metallic glass, Philosophical Magazine 86 (2006) 4235–4242. https://doi.org/10.1080/14786430500375175.

[88] J. Antonowicz, E. Jezierska, M. Kedzierski, A.R. Yavari, L. Greer, P. Panine, M. Sztucki, Early stages of phase separation and nanocrystallization in Al-rare earth metallic glasses studied using SAXS/WAXS and HRTEM methods, Reviews on Advanced Materials Science 18 (2008) 454–458.

[89] J.E. Spowart, D.B. Miracle, H.M. Mullens, The influence of solute distribution on the high nucleation density of Al crystals in amorphous aluminum alloys, J Non Cryst Solids 336 (2004) 202–211. https://doi.org/10.1016/j.jnoncrysol.2004.02.011.

[90] J.C. Foley, D.R. Allen, J.H. Perepezko, Analysis of nanocrystal development in Al-Y-Fe and Al-Sm glasses, Scr Mater 35 (1996) 655–660. https://doi.org/10.1016/1359-6462(96)00196-0.

[91] K. Nakazato, Y. Kawamura, A.P. Tsai, A. Inoue, T. Masumoto, On the growth of nanocrystalline grains in an aluminum-based amorphous alloy, Appl Phys Lett 63 (1993) 2644–2646. https://doi.org/10.1063/1.110407.

[92] S. Trady, M. Mazroui, A. Hasnaoui, K. Saadouni, Microstructural evolutions and fractal characteristics in medium range level in AlxNi100-x alloys during rapid solidification process, J Alloys Compd 744 (2018) 750–758. https://doi.org/10.1016/J.JALLCOM.2018.02.131.

[93] W. Li, L.T. Kong, J.F. Li, Thermal stability and crystallization behavior of Al86Ni9Y5 amorphous alloys with different Si addition, Mater Charact 194 (2022). https://doi.org/10.1016/J.MATCHAR.2022.112387.

[94] B. Gu, F. Liu, Characterization of structural inhomogeneity in Al88Ce8Co4 metallic glass, Acta Mater 112 (2016) 94–104. https://doi.org/10.1016/J.ACTAMAT.2016.04.009.

[95] F. Li, X.J. Liu, H.Y. Hou, G. Chen, G.L. Chen, Structural origin underlying poor glass forming ability of Al metallic glass, J Appl Phys 110 (2011). https://doi.org/10.1063/1.3605510.

[96] D. Moroni, P.R. Ten Wolde, P.G. Bolhuis, Interplay between structure and size in a critical crystal nucleus, Phys Rev Lett 94 (2005). https://doi.org/10.1103/PHYSREVLETT.94.235703.

[97] B.S. Lee, G.W. Burr, R.M. Shelby, S. Raoux, C.T. Rettner, S.N. Bogle, K. Darmawikarta, S.G. Bishop, J.R. Abelson, Observation of the role of subcritical nuclei in crystallization of a glassy solid, Science (1979) 326 (2009) 980–984. https://doi.org/10.1126/SCIENCE.1177483.

[98] J.H. Li, Y. Dai, Y.Y. Cui, B.X. Liu, Atomistic theory for predicting the binary metallic glass formation, Materials Science and Engineering R: Reports 72 (2011) 1–28. https://doi.org/10.1016/J.MSER.2010.09.002.

[99] W.D. Liu, H.H. Ruan, L.C. Zhang, Atomic rearrangements in metallic glass: Their nucleation and self-organization, Acta Mater 61 (2013) 6050–6060. https://doi.org/10.1016/J.ACTAMAT.2013.06.046.

[100] S. Menon, G. Díaz Leines, R. Drautz, J. Rogal, Role of pre-ordered liquid in the selection mechanism of crystal polymorphs during nucleation, Journal of Chemical Physics 153 (2020). https://doi.org/10.1063/5.0017575.

[101] G. Díaz Leines, A. Michaelides, J. Rogal, Interplay of structural and dynamical heterogeneity in the nucleation mechanism in nickel, Faraday Discuss 235 (2021) 406–415. https://doi.org/10.1039/D1FD00099C.

[102] M. Fitzner, G.C. Sosso, F. Pietrucci, S. Pipolo, A. Michaelides, Pre-critical fluctuations and what they disclose about heterogeneous crystal nucleation, Nat Commun 8 (2017). https://doi.org/10.1038/S41467-017-02300-X.

[103] E.D. Zanotto, M. Montazerian, Dominant Effect of Heterogeneous Dynamics on Homogenous Crystal Nucleation in Supercooled Liquids, Front Phys 8 (2020). https://doi.org/10.3389/FPHY.2020.00020.

[104] G.C. Sosso, J. Chen, S.J. Cox, M. Fitzner, P. Pedevilla, A. Zen, A. Michaelides, Crystal Nucleation in Liquids: Open Questions and Future Challenges in Molecular Dynamics Simulations, Chem Rev 116 (2016) 7078–7116. https://doi.org/10.1021/ACS.CHEMREV.5B00744.

[105] G.W. Lee, Y.C. Cho, B. Lee, K.F. Kelton, Interfacial free energy and medium range order: Proof of an inverse of Frank's hypothesis, Phys Rev B 95 (2017). https://doi.org/10.1103/PHYSREVB.95.054202.

[106] Y. Sun, Y. Zhang, F. Zhang, Z. Ye, Z. Ding, C.Z. Wang, K.M. Ho, Cooling rate dependence of structural order in Al90Sm10 metallic glass, J Appl Phys 120 (2016). https://doi.org/10.1063/1.4955223.

[107] L. Zhao, G.B. Bokas, J.H. Perepezko, I. Szlufarska, Nucleation kinetics in Al-Sm metallic glasses, Acta Mater 142 (2018) 1–7. https://doi.org/10.1016/J.ACTAMAT.2017.09.050.

[108] A. Inoue, H. Ohtera, T. Masumoto, Anomalous X-ray Scattering on Amorphous Al87Y8Ni5 and A190Y10 Alloys, Zeitschrift Fur Naturforschung - Section A Journal of Physical Sciences 44 (1989) 814–820. https://doi.org/10.1515/ZNA-1989-0907/MACHINEREADABLECITATION/RIS.

[109] D.B. Miracle, O.N. Senkov, A geometric model for atomic configurations in amorphous Al alloys, J Non Cryst Solids 319 (2003) 174–191. https://doi.org/10.1016/S0022-3093(02)01917-8.

[110] D.B. Miracle, A structural model for metallic glasses, Nature Materials 2004 3:10 3 (2004) 697–702. https://doi.org/10.1038/nmat1219.

[111] D.B. Miracle, E.A. Lord, S. Ranganathan, Candidate Atomic Cluster Configurations in Metallic Glass Structures, Mater Trans 47 (2006) 1737–1742. https://doi.org/10.2320/MATERTRANS.47.1737.

[112] W.S. Sanders, J.S. Warner, D.B. Miracle, Stability of Al-rich glasses in the Al-La-Ni system, Intermetallics (Barking) 14 (2006) 348–351. https://doi.org/10.1016/J.INTERMET.2005.06.009.

[113] M.M.J. Treacy, J.M. Gibson, L. Fan, D.J. Paterson, I. McNulty, Fluctuation microscopy: a probe of medium range order, Reports on Progress in Physics 68 (2005) 2899. https://doi.org/10.1088/0034-4885/68/12/R06.

[114] P.M. Voyles, J.R. Abelson, Medium-range order in amorphous silicon measured by fluctuation electron microscopy, Solar Energy Materials and Solar Cells 78 (2003) 85–113. https://doi.org/10.1016/S0927-0248(02)00434-8.

[115] L.N. Nittala, S. Jayaraman, B.A. Sperling, J.R. Abelson, Hydrogen-induced modification of the medium-range structural order in amorphous silicon films, Appl Phys Lett 87 (2005) 1–3. https://doi.org/10.1063/1.2143124/905964.

[116] H.W. Sheng, Y.Q. Cheng, P.L. Lee, S.D. Shastri, E. Ma, Atomic packing in multicomponent aluminum-based metallic glasses, Acta Mater 56 (2008) 6264–6272. https://doi.org/10.1016/J.ACTAMAT.2008.08.049.

[117] A. Inoue, F. Kong, S. Zhu, C.T. Liu, F. Al-Marzouki, Development and applications of highly functional al-based materials by use of metastable phases, Materials Research 18 (2015) 1414–1425. https://doi.org/10.1590/1516-1439.058815.

[118] Y. Zhang, M.X. Pan, D.Q. Zhao, R.J. Wang, W.H. Wang, Formation of Zr-Based Bulk Metallic Glasses from Low Purity of Materials by Yttrium Addition, Materials Transactions, JIM 41 (2000) 1410–1414. https://doi.org/10.2320/MATERTRANS1989.41.1410.

[119] C.T. Liu, M.F. Chisholm, M.K. Miller, Oxygen impurity and microalloying effect in a Zr-based bulk metallic glass alloy, Intermetallics (Barking) 10 (2002) 1105–1112. https://doi.org/10.1016/S0966-9795(02)00131-0.

[120] Z.P. Lu, C.T. Liu, W.D. Porter, Role of yttrium in glass formation of Fe-based bulk metallic glasses, Appl Phys Lett 83 (2003) 2581–2583. https://doi.org/10.1063/1.1614833.

[121] B. Liu, L. Liu, The effect of microalloying on thermal stability and corrosion resistance of Cu-based bulk metallic glasses, Materials Science and Engineering: A 415 (2006) 286–290. https://doi.org/10.1016/J.MSEA.2005.09.099.

[122] K.S. Bondi, A.K. Gangopadhyay, Z. Marine, T.H. Kim, A. Mukhopadhyay, A.I. Goldman, W.E. Buhro, K.F. Kelton, Effects of microalloying with 3d transition metals on glass formation in AlYFe alloys, J Non Cryst Solids 353 (2007) 4723–4731. https://doi.org/10.1016/j.jnoncrysol.2007.06.063.

[123] Y. Shen, J.H. Perepezko, Al-based amorphous alloys: Glass-forming ability, crystallization behavior and effects of minor alloying additions, J Alloys Compd 707 (2017) 3–11. https://doi.org/10.1016/J.JALLCOM.2016.11.079.

[124] Y. Shen, J.H. Perepezko, The effect of minor addition of insoluble elements on transformation kinetics in amorphous Al alloys, (2015). https://doi.org/10.1016/j.jallcom.2014.12.276.

[125] A. Mukhopadhyay, K.E. Spence, L.Q. Xing, W.E. Buhro, K.F. Kelton, An Al-rich metallic glass with a large supercooled liquid region, Philosophical Magazine 87 (2007) 281–290. https://doi.org/10.1080/14786430600953798.

[126] J.-H. Jun, J.-M. Kim, K.-T. Kim, W.-J. Jung, Glass formability and thermal stability of Al-Ni-Y-Be amorphous alloys, J Alloys Compd 434 (2007) 190–193. https://doi.org/10.1016/j.jallcom.2006.08.120.

[127] M.F. De Oliveira, L.C.R. Aliaga, C. Bolfarini, W.J. Botta, C.S. Kiminami, Thermodynamic and topological instability approaches for forecasting glass-

forming ability in the ternary Al-Ni-Y system, J Alloys Compd 464 (2008) 118–121. https://doi.org/10.1016/j.jallcom.2007.09.094.
[128] M.J. Styles, W.W. Sun, D.R. East, J.A. Kimpton, M.A. Gibson, C.R. Hutchinson, On the competition in phase formation during the crystallisation of Al-Ni-Y metallic glasses, (2016). https://doi.org/10.1016/j.actamat.2016.07.016.
[129] S.P. Sun, D.Q. Yi, H.Q. Liu, B. Zang, Y. Jiang, Calculation of glass forming ranges in Al-Ni-RE (Ce, La, Y) ternary alloys and their sub-binaries based on Miedema's model, J Alloys Compd 506 (2010) 377–387. https://doi.org/10.1016/j.jallcom.2010.07.011.
[130] S.-F. Chen, J.-K. Chen, S.-L. Lin, Y.-L. Lin, Effects of B upon glass forming ability of Al 87 Y 8 Ni 5 amorphous alloy, (2013). https://doi.org/10.1016/j.jallcom.2013.02.135.
[131] M. Gögebakan, The effect of Si addition on crystallization behavior of amorphous Al-Y-Ni alloy, J Mater Eng Perform 13 (2004) 504–508. https://doi.org/10.1361/10599490419171.
[132] S.-F. Chen, C.-Y. Chen, C.-H. Lin, Insight on the glass-forming ability of Al-Y-Ni-Ce bulk metallic glass, (2015). https://doi.org/10.1016/j.jallcom.2015.02.217.
[133] M. Yewondwossent, R.A. Dunlapt, D.J. Lloyd, Thermal and electronic properties of amorphous AI,Y,Ni,-,TM, (TM=Mn, Fe, CO, Cu), (1992) 461–472.
[134] Z. Zhang, X.Z. Xiong, W. Zhou, X. Lin, A. Inoue, J.F. Li, Glass forming ability and crystallization behavior of AleNieRE metallic glasses, (2013). https://doi.org/10.1016/j.intermet.2013.05.003.
[135] F.G. Cuevas, S. Lozano-Perez, R.M. Aranda, R. Astacio, Crystallization Process and Microstructural Evolution of Melt Spun Al-RE-Ni-(Cu) Ribbons, Metals 2020, Vol. 10, Page 443 10 (2020) 443. https://doi.org/10.3390/MET10040443.
[136] W. Li, L.T. Kong, J.F. Li, The alloying effects of Ge and Si on thermal stability and crystallization behavior of Al-Y binary amorphous alloys, J Non Cryst Solids 575 (2022) 121197. https://doi.org/10.1016/J.JNONCRYSOL.2021.121197.
[137] S.F. Chen, C.Y. Chen, C.H. Lin, Insight on the glass-forming ability of Al–Y–Ni–Ce bulk metallic glass, J Alloys Compd 637 (2015) 418–425. https://doi.org/10.1016/J.JALLCOM.2015.02.217.
[138] S.J. Hong, P.J. Warren, B.S. Chun, Nanocrystallization behaviour of Al–Y–Ni with Cu additions, Materials Science and Engineering: A 304–306 (2001) 362–366. https://doi.org/10.1016/S0921-5093(00)01480-5.
[139] Y.H. Kim, A. Inoue, T. Masumoto, Ultrahigh Mechanical Strengths of Al88Y2Ni10−xMx (M = Mn, Fe or Co) Amorphous Alloys Containing Nanoscale fcc-Al Particles, Materials Transactions, JIM 32 (1991) 599–608. https://doi.org/10.2320/matertrans1989.32.599.
[140] F.G. Cuevas, S. Lozano-Perez, R.M. Aranda, F. Ternero, Crystallisation of amorphous Al-Y-Ni-(Cu) alloys, J Non Cryst Solids 512 (2019) 15–24. https://doi.org/10.1016/J.JNONCRYSOL.2019.02.013.
[141] M. Gögebakan, The effect of Si addition on crystallization behavior of amorphous Al-Y-Ni alloy, J Mater Eng Perform 13 (2004) 504–508. https://doi.org/10.1361/10599490419171/METRICS.

[142] J. Latuch, A. Kokoszkiewicz, H. Matyja, The effect of Cu addition on the formation of f.c.c.-Al phase in rapidly quenched Al-Y-Ni alloys, Materials Science and Engineering: A 226–228 (1997) 809–812. https://doi.org/10.1016/S0921-5093(97)80084-6.

[143] P.J. Squire, I.T.H. Chang, Development of rapidly solidified Al–Y–Ni-based alloys, Materials Science and Engineering: A 449–451 (2007) 1009–1012. https://doi.org/10.1016/J.MSEA.2006.02.274.

[144] J.H. Perepezko, S.D. Imhoff, R.J. Hebert, Nanostructure development during devitrification and deformation, J Alloys Compd 495 (2010) 360–364. https://doi.org/10.1016/j.jallcom.2009.10.051.

[145] J.P. Liao, B.J. Yang, Y. Zhang, W.Y. Lu, X.J. Gu, J.Q. Wang, Evaluation of glass formation and critical casting diameter in Al-based metallic glasses, Mater Des 88 (2015) 222–226. https://doi.org/10.1016/j.matdes.2015.08.138.

[146] M. Salehi, S.G. Shabestari, S.M.A. Boutorabi, Nanostructure evolution and mechanical properties of rapidly solidified Al3Ni3RE (Y, Ce) alloys, Materials Science and Engineering: A 586 (2013) 407–412. https://doi.org/10.1016/j.msea.2013.08.040.

[147] B.J. Yang, J.H. Yao, Y.S. Chao, J.Q. Wang, E. Ma, Developing aluminum-based bulk metallic glasses, Philosophical Magazine 90 (2010) 3215–3231. https://doi.org/10.1080/14786435.2010.484401.

[148] C. Dong, J.B. Qiang, Y.M. Wang, N. Jiang, J. Wu, P. Thiel, Cluster-based composition rule for stable ternary quasicrystals in Al-(Cu, Pd, Ni)-TM systems, Philosophical Magazine 86 (2006) 263–274. https://doi.org/10.1080/14786430500281308.

[149] Y.Q. Cheng, E. Ma, Atomic-level structure and structure-property relationship in metallic glasses, Prog Mater Sci 56 (2011) 379–473. https://doi.org/10.1016/j.pmatsci.2010.12.002.

[150] B.J. Yang, J.H. Yao, J. Zhang, H.W. Yang, J.Q. Wang, E. Ma, Al-rich bulk metallic glasses with plasticity and ultrahigh specific strength, Scr Mater 61 (2009) 423–426. https://doi.org/10.1016/j.scriptamat.2009.04.035.

[151] G.B. Bokas, L. Zhao, J.H. Perepezko, I. Szlufarska, On the role of Sm in solidification of Al-Sm metallic glasses, Scr Mater 124 (2016) 99–102. https://doi.org/10.1016/j.scriptamat.2016.06.045.

[152] D.D. Wen, P. Peng, Y.Q. Jiang, Z.A. Tian, W. Li, R.S. Liu, Correlation of the heredity of icosahedral clusters with the glass forming ability of rapidly solidified CuxZr100 - X alloys, J Non Cryst Solids 427 (2015) 199–207. https://doi.org/10.1016/j.jnoncrysol.2015.07.019.

[153] J. Xi, G. Bokas, L.E. Schultz, M. Gao, L. Zhao, Y. Shen, J.H. Perepezko, D. Morgan, I. Szlufarska, Microalloying effect in ternary Al-Sm-X (X = Ag, Au, Cu) metallic glasses studied by ab initio molecular dynamics, Comput Mater Sci 185 (2020) 109958. https://doi.org/10.1016/j.commatsci.2020.109958.

[154] F. Audebert, M. Galano, F. Saporiti, The use of Nb in rapid solidified Al alloys and composites, J Alloys Compd 615 (2015) S621–S626. https://doi.org/10.1016/j.jallcom.2013.12.129.

[155] X.M. Shi, X.D. Wang, Q. Yu, Q.P. Cao, D.X. Zhang, J. Zhang, T.D. Hu, L.H. Lai, H.L. Xie, T.Q. Xiao, J.Z. Jiang, Structure alterations in Al-Y-based metallic glasses with la and Ni addition, J Appl Phys 119 (2016) 114904. https://doi.org/10.1063/1.4944653.
[156] Y. Liu, J. Wang, J. Qin, G. Schumacher, Influence of Ag substitution on the local structure and glass-forming ability of Al86Ni(8-x)Y6Agx (X = 0,1,2) liquids, Phys Chem Liquids 54 (2016) 98–109. https://doi.org/10.1080/00319104.2015.1084880.
[157] J. Yi, W. Xu, X. Xiong, L. Kong, M. Ferry, J. Li, Glass-Forming Ability and Crystallization Behavior of Al 86 Ni 9 La 5 Metallic Glass with Si Addition**, (2015). https://doi.org/10.1002/adem.201500354.
[158] N. Wang, Y.E. Kalay, R. Trivedi, Eutectic-to-metallic glass transition in the Al-Sm system, Acta Mater 59 (2011) 6604–6619. https://doi.org/10.1016/j.actamat.2011.07.015.
[159] U. Köster, P. Weiss, Crystallization and decomposition of amorphous silicon-aluminium films, J Non Cryst Solids 17 (1975) 359–368. https://doi.org/10.1016/0022-3093(75)90126-X.
[160] D. V. Louzguine, V.I. Pol'kin, Bulk metallic glasses: Fabrication, structure, and structural changes under heating, Russian Journal of Non-Ferrous Metals 57 (2016) 25–32. https://doi.org/10.3103/S1067821216010107.
[161] W. Kim, T. Duan, J.H. Perepezko, Nanocrystal evolution during ultra-fast heating in an amorphous Fe85B15 alloy, Scr Mater 225 (2023). https://doi.org/10.1016/J.SCRIPTAMAT.2022.115155.
[162] J. Zhou, J. You, K. Qiu, Advances in Fe-based amorphous/nanocrystalline alloys, J Appl Phys 132 (2022). https://doi.org/10.1063/5.0092662/2837128.
[163] Y.Q. Zeng, J.S. Yu, Y. Tian, A. Hirata, T. Fujita, X.H. Zhang, N. Nishiyama, H. Kato, J.Q. Jiang, A. Inoue, M.W. Chen, Improving glass forming ability of off-eutectic metallic glass formers by manipulating primary crystallization reactions, Acta Mater 200 (2020) 710–719. https://doi.org/10.1016/J.ACTAMAT.2020.09.042.
[164] H.W. Kui, A.L. Greer, D. Turnbull, Formation of bulk metallic glass by fluxing, Appl Phys Lett 45 (1984) 615–616. https://doi.org/10.1063/1.95330.
[165] S. V. Ketov, L. V. Louzguina-Luzgina, A.Y. Churyumov, A.N. Solonin, D.B. Miracle, D. V. Louzguine-Luzgin, A. Inoue, Glass-formation and crystallization processes in Ag–Y–Cu alloys, J Non Cryst Solids 358 (2012) 1759–1763. https://doi.org/10.1016/J.JNONCRYSOL.2012.05.012.
[166] A. Wang, C. Zhao, A. He, H. Men, C. Chang, X. Wang, Composition design of high Bs Fe-based amorphous alloys with good amorphous-forming ability, J Alloys Compd 656 (2016) 729–734. https://doi.org/10.1016/J.JALLCOM.2015.09.216.
[167] H.R. Lashgari, D. Chu, S. Xie, H. Sun, M. Ferry, S. Li, Composition dependence of the microstructure and soft magnetic properties of Fe-based amorphous/nanocrystalline alloys: A review study, J Non Cryst Solids 391 (2014) 61–82. https://doi.org/10.1016/J.JNONCRYSOL.2014.03.010.

[168] D.T. Schweiss, J. Hwang, P.M. Voyles, Inelastic and elastic mean free paths from FIB samples of metallic glasses, Ultramicroscopy 124 (2013) 6–12. https://doi.org/10.1016/J.ULTRAMIC.2012.08.005.

[169] D.R. Allen, J.C. Foley, J.H. Perepezko, Nanocrystal development during primary crystallization of amorphous alloys, Acta Mater 46 (1998) 431–440. https://doi.org/10.1016/S1359-6454(97)00279-6.

[170] Y.X. Zhuang, J.Z. Jiang, Z.G. Lin, M. Mezouar, W. Crichton, A. Inoue, Evidence of eutectic crystallization and transient nucleation in Al89La6Ni5 amorphous alloy, Appl Phys Lett 79 (2001) 743–745. https://doi.org/10.1063/1.1389506.

[171] F. Spaepen, Homogeneous Nucleation and the Temperature Dependence of the Crystal-Melt Interfacial Tension, Solid State Physics - Advances in Research and Applications 47 (1994) 1–32. https://doi.org/10.1016/S0081-1947(08)60638-4.

[172] K.F. (Kenneth F.) Kelton, A.L. (Alan L. Greer, Nucleation in condensed matter : applications in materials and biology, Elsevier, Oxford, 2010.

[173] Y.T. Shen, T.H. Kim, A.K. Gangopadhyay, K.F. Kelton, Icosahedral order, frustration, and the glass transition: Evidence from time-dependent nucleation and supercooled liquid structure studies, Phys Rev Lett 102 (2009). https://doi.org/10.1103/PHYSREVLETT.102.057801.

[174] K.C. Russell, Nucleation in solids: The induction and steady state effects, Adv Colloid Interface Sci 13 (1980) 205–318. https://doi.org/10.1016/0001-8686(80)80003-0.

[175] K.F. Kelton, Crystal Nucleation in Liquids and Glasses, Solid State Physics - Advances in Research and Applications 45 (1991) 75–177. https://doi.org/10.1016/S0081-1947(08)60144-7.

[176] F. Faupel, W. Frank, M.P. Macht, H. Mehrer, V. Naundorf, K. Rätzke, H.R. Schober, S.K. Sharma, H. Teichler, Diffusion in metallic glasses and supercooled melts, Rev Mod Phys 75 (2003) 237–280. https://doi.org/10.1103/REVMODPHYS.75.237.

[177] G. Vanden Poel, V.B.F. Mathot, High-speed/high performance differential scanning calorimetry (HPer DSC): Temperature calibration in the heating and cooling mode and minimization of thermal lag, Thermochim Acta 446 (2006) 41–54. https://doi.org/10.1016/J.TCA.2006.02.022.

[178] N. Sohrabi, J.E.K. Schawe, J. Jhabvala, J.F. Löffler, R.E. Logé, Critical crystallization properties of an industrial-grade Zr-based metallic glass used in additive manufacturing, Scr Mater 199 (2021) 113861. https://doi.org/10.1016/J.SCRIPTAMAT.2021.113861.

[179] J.E.K. Schawe, S. Pogatscher, J.F. Löffler, Thermodynamics of polymorphism in a bulk metallic glass: Heat capacity measurements by fast differential scanning calorimetry, Thermochim Acta 685 (2020) 178518. https://doi.org/10.1016/J.TCA.2020.178518.

[180] M. Gao, J.H. Perepezko, Separating β relaxation from α relaxation in fragile metallic glasses based on ultrafast flash differential scanning calorimetry, Phys Rev Mater 4 (2020) 025602. https://doi.org/10.1103/PHYSREVMATERIALS.4.025602/FIGURES/9/MEDIUM.

[181] E. Zhuravlev, C. Schick, Fast scanning power compensated differential scanning nano-calorimeter: 2. Heat capacity analysis, Thermochim Acta 505 (2010) 14–21. https://doi.org/10.1016/J.TCA.2010.03.020.
[182] Q. Cheng, X. Han, I. Kaban, I. Soldatov, W.H. Wang, Y.H. Sun, J. Orava, Phase transformations in a Cu–Zr–Al metallic glass, Scr Mater 183 (2020) 61–65. https://doi.org/10.1016/J.SCRIPTAMAT.2020.03.028.
[183] J.E.K. Schawe, J.F. Löffler, Kinetics of structure formation in the vicinity of the glass transition, Acta Mater 226 (2022) 117630. https://doi.org/10.1016/J.ACTAMAT.2022.117630.
[184] Y. Geng, Y. Wang, J. Qiang, G. Zhang, C. Dong, P. Häussler, Composition formulas of Fe–B binary amorphous alloys, J Non Cryst Solids 432 (2016) 453–458. https://doi.org/10.1016/J.JNONCRYSOL.2015.11.004.
[185] U. Köster, J. Meinhardt, Crystallization of highly undercooled metallic melts and metallic glasses around the glass transition temperature, Materials Science and Engineering: A 178 (1994) 271–278. https://doi.org/10.1016/0921-5093(94)90553-3.
[186] U. Köster, U. Herold, H.-G. Hillenbrand, J. Denis, Diffusion in some iron-based metallic glasses, J Mater Sci 15 (1980) 2125–2128. https://doi.org/10.1007/BF00550644.
[187] M.-N. Avettand-Fènoël, X. Sauvage, M. Marinova, A. Addad, Multiscale investigation of the crystallization mechanisms and solute redistribution during annealing of a Fe64B24Y4Nb6Al0.4 metallic glass, J Alloys Compd 887 (2021) 161264. https://doi.org/10.1016/j.jallcom.2021.161264.
[188] F. C. Frank, Radially symmetric phase growth controlled by diffusion, Proc R Soc Lond A Math Phys Sci 201 (1950) 586–599. https://doi.org/10.1098/rspa.1950.0080.
[189] M. Palumbo, M. Baricco, Modelling of primary bcc-Fe crystal growth in a Fe85B 15 amorphous alloy, Acta Mater 53 (2005) 2231–2239. https://doi.org/10.1016/j.actamat.2005.01.029.
[190] P.R. Rios, Relationship between non-isothermal transformation curves and isothermal and non-isothermal kinetics, Acta Mater 53 (2005) 4893–4901. https://doi.org/10.1016/j.actamat.2005.07.005.
[191] F. Spaepen, A structural model for the solid-liquid interface in monatomic systems, Acta Metallurgica 23 (1975) 729–743. https://doi.org/10.1016/0001-6160(75)90056-5.
[192] V. Ozoliņš, M. Asta, Large vibrational effects upon calculated phase boundaries in Al-Sc, Phys Rev Lett 86 (2001) 448–451. https://doi.org/10.1103/PHYSREVLETT.86.448.
[193] J.E. Jensen, W.A. Tuttle, R.B. Stewart, H. Brechna, A.G. Prodell, Brookhaven National Laboratory Selected Cryogenic Data Notebook: Sections 1-9, 1980. https://ntrl.ntis.gov/NTRL/dashboard/searchResults/titleDetail/DE87002799.xhtml (accessed November 18, 2022).
[194] V. Sarou-Kanian, F. Millot, J.C. Rifflet, Surface Tension and Density of Oxygen-Free Liquid Aluminum at High Temperature, Int J Thermophys 24 (2003) 277–286. https://doi.org/10.1023/A:1022466319501.

[195] C. Wu, W. Huang, X. Su, H. Peng, J. Wang, Y. Liu, Experimental investigation and thermodynamic calculation of the Al–Fe–P system at low phosphorus contents, Calphad 38 (2012) 1–6. https://doi.org/10.1016/J.CALPHAD.2012.03.005.

[196] S. Kardellass, C. Servant, N. Selhaoui, A. Iddaoudi, M.A. Amar, L. Bouirden, A thermodynamic assessment of the iron-yttrium system, J Alloys Compd 583 (2014) 598–606. https://doi.org/10.1016/J.JALLCOM.2013.07.010.

[197] W.J. Golumbfskie, S.N. Prins, T.J. Eden, Z.K. Liu, Predictions of the Al-rich region of the Al-Co-Ni-Y system based upon first-principles and experimental data, CALPHAD 33 (2009) 124–135. https://doi.org/10.1016/J.CALPHAD.2008.09.001.

[198] A.T. Dinsdale, SGTE data for pure elements, Calphad 15 (1991) 317–425. https://doi.org/10.1016/0364-5916(91)90030-N.